Advanced Limiter-divertor Plasma-facing Systems (ALPS)

August 2001

The Advanced Limiter-Divertor Plasma-facing Systems (ALPS) Program has been addressing issues for advanced systems since 1998. The goals of the program are:

- Establish the scientific and technological base for innovative plasma facing systems that can significantly advance fusion science and improve the vision for fusion as an energy source.
- Provide advanced plasma-facing systems and technology to the plasma physics community to enhance the performance and understanding of plasmas in existing and near term devices.

The program focus thus far has been to determine feasibility of using liquid surfaces for limiters and divertors, determine the operating windows for candidate materials, develop models to understand plasma material interactions, and conduct laboratory and tokamak tests to obtain key materials data and to determine performance. Candidate liquid surface materials include Li, SnLi, Sn, Flibe

The program is divided into four major categories.

- Plasma Edge and PMI Modeling. Modeling investigations are performed to assess the feasibility of using liquid surfaces without adversely affecting plasma performance. State-of-the-art codes are used to model the plasma edge, plasma sheath at the divertor, and particle surface interactions. The results are used to establish the operating windows for candidate liquids.
- Liquid Surface PMI Experiments. Laboratory experiments are performed to determine physical properties e.g., physical sputtering, of candidate liquids and to develop a fundamental understanding of particle interactions with liquid surfaces.
- Tokamak Experiments. Liquid lithium has been tested in CDX-U at PPPL and DIII-D at GA. The experiments have shown that lithium can safely be tested in such devices and plasma performance need not be adversely affected.
- Heat Transfer in Liquid Surfaces. Liquid surfaces potentially offer the capability to remove high heat fluxes. Flowing liquid metals in magnetically confined systems will be influenced by MHD phenomena, and work is underway to examine how MHD forces will affect heat removal capability.

This report summarizes recent results in these areas.

1.0 Plasma Edge and PMI Modeling

ALPS REPORT—Edge/PMI Modeling

PART A

Introduction to ALPS PMI Modeling, J.N. Brooks, ANL

Plasma Material Interaction (PMI) analysis is a key area for the ALPS and APEX projects. We formed a ***Plasma Edge and Plasma/Material Interaction Modeling Group*** at the start of these projects, to work on both ALPS/APEX problems and on general fusion community-wide projects.. The purpose, membership, and current tasks of the group are as follows.

Purpose

Undertake model integration and studies of the plasma edge and plasma/material interactions that lead to:

1) fundamental understanding of the influences of plasma facing surfaces on fusion plasma performance

2) identifying performance limits and optimization strategies for advanced liquid and solid, first wall and PFC concepts.

Near Term Goal

Support the ALPS and APEX programs to help determine the feasibility of and optimization strategies for advanced first wall and PFC concepts.

Group Members

J. Brooks (ANL) – Chairman
T. Evans (GA)
A. Hassanein (ANL)
L. Owen (ORNL)
M. Rensink (LLNL)
T. Rognlien (LLNL)
D. Ruzic (UIUC)
C. Skinner (PPPL)
D. Stotler (PPPL)
R. Maingi (ORNL)
D. Whyte (UCSD)

C. Wong (GA)

· Current Tasks

Task 1. Support NSTX liquid surface module proposal via analysis of scrape off layer (SOL) plasma with hydrogen-absorbing surface, lithium sputtering and transport, hydrogen, helium recycling characteristics, and related issues. (LLNL, ANL, GA, ORNL, UCSD, UIUC)

Task 2: Conduct plasma fluid code analysis (UEDGE code) of tokamak fusion reactor and FRC reactor sol with liquid *wall* (APEX designs). Estimate maximum permissible wall-temperature/wall-impurity-flux based on global plasma core plasma impurity limits and sol radiation limits. For tin, tin-lithium (tokamak), lithium etc. (FRC). (LLNL)

Task 3: Conduct plasma fluid code analysis (UEDGE code) of tokamak fusion reactor scrape off layer with liquid *divertor*. (ALPS-ARIES design). Obtain initial hydrogen edge plasmas and later couple to the divertor impurity source from Task 3. Using combined UEDGE/REDEP analysis estimate sputtered impurity concentration in SOL. For lithium, tin (gallium). (LLNL, ANL)

Task 4: Conduct erosion/redeposition analysis (REDEP code package) of liquid surface fusion reactor divertor (ALPS-ARIES design). Via coordination with Task 2 analysis, estimate maximum allowable near-surface plasma temperature based on self-sputtering limits. Estimate core plasma contamination from sputtering. Use ALPS/APEX developed data and code estimates of sputtering yields. For lithium, tin, gallium. (ANL, LLNL, UIUC, SNL,GA)

Task 5. Support CDX-U (lithium) and DIII-D/DiMES (lithium, tin, etc.) experiments:

a) Conduct b2.5 and/or UEDGE analysis of DiMES background/SOL plasma parameters (ORNL,LLNL, GA).
b) Estimate—to the extent possible from data and parametric modeling—near-surface plasma parameters for CDX-U (PPPL, ORNL, UCSD)

c) Using above plasma parameter estimates (and DIII-D near-surface data) conduct REDEP and related code analysis of impurity sputtering and transport in DIII-D and CDX-U (ANL, UIUC, GA)

d) Compare code predictions to data, and benchmark codes. (all)

Task 6. Model particle fluxes (D-T, He) to and entrainment in liquid surfaces. Compare predictions with available test data. (ANL, LLNL, UCSD, SNL)

Task 7. Model the effects of ELMs on loss of material from liquid surfaces. Compare predictions with available test data. (ANL, GA, UCSD, SNL)

Task 8. Compute evaporation-limited surface temperature. limits for divertor liquid surfaces based on BPHI-3D sheath kinetic code analysis. For lithium, tin, gallium (ANL)

Task 9. Coordinate and provide up-date on atomic physics data/models. (GA)

In the following four parts of this Edge/PMI section we discuss four work areas representing parts of the above goals. These areas are: B) plasma edge modeling, C) liquid surface sputtering data and modeling, D) erosion/redeposition analysis of liquid lithium based divertors and sheath/surface analysis, and E) helium and hydrogen retention/release in liquid lithium,

PART B

Hydrogenic edge-plasma characteristics from transport analysis: T.D. Rognlien and M.E. Rensink, LLNL

B 1

The properties of the plasma adjacent to divertor plates, limiters, and other plasma-facing components play a dominate role in determining the peak particle and heat fluxes incident on these surfaces. The power which drives this edge-region plasma comes from the core plasma energy input (ohmic, auxiliary, and/or alpha-particle heating). The edge-plasma particle source comes from neutrals recycling from surfaces and those intentionally injected through gas puffing. We obtain the two-dimensional (2D) profiles of the edge plasma by solving a set of plasma and neutral fluid transport equations for particle continuity, parallel momentum (along the B-field), and separate ion and electron energy equations; the resulting computer code is called UEDGE [1,2]. The domain modeled includes a region a short distance inside the core boundary (defined by the magnetic separatrix) to the exterior material surfaces, and in this section, we focus on the dominant hydrogenic species in a tokamak configuration.

The output of the transport calculations give the heat load as a function of position on the material surfaces, and they also provide plasma densities and temperatures near the surfaces that are used for more detailed sheath modeling and erosion/redeposition simulations described in Sec. [?]. The hydrogenic plasma properties also serve as the beginning state for analyzing transport of impurity and neutral particles in the edge region as discussed later. The transport models have been benchmarked extensively with present experimental data, especially from the well-diagnosed DIII-D tokamak at General Atomics, *e.g.*, Ref. 3. The primary uncertainty in the modeling is the magnitude of the turbulence-induced transport, but comparison with experiments and turbulence modeling brackets the range of values expected to be in the range of 0.1 - 4 m^2/s.

Two general types of divertor plasmas arise, those with high-recycling divertor plates and those with low -recycling plates, where low recycling usually pertains to particle recycling coefficients of about 1/2 or less. High recycling gives high plasma densities at the plates and low temperatures of tens of eV or less; the detached plasma is the low-temperature, recombining-plasma extreme of this regime (sometimes called a third type of divertor plasma) [4]. The low-recycling regime has low density and high temperature; this regime is less common experimentally, but if it can be produced in a reactor, may

lead improved core micro-stability. However, for low recycling, a large particle flux out of the core may need to be maintained by an edge particle-fueling source such as pellets. Parameters of the regimes are illustrated in Table 1.

Table 1 Hydrogenic edge-plasma density and electron temperature at two locations for a large tokamak with low and high plate recycling coefficients.

Hydrogen plate recycling coefficient	Midplane n_e (10^{19} m^{-3})	Midplane T_e (eV)	Plate n_e (10^{19} m^{-3})	Plate T_e (eV)
$R_h = 0.25$	0.95	1090	0.26	960
$R_h = 0.99$	3.50	225	50.9	76

A device study that we have recently analyzed is the ARIES-AT tokamak [5], with the edge-plasma domain shown in Fig. 1. In the figure, the divertor plates are shown orthogonal to the magnetic flux surfaces, but we have surveyed the effect of tilting the plates and allowing a portion of the core power to be radiated by edge impurities to reduce the heat load [4]. The plate heat flux is shown in Fig. 2 for 77% of the core power radiated and a 30° angle between the flux surface and the plate. For this case, the plate recycling coefficient is unity.

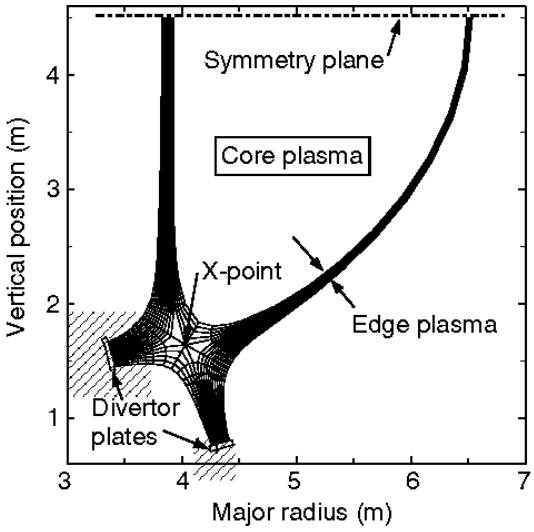

Fig. 1. Modeling domain for UEDGE simulation for lower half of the symmetric double-null tokamak ARIES-AT with orthogonal plates.

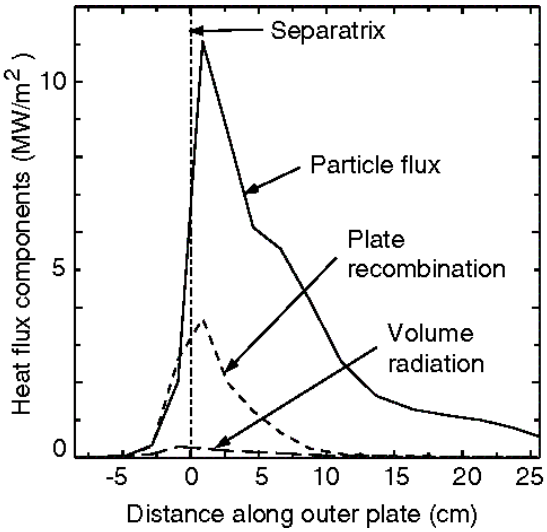

Fig. 2. Components of plasma heat flux on outer divertor plate for 30° between plate and flux surfaces and 77% of the core power radiated.

Simulations of the hydrogenic edge plasma have also been performed for other devices of interest to ALPS, namely, the ITER and FIRE tokamaks, and two spherical tori, NSTX and CDX-U. For NSTX, we have modeled the effect of a hydrogen-pumping liquid module place either at the midplane (limiter) or in the divertor region. Both show that substantially pumping of hydrogen may be possible (assuming the hydrogen retention properties of Li) without excessive heat load on the module, and that the pumping increases the separatrix plasma temperature for better micro-stability properties; these results are presented in the ALIST proposal for a lithium module in NSTX.

B 2. Temperature limits of liquid first-walls for tokamaks based on impurity contamination

The UEDGE calculations of the hydrogen edge-plasma is augmented by including a source of impurities from the first wall to model the evaporation and subsequent ionization of impurity gas. There are a number of processes included in the modeling. The impurity gas is emitted from the wall in the form of atoms at typically ~1 eV if they arise from dissociation of molecules (*i.e.,* Frank-Condon-like neutrals), although a range of energies have been considered since molecular dissociation is not yet modeled in any detail, and for lithium walls, the vapor likely comes off the wall in the form of atoms. These neutrals diffuse by elastic collisions with ions until they are ionized by the electrons of the edge plasma. Once an ion, the impurity diffuses across the magnetic field with anomalous diffusion coefficients estimated from present experimental devices. Thus, the ions can diffuse radially into the core or back to the liquid wall where they are assumed to be absorbed. In addition, the ions can flow along the magnetic field and out of the system. The electron energy lost by ionizing the impurities through all of their charge states is included, so that the impinging impurities depress the electron temperature, especially near the liquid surface. See Refs. [1,2] for more details on the basic models.

A number of calculations have been made for a tokamak configuration of the ARIES-AT size assuming different liquid-wall materials with evaporation rates that depend on

temperature. The density of the impurity species at the core must be kept below a critical value to avoid fuel dilution or excessive impurity core radiation. The core fusion power is reduced by a factor of $(1 - 2Zn_z/n_h)$ for small impurity density n_z compared to the hydrogen density n_h. Here Z is the charge of the impurity. If the dilution limit is legislated to be a 20% power reduction, impurity radiation takes over to set the impurity limit for Z > 10. A summary of these results for low- and high-recycling divertor plates is shown in Table 2. From considerations of the radiative heating and thermal-cycle requirements for the first wall, the limits for Sn are clearly the best for tokamaks. All but the Sn case are detailed in the literature [6,7]. Lithium and SnLi give about 10 times too much impurity flux, and for Flibe even more reduction is needed. Near the critical impurity level, the edge-plasma is substantially modified by the presence of the impurities, so it is important to perform self-consistent, coupled hydrogen/impurity transport simulations as has been done here. Intervention schemes like auxiliary edge-plasma heating for increasing the impurity removal may lead to higher temperature limits.

Table 2 Effective temperature limits for different liquid first-wall materials in a large tokamak based on core impurity dilution and radiation loss for two divertor plate recycling coefficients.

Hydrogen recycling coeff.	Lithium (^oC)	Flibe (F) (^oC)	$Sn_{80}Li_{20}$ (Li) (^oC)	Sn (^oC)
$R_h = 0.25$	380	480	590	>850
$R_h = 0.99$	>300	400	>500	830

B 3. Divertor/SOL coupling, DIII-D DiMES edge-plasma, and alternate devices

Transport of impurities originating from the divertor plate is strongly affected by the sheath and near-surface plasma conditions owing to the substantial electron temperature and density that can exist there (compared to the typically low T_e and n_e near the first wall); substantial ionization of impurities can occur within the sheath region. Consequently, detailed modeling of the near-plate region is required with the particle code WBC by Brooks [8]. In order to trace the impurities leaving this near-plate region in the full scrape-off layer to the core, we have taken the impurity flux output at the end

of the WBC domain as input to the UEDGE code. An example of this coupling is reported in Ref. 8 for sputtering of a lithium divertor plate in the low-recycling regime. The substantial attenuation of the lithium from the near-plate region shown by WBC is further augmented as the lithium escaping the plate region tries to move upstream in the face of the collisional drag from the hydrogen flowing toward the plate. The resulting lithium density at the core boundary originating from the plate is thus found to be at least two orders of magnitude below the critical value for core dilution.

Calculations have also been performed to better understand the behavior of the DIII-D DiMES lithium probe, especially during its large impurity-release phase. Since the evolution of the plasma through its thermal collapse phase takes 10's of ms, much longer than the toroidal flow time needed to smooth out the initial toroidally localized DiMES source, we have used the 2D UEDGE transport model in a time-dependent mode to help understand how the lithium may migrate into the core region. These calculations also help us benchmark of impurity transport models. If a large lithium gas influx consistent with the later-observed lithium core density is taken at the divertor floor, the lithium causes a thermal collapse of the divertor plasma, thereby allowing the lithium gas to approach the X-point were it can enter the core region. Alternately, if the lithium reaches the core as a liquid and is then vaporized, we also show that thermal collapse begins in the edge region where the electron temperature is in the range of effective radiation by lithium. The possible ejection of the liquid lithium from the DiMES probe may depend on the thermoelectric currents in the plasma, so we include these for the hydrogenic base-case.

The previous modeling of impurity intrusion to the core plasma of tokamaks from liquid walls has been extended to the compact, high power-density Field-Reversed Configuration (FRC) [9]. It is found that the wall temperature limits are substantially higher for the FRC compared to the tokamak, both because of the higher power density which sustains the edge plasma at a higher temperature and the shorter distance along the B-field that impurity ions need to travel to escape out the end of the device. For Flibe, we now find an effective wall temperature limit of 630 ^{o}C, while for SnLi we obtain 720 ^{o}C for the same assumption of flat impurity profiles in the core as used in Table 2 for tokamaks. For the FRC, this means that SnLi would not quite reach the critical temperature, whereas Flibe would exceed it by only 30 ^{o}C [9]. If the impurity profile follows that of the hydrogenic species, the allowable temperatures decrease by about 60 ^{o}C.

REFERENCES for Part B

[1] T.D. Rognlien, P.N. Brown, R.B. Campbell, *et al.,* Contr. Plasma Phys. **34**, (1994) 362.

[2] T.D. Rognlien, M.E. Rensink, and G.R. Smith, "Users manual for UEDGE edge-plasma transport code," Lawrence Livermore Nat. Lab. Report UCRL-ID-127121, Jan. 21, 2000.

[3] G.D. Porter, R. Isler, J. Boedo, *et al.,* Phys. Plasmas **7** (2000) 3663.

[4] T.D. Rognlien and M.E. Rensink, "Edge-plasmas models and characteristics for magnetic fusion energy devices," submitted to Fusion Eng. Design, 2001.

[5] A.R. Raffray, M.S. Tillack, X. Wang, *et al.,* Fusion Tech. **39** (2001) 429.

[6] T.D. Rognlien and M.E. Rensink, J. Nucl. Mater. **290-293** (2001) 312.

[7] R.W. Moir, M.E. Rensink, and T.D. Rognlien, 18th IAEA Fusion Energy Conf., Sorrento, paper IAEA-CN-77FTP2/07 (IAEA, Vienna, 2001).

[8] J.N. Brooks, T.D. Rognlien, D.N. Ruzic, and J.P. Allain, J. Nucl. Mater. **290-293** (2001) 185.

[9] R.W. Moir, R.H. Bulmer, K. Gulec, *et al.,* Fusion Tech. **39** (2001) 758.

PART C

Sputtering erosion/redeposition and sheath studies, J.N. Brooks, ANL, T.D. Ronglien, LLNL, D.N. Ruzic, UIUC, J.P. Allain, UIUC, D. Naujoks, ANL/IPP-Berlin

The purpose of sputtering erosion/redeposition and sheath studies is to determine (1) surface temperature, plasma edge temperature, and heat flux limits on flowing liquid surface divertors, (2) impurity content in and effects on scrapeoff layer and edge plasma, (3) tritium codeposition in sputtered, transported, and possibly solidifying materials, (4) effects on core plasma and reactor performance, (5) compatibility between wall and divertor materials, and (6) critical data needs (e.g. self-sputtering yields). This part summarizes results described in three recent journal papers [1-3]

D 1 Erosion/redeposition

In study [1] a sputtering erosion/redeposition analysis was performed for three candidate tokamak fusion reactor liquid divertor surfaces—lithium, tin-lithium ($Sn_{80}Li_{20}$), and flibe ($LiF+BeF_2$ salt). The analysis uses coupled edge-plasma, impurity-transport, and sputtering codes (UEDGE/WBC/VFTRIM), and available sputtering data. A pure-lithium surface strongly absorbs impinging D-T ions—this results in a high temperature, low density, (~200 eV, ~$1x10^{19}$ m^{-3}) *low-recycle* plasma edge regime. Lithium appears to perform well in this regime. Although overall sputtering is high, self-sputtering is finite. Most (~95%) of the sputtered lithium is confined to the near-surface region and redeposited on the divertor with the remainder (~5%) also being redeposited after transport in the scrape-off layer. Lithium core plasma contamination is low (~10^{-4} Li/D-T). Tin-lithium and flibe would likely operate in a high-recycle regime (e.g., 30 eV, $3x10^{20}$ m^{-3}). Erosion/redeposition performance of these materials is also good, with finite self-sputtering and negligible core plasma contamination predicted, but with some concern about changing surface composition due to different constituent element redeposition distances.

Some of the WBC/UEDGE lithium erosion/redeposition results are summarized in Figures 1-2 and Table 1. In spite of high redeposited Li^+ energies and generally oblique

incidence, self-sputtering is limited, comprising some 25% of the total. Of the total sputtered lithium current, ~95% is locally redeposited via near-surface impurity/plasma transport processes, ~5% leaves the near-surface region but returns to be redeposited after SOL transport, and ~0.2% enters the private flux region or hits the first wall. Lithium is thus mostly confined to the near surface region. A liquid surface has, of course, zero net erosion on the time scale of the liquid flow, however, gross and instantaneous (i.e., before liquid flow) net erosion rates are shown (Fig. 1) for comparison to previous solid-material studies. These rates are high, but due to the continuous replenishment, of apparently limited significance.

In summary, lithium sputtering rates are high, but the sputtered lithium is well confined close to the divertor surface with resulting low core plasma contamination. The high confinement is due to high electron-impact ionization rate coefficients, low binding energy/sputtered-velocities, and reasonably high impurity/plasma collision frequencies. Based on WBC code results for redeposited lithium ion energies and impingement angles, and on available data, we predict that lithium self-sputtering is well short of runaway. Further evaluation is needed for lower density/higher temperature plasma regimes. Other critical psi issues needing analysis for pure lithium are: effect of high tritium removal rates on plasma refueling requirements and helium removal by trapping in the lithium.

An important related psi/engineering issue is the maximum allowable surface temperature. The present lithium calculations are based on code/data results for 200 °C. Evaporation/sheath analysis sets an upper limit for lithium of order 500 °C [2,3]. A lower limit, however, could be set by thermally-enhanced sputtering rates as possibly seen in PISCES [4] and preliminarily in IIAX, and depending also on the spectrum (e.g. thermal) and form (atom, ion, macroscopic) of the emitted material.

Figure 2 shows sputtered ion densities near the divertor surface for a tin-lithium surface. These densities are all low compared to the D-T density and fall off rapidly away from the surface. Essentially zero core plasma contamination by sputtering is predicted. For

both flibe and tin-lithium the analysis shows high confinement of impurities in the near-surface region with low potential for core plasma contamination, and no runaway self-sputtering. These results are encouraging but more work is needed on, for instance, full plasma profile effects, performance for different plasma edge temperatures/densities, surface temperature effects, surface segregation properties and properties of redeposited material. Sputtering data is also needed.

Table 1 summarizes various redeposition parameters for the flibe and tin-lithium components, and also as mentioned previously, for pure lithium. The sputtered tin-lithium atoms have short mean free paths for ionization, due to a combination of low binding energy (lower sputtered energies), high electron density, and high ionization cross sections. Much ionization occurs in the magnetic sheath, for these high-recycling plasma conditions. Lithium from flibe behaves similarly. The beryllium and fluorine components travel longer but still fairly short distances. After ionization, subsequent strong collisional friction with the incoming plasma—and particularly for Sn and Li, sheath field acceleration—gives rise to the high local redeposition. The redeposited ion angle and energy parameters suggest data needed from sputtering experiments. For tin-lithium it is significant that redeposited Sn impacts at near-normal incidence, in contrast to the F and Be components of flibe which redeposit at more oblique incidence.

D 2 Sheath Studies

In-sheath ionization of surface-emitted material can affect the tokamak type (strong B field at highly oblique angle) sheath. This is particularly true for a low vapor pressure material like lithium. Reference [2] describes the newly developed BPHI-3D code and initial studies for plasma sheath interactions with lithium and also for carbon. This is a self-consistent 3-D numerical analysis performed for the Debye/magnetic tokamak-type oblique incidence magnetic field sheath, with near-surface ionization and transport of thermally emitted surface material. The analysis uses Monte Carlo, kinetic treatment for deuterium-tritium (D-T) and impurity ions/neutrals, Boltzmann/guiding-center electrons, and particle-in-cell time-independent Poisson solver. For typical predicted fusion edge

plasma conditions for a liquid lithium divertor most evaporated lithium atoms—from a ~1 cm^2 overheated spot—are ionized in the ~ 1 mm wide magnetic sheath. These ions are strongly redeposited due to the sheath electric field. While this redeposition minimizes core plasma contamination it increases the peak heat flux to the surface. A runaway situation is then possible due to superheating/evaporation positive feedback. Carbon may behave likewise as seen in code results obtained for a TORE SUPRA carbon limiter. A semi-analytic formula for sheath parameters as a function of emitted surface material flux was developed and verified with the code.

In study [2] the semi-analytic model is extended and the BPHI-3D code is coupled with the THERM code which solves the non-stationary heat conduction equation also in 3D geometry. Runaway heating due to initial overheating and subsequent sheath breakdown and superheat was analyzed for lithium and carbon. For typical liquid lithium divertor conditions the critical exposure time for thermal runaway is of order 10 ms – generally greater than transient periods (e.g. ELMS) or flowing liquid exposure times. This is encouraging. Critical exposure times for carbon are much longer (~1-2s), as expected due to thermal property differences, and this may explain various "hot spot" formations in carbon systems. It is also shown that, especially for carbon materials, effects such as flake formation and deterioration of heat conductivity can play a critical role.

REFERENCES for Part D

[1] J.N. Brooks, T.D. Rognlien, D.N. Ruzic, J.P. Allain, J. Nuc. Mat. 290-293(2001)185..

[2] J.N. Brooks, D. Naujoks, Physics of Plasmas, 7(2000)2565.

[3] D. Naujoks, J.N. Brooks, J. Nuc. Mat. 290-293(2001)1123.

[4] R.P. Doerner et al. ibid p166.

[5] J.P. Allain, D.N. Ruzic, ibid p180; also see this report Part C

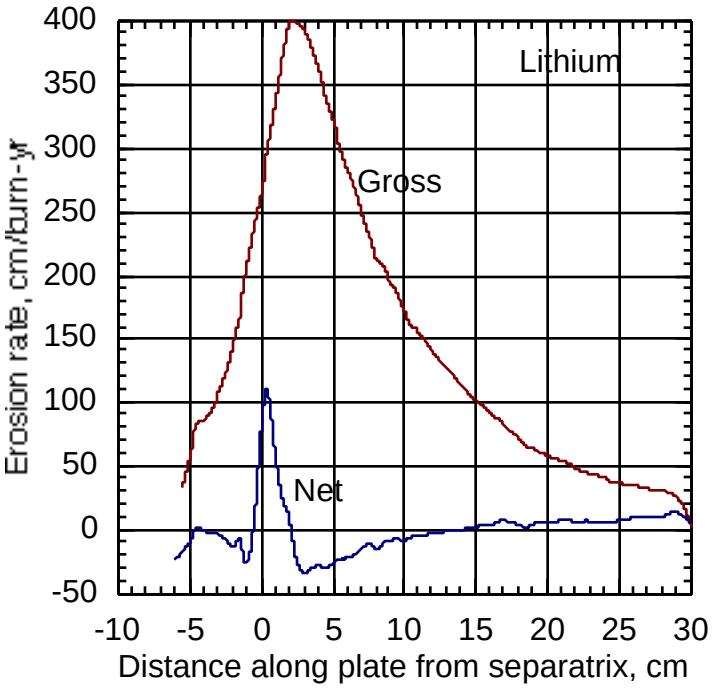

Figure 1. Gross and instantaneous (before liquid flow) net erosion rates from the WBC analysis of the lithium divertor. (Net erosion rate with flow is zero).

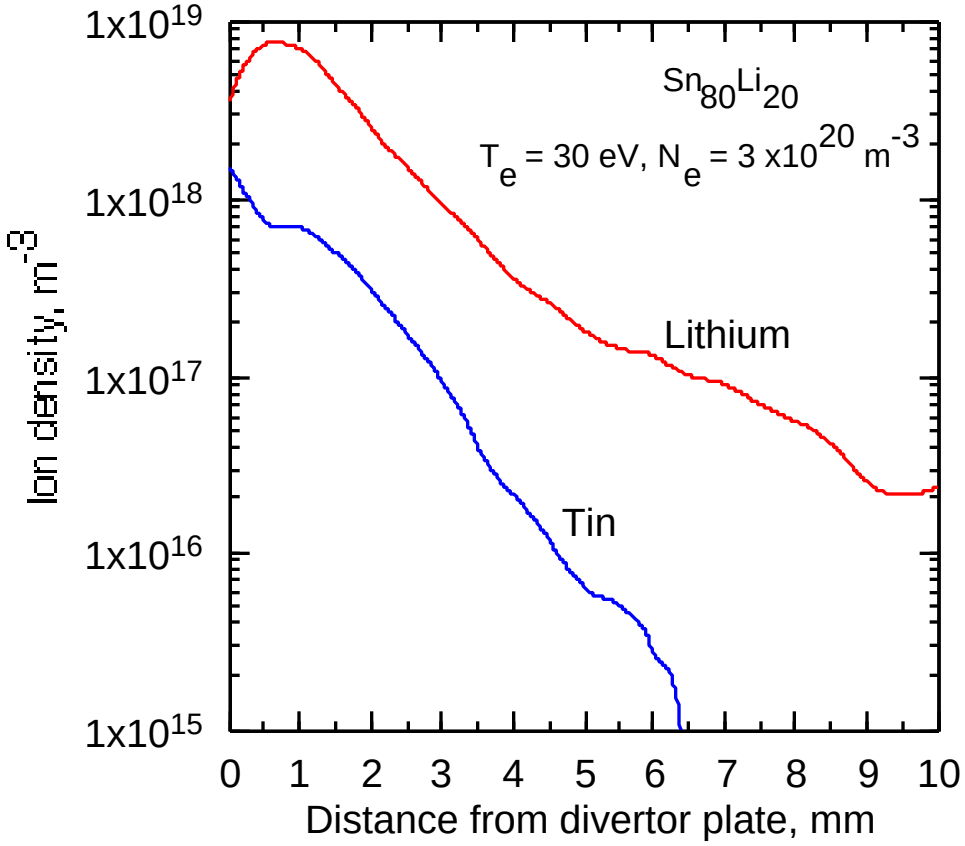

Figure 2. Sputtered ion densities near the divertor plate for a tin-lithium divertor.

Table 1 Selected erosion/redeposition parameters from WBC analysis of three liquid divertor surfaces.

Parameter[a]	LITHIUM	TIN-LITHIUM		FLIBE		
	(pure)	Li	Sn	Li	Be	F
Plasma conditions at divertor; Te(eV)/Ne(10^{20} m^{-3})	variable; 185/0.1 at separatrix	30/3		30/3		
Binding energy, eV	1.12	2.40	2.40	7.49	7.49	7.49
Neutral ionization distance[b], mm	4.6	0.29[c]	0.15	0.30	0.86	1.4
Charge state	1.1	1.0	1.5	1.0	1.5	2.0
Transit time, μs	15	0.33	0.17	0.24	0.85	1.6
Elevation angle, °	53	32	15	30	42	42
Energy, eV	238	96	110	95	171	268
Poloidal distance from launch point (standard deviation), mm	70	2.0	1.1	1.7	4.7	7.9
Redeposition fraction (for 5 cm near-surface-cutoff)	0.950[d]	1.000	1.000	1.000	1.000	1.000

a Except where noted denotes average value for redeposited ions

b Normal to surface

c Includes effect of high reflected Li component

d Total redeposition (with SOL transport) = 0.998

PART D

Hydrogen Isotope and Helium Particles Entrapment in Flowing Liquid Metals as Divertor Surfaces

Ahmed Hassanein
Argonne National Laboratory

I. Introduction

The ability to use liquids as divertor surfaces depends on their interaction with the plasma. One important area that will influence the selection of liquid surfaces is the ability of the moving liquid to entrain particles that strike the surface. Particle entrapment could determine the viability of specific liquid candidates as successful renewable divertor surfaces. DT particles striking the surface will most likely be trapped in a lithium surface due to the high chemical solubility of hydrogen in liquid lithium. This will result in a low recycling divertor and a high edge temperature (several hundred eV). There are several implications of low recycling divertor on plasma performance. An important question is whether He can be pumped at low density using a standard vacuum system approach. If helium particles are not entrained in the surface and pumped out of the divertor, then standard vacuum pumping techniques must be used. However, the low recycling regime also results in a low density/pressure at the pump ducts. Helium is a difficult species to vacuum pump, and it may be more difficult or impossible to get adequate pumping in this situation.

Therefore, the understanding of particle entrapment in liquid surfaces is crucial to assessing their viability for divertor operation. Modeling of the kinetics of particle injection, motion and interactions with the liquid lattice, and ultimate release from the surface is presented in this analysis.

The purpose of this study is to investigate ability of liquid lithium layer to absorb incoming flux of helium, deuterium and lithium. There are several implications of low recycling divertor on plasma performance. If helium particles are not entrained in the surface and pumped out of the divertor, then standard vacuum pumping techniques must be used. However, the low recycling regime also results in a low density/pressure at the pump ducts. Helium is a difficult species to vacuum pump, and it may be more difficult or impossible to get adequate pumping in this situation.

The potential for any of the liquid candidates (Li, Tin, Flibe, etc) to work satisfactorily depends on whether particles with negligible chemical solubility (for example, He in Li and DT in Flibe) become entrained in the surface for a long enough time to be removed from the divertor chamber. If He is entrained in lithium, DT particles will more likely be entrained in Flibe. In this case, the lithium system seems more attractive, and the Flibe system appears undesirable since entrapment would result in an unacceptably high edge.

On the other hand, complete recycling (little or no entrapment) would be favorable for Flibe but would make He removal from the lithium system difficult or impossible.

Therefore, the understanding of particle entrapment in liquid surfaces is crucial to assessing their viability for divertor operation. Modeling of the kinetics of particle penetration, motion, and interactions with the liquid lattice, and ultimate release from the surface is presented in this analysis.

II. Pumping Requirements

Helium ash produced from as a result of the thermonuclear reaction need to be removed at its production rate. For example, in a 2000 MW fusion power reactor with major radius = 6 m operating in the low-recycle regime, the alpha-production rate, I_{fus} = 2000 MW/ (17.6MeV/fusion) = 7.1 x 10^{20} He/s. The DT current, I_{dt} = 1.6 x 10^{23} s^{-1} and for 10 % He/(D+T) fraction in core plasma, the helium current to divertor is roughly: I_{he} = 1.6 x 10^{22} $s^{-1.}$ Helium must be removed at the production rate. Therefore, the required removal efficiency $\varepsilon = I_{fus//} / I_{he} \approx 0.04$. Thus, we need approximately 5 % removal efficiency.

III. Computational Model

Model describing absorption of helium and DT particles by a layer of liquid metal consists of solving the diffusion equation in x-y direction as shown below in Fig. 1 with various boundary conditions. Modeling of the kinetics of particle injection, motion and interactions with the liquid lattice, and ultimate release from the surface is modeled in details using the HEIGHTS package [1]. The detail implantation of the incident Helium and Hydrogen Isotopes in liquid Li is calculated using the 3-D ITMC Monte Carlo code, part of the HEIGHTS Package [2]. The mesh size of the implantation zone can be as small as one monolayer thick to accurately predict the effect of near surface area. The particle incident energies are governed by the temperature in the SOL as well as by the sheath potential at the wall surface. The TRICS code (part of HEIGHTS) then calculate the details of Helium and Hydrogen Isotope diffusion motion, trapping (if any), and surface release in the form of molecules (D-T particles) due to the recombination mechanism [3].

Figure 2 shows He pumping coefficient as a function of Li flow velocity and He diffusion coefficient for He particles incident energy of 1.0 keV. To achieve adequate He removal rate by the Li at diffusion coefficient $D_o = 10^{-6}$ cm^2/s, Li velocity should be > 20-30 m/s. At higher diffusion coefficients the required Li velocity is very high and can exceed 100 m/s. To achieve adequate He pumping at higher implantation energies (that can result from the low-recycle regime), reasonable Li velocities of ≈ 10 m/s could be sufficient as shown in Fig. 3. However, if He bubbles are formed in the following Li near surface layer, significant He trapping can occur. This needs more detailed investigations.

Although the range of the implanted Hydrogen Isotope in Li is less than 0.1 μm for incident particle kinetic energy as high as 1 keV, the calculated rate of surface recombination into Hydrogen Isotope molecules, and therefore the release rate is very small. The recombination rate is small mainly because of lower recombination coefficient and lower surface concentration due to the short residence time exposure of the moving liquid Li (about 10 ms for an effective 10-cm particle interaction zone moving with velocity of 10 m/s) [4]. It takes a couple of minutes of a stagnant surface to build up enough surface concentration to start having significant recombination and release rate. Therefore, in our case of a moving liquid surface almost all the incident Hydrogen Isotope is retained in the flowing Li. In addition, Hydrogen Isotope concentration near the end-of-range of the implantation zone, coupled with synergistic effects of simultaneous He implantation, could promote bubble formation. This will have the effect of further increasing hydrogen retention due to the slow diffusion of bubbles to the surface. Therefore, in a moving liquid Li as plasma-facing components under these conditions, the Li will pump most of the incident particle flux of the Hydrogen Isotope and should have notable effects on the physics of the boundary layer in future machines using free surface flow of liquid metals.

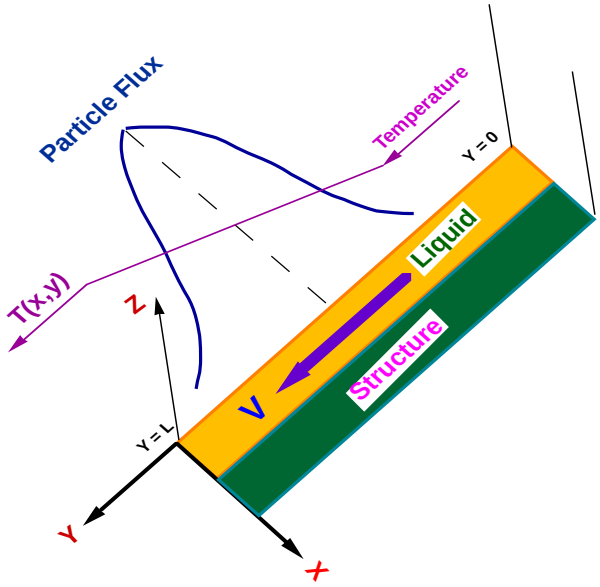

Fig. 1 Schematic illustration of D/T/He interaction with free liquid surface

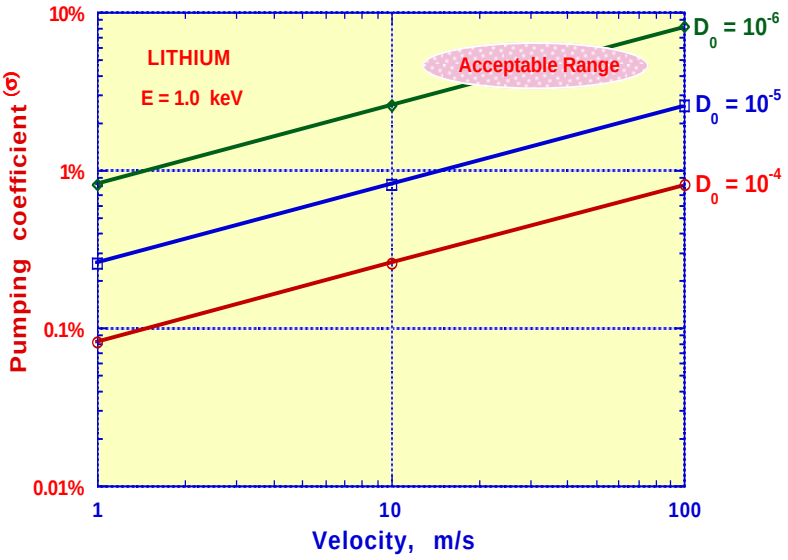

Fig. 2 HEIGHTS calculations of He pumping coefficient as a function of lithium velocity

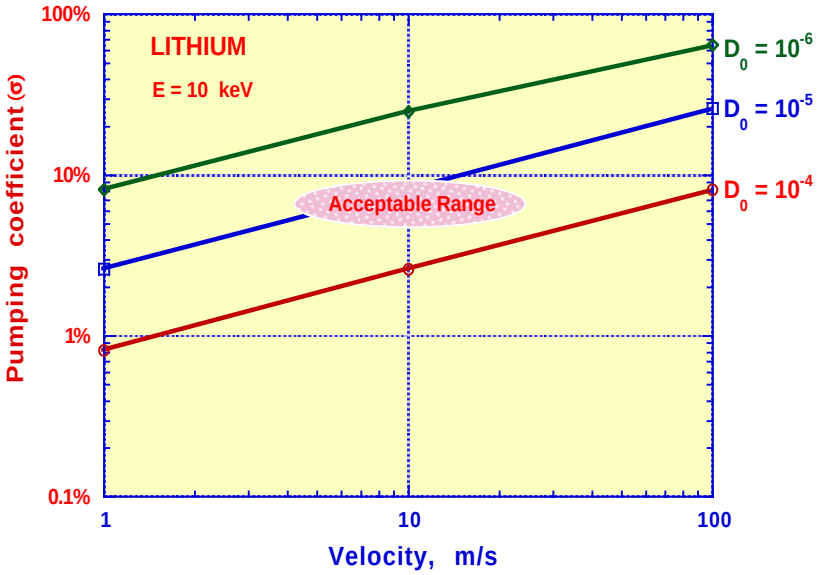

Fig. 3 HEIGHTS calculations of He pumping coefficient as a function of lithium velocity

IV. Summary of particle pumping

(1) To pump He at the minimum required rate of about 4-5%, one need a He diffusion coefficient < 10^{-4} cm^2/s for reasonable liquid velocities. Recent studies indicate this may be feasible.

(2) Helium penetration depth is only several monolayers. Therefore, enhancement due to internal flows is not achieved for several reasons:

(a) Internal flow is not inward but circular, thus; more time is spent near surface; which can enhance the release rate.

(b) More importantly even if one assume inward velocity of 1 m/s as suggested by some authors, one should realize that the liquid is moving with velocities of 10-20 m/s, so the resultant velocity is still mainly in flow direction.

(3) The numerical calculations of HEIGHTS indicate that D and T particles are completely pumped by the flowing Li.

(4) There are, however several uncertainties that in order to resolve require more data on He diffusion and trapping such as bubble formation and growth in liquids that could significantly enhance He pumping. On the other hand, bubbles bursting and splashing will detrap He and DT particles. In addition, one need to synergistic effects of He/D/T interactions with moving liquids.

References for PART E

1. A. Hassanein and I. Konkashbaev, "Comprehensive Physical Models and Simulation Package for Plasma/Material Interaction during Plasma Instabilities," **J. Nucl. Mater. 273** (1999) 326**.**
2. A. Hassanein, " Elastic and Inelastic Surface Effects on Ion Penetration in Solids and Resulting Sputtering and Backscattering," J. **Nucl. Inst. & Method. Phys Res. B13 (1985) 225**.
3. A. Hassanein, et al, " Tritium Behavior in Eroded Dust and Debris of Plasma Facing Materials," **J. Nucl. Mater. 258-263 (1998) 295.**
4. A. Hassanein, "Deuteron Beam Interaction with Li Jet in a Neutron Source Test Facility," **J. Nucl. Mater. 233-237 (1996) 1547**.

2.0 Liquid Surface PMI Experiments

ALPS Report - PMI Experiments

Overview

Plasma-materials interactions (PMI) involving liquids can be significantly different than PMI on solids [1]. Consequently, experimental PMI data on liquid surfaces are needed to understand their behavior when exposed to the energetic particle flux emanating from a fusion plasma. The ALPS PMI experiments group is providing these data using a combination of ion beam and plasma simulator experiments. The intent is twofold: (1) provide experimental measurements of the material parameters needed for realistic PMI modeling of ALPS concepts and (2) to examine under controlled laboratory conditions critical PMI effects to validate or disprove the physical basis of ALPS concepts.

This section contains summary reports from the three laboratories that comprise the ALPS PMI experiments group. The participating organizations are (1) Sandia National Laboratories, (2) the University of California , San Diego, and (3) the University of Illinois, Urbana-Champaign.

Reference:

[1] R. Bastasz and W. Eckstein, J. Nucl. Mater. 290-293 (2001) 19.

Surface Measurements of Liquid Li and Sn-Li (SNL)

Contributed by R. Bastasz
Sandia National Laboratories, Livermore

Surface Analysis of Liquid Lithium and Liquid Tin-Lithium

The composition and charge state distribution of the sputter flux originating from the divertor are important parameters for modeling erosion/deposition effects. The charged fraction of sputtered particles is immediately affected by local fields, while the neutral fraction escapes in straight-line trajectories from the surface until collisions or ionization processes occur. Furthermore, the initial velocity distribution of the sputtered particles is a function of mass. Consequently, it is necessary to obtain information about the various species sputtered from plasma-facing materials. To collect such data, a series of secondary-ion mass spectrometry (SIMS) measurements have been made of liquid Li surfaces during bombardment by hydrogen and helium ion beams. As expected, the predominant sputtered species is Li^+. In addition, an appreciable fraction of the ionized sputter flux is comprised of Li_2^+ dimers , and the oxygen-containing species Li_2O^+, and Li_3O^+. In addition, we measured small amounts of Li_2H^+, but little LiH^+. We found the emission intensity of molecular Li secondary ions containing hydrogen and oxygen to be higher on the liquid surface (at 250 °C) than on the corresponding solid surface (at 25 °C). Evidently the increased diffusivity of impurity species in the Li liquid helps to segregate hydrogen and oxygen to the liquid surface, from which they are eventually

sputtered. These data provide PMI models with information about the sputter flux composition needed to better forecast erosion/deposition rates and plasma contamination levels.

The surface composition of liquid Sn-Li was measured using low energy ion scattering (LEIS), a extremely surface-specific analysis method, as a function of temperature from below the melting point to 450 C. Upon melting, Li and O was observed to segregate to the surface, replacing Sn at the outermost atomic layer. This behavior is shown in Fig. 1. The source of the O atoms are impurities in the starting material. As the liquid temperature is raised, the O coverage begins to decrease. At operating temperatures above 410 °C, the liquid surface is predominantly Li. This observation indicates that initial surface presented to the plasma in a flowing Sn-Li alloy system will be significantly different than the bulk alloy composition. Consequently, using a Sn-Li alloy or adding Li to Sn may be beneficial by making the plasma-facing surface enriched in Li, thereby reducing the Sn sputter flux.

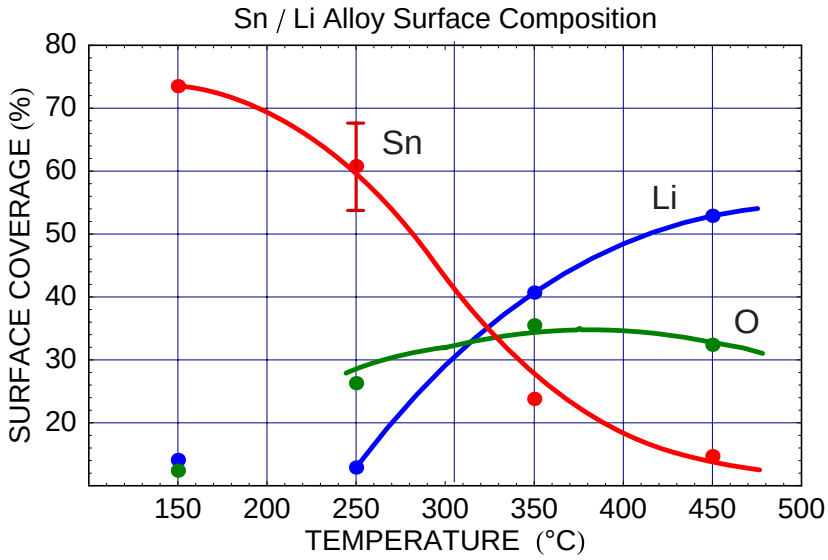

Figure 1. Surface composition of Sn(0.8)-Li(0.2) alloy as a function of temperature as determined by LEIS measurements. Above the melting temperature (222 •C), oxygen and lithium segregate to the surface. At temperatures above 330 °C, Li is the most prevalent atom at the surface of the liquid and the majority of surface atoms above approximately 410 °C are Li. The curves are guidelines only.

Segregation of Lithium to Liquid Tin Surfaces

The above measurements show a strong segregation effect of Li to the surface of liquid Sn-Li alloys. This is a desirable effect for the use of liquid Sn-Li alloys as plasma facing materials, as the surface atoms, which contribute to the majority of sputtered particles, are Li, a plasma-compatible low-Z element. Whether or not this effect can be practically utilized in flowing liquid free-surface in-vessel components, such as divertor and first-wall systems, depends upon maintaining the Li enrichment of the surface layer. This is determined by the liquid surface temperature, the velocity of the flowing surface, the incident particle flux and energy, and the rate of diffusion of Li from the bulk to the liquid surface. We developed a model to take into account these effects, based on simple expressions for the evaporation of Li from the surface, the Li sputtering rate, and the segregation rate of Li to the liquid surface. We calculated, for a flowing liquid divertor with a fresh surface moving across the plasma region, the maximum allowable residence time for a given set of criteria. These calculations assumed a diffusivity of Li in liquid Sn-Li to be on the order of the Li self-diffusion rate in liquid Li. For example, if at least 50% of the surface must remain Li, the maximum residence time is about 25 ms for a 500 eV normal incidence D flux of 10^18 /cm^2-s at an operating temperature of 500 °C. The surface coverage of Li is also dependent on the incident particle energy and a segregated Li surface may persist in certain circumstances. At 10 eV, for an incident flux of 10^17/cm2-s and a surface temperature of 500 °C, the coverage remains high (>50%) for times greater than 1 s. We found that at very high temperatures evaporation is always the main Li loss mechanism. For example, at 700 °C, the time dependence of the Li surface coverage is dominated by evaporation and rather insensitive to the incident particle flux and energy. These calculations help to determine the operating window for flowing liquid Sn-Li alloy divertors.

We also conducted a series of measurements to measure the segregation rate of Li to the surface of a liquid Sn-Li alloy (bulk composition Sn0.8Li0.2) using LEIS. These measurements build upon the techniques we developed for utilizing LEIS to examine the composition of liquid metal surfaces. The particular issue we addressed was to access how fast Li diffuses to the surface of the liquid alloy, since this rate is a major factor in determining how long a flowing liquid divertor surface can be exposed to the divertor plasma in a fusion reactor. The measurements consisted of allowing a liquid Sn-Li surface to reach an equilibrium surface composition (i.e., enriched in Li) and then monitoring the composition as the surface was bombarded with ions of known energy and flux. The measurement was repeated at various liquid alloy temperatures. At lower temperatures, the surface becomes depleted in Li. At higher temperatures and Li diffusivities, the surface remains enriched in Li. This behavior is illustrated in Fig. 2, which shows the abundance of Li at the liquid surface as a function of ion dose for 1 keV He+ bombardment at 68 degrees incidence from the normal.

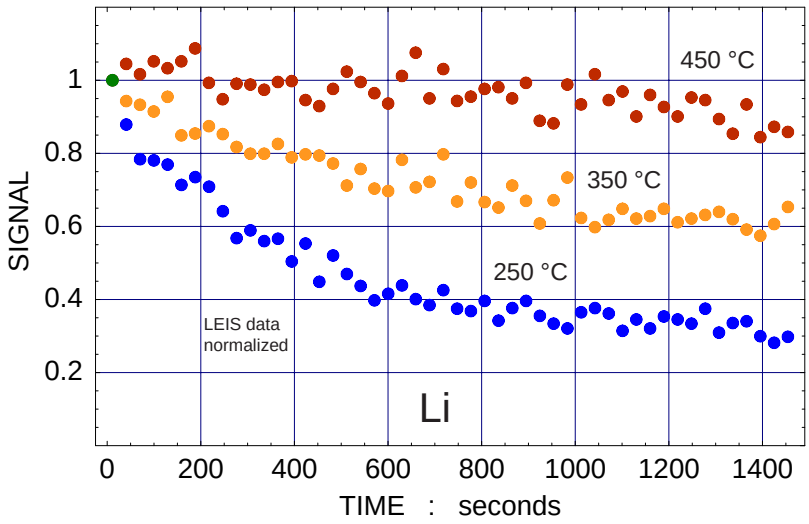

Figure 2. Time evolution of a Sn-Li liquid surface during bombardment by 1 keV He+ at 68° incidence from normal at a flux of about 2 10^13 /cm^2-s. Data are shown for three temperatures. Before beginning each measurement, the surface was allowed to equilibrate, which enriched it in Li. At 450 °C, the segregation rate of Li nearly balances its erosion rate at the surface, resulting in a nearly constant concentration of Li at the surface.

We will obtain additional data of this type during the coming year to complete a quantitative determination of Li diffusivity in liquid Sn-Li at the operating temperatures envisioned for a flowing Sn-Li plasma-facing system. In addition, Ahrennius plots derived from the such data yield the thermodynamic characteristics (e.g., enthalpy) of Li segregation. This will enable us to realistically assess the potential benefits of the Sn-Li system as a plasma-facing material.

PISCES-B Experiments with Li (UCSD)

Contributed by R. Doerner
University of California, San Diego

Deuterium Recycling from Liquid Lithium

Much of the recent work with lithium in the PISCES Laboratory has focussed on the retention properties of lithium exposed to deuterium plasma bombardment. One of the proposed advantages of using a liquid-lithium wall in a plasma environment is its potential ability to provide a low-recycling boundary condition for a confined plasma. If a low-recycling wall can be achieved, one expects there to be a dramatic increase in the edge plasma temperature. It is well known that a high edge plasma temperature will influence the core plasma profiles and provide flatter temperature and density profiles across the plasma volume. The promise that a low-recycling wall will improve the confinement of the core plasma is one of the prime motivations for investigating liquid-lithium particle removal systems.

Early, preliminary measurements in PISCES-B of the retention capability of liquid lithium showed that only a small fraction of the incident deuterium ion flux was retained within the liquid sample. However, impurity surface layers formed on the reactive lithium surfaces hindered these early measurements. After developing in-situ techniques to produce pristine lithium surfaces, recent measurements now show full retention of all incident deuterium ions onto the liquid-lithium surface. In fact, the total number of deuterium atoms retained appears to be slightly larger than the integrated incident ion flux, a result that may be due to the absorption of energetic deuterium atoms incident on the lithium surface during plasma exposure. Low recycling continues until the lithium sample becomes fully hydrided (i.e. 50% Li, 50% D), at which point the retention saturates and high recycling occurs. Figure 1 shows retention data from a series of lithium samples exposed to varying fluences of deuterium plasma in PISCES-B.

Deuterium retention in the lithium samples is measured using Thermal Desorption Spectroscopy (TDS) after the samples have been removed from PISCES-B and placed in a small vacuum oven. Future measurements of the outgassing characteristics of deuterium-containing lithium samples will be made to determine the deuterium recombination rate coefficient in lithium as a function of the surface temperature. By varying the heating profile during TDS, a series of plateau levels in the deuterium outgassing can be observed as shown in Figure 2. By assuming that the deuterium concentration at the surface does not change appreciably during the course of the TDS one can use the plateau level to measure the recombination rate of deuterium in liquid lithium at different temperatures.

Mechanisms for Material Removal from Lithium Samples

A comparison has been made between data collected from quantitative lithium experiments at UCSD, University of Illinois and from the DiMES experiment at GA. The samples compared were all in the solid lithium state. Since each of the facilities measures somewhat different quantities some corrections to the available data had to be made. Figure 3 shows the comparison of the three sets of data normalized to show the erosion yield of lithium vs. deuterium ion energy at an angle of incidence of 45-60° with respect to the surface normal. The following corrections were imposed to be able to plot the data on the same graph. The DiMES experiment assumes that the incident ion energy equals 5 times the measured electron temperature at the divertor plate. The UI data has been multiplied by a factor of 1/3 to account for only the fraction of sputtered particles lost from the surface as neutrals. The PISCES data was multiplied by a factor of 6 (obtained from J. Laszlo and W. Eckstein, JNM 184 (1991) 22.) to account for the variation from normal incidence to 60°. As can be seen, the data from all three facilities is consistently lower than that predicted by Laszlo and Eckstein using the TRIM Monte-Carlo code.

Measurements continue attempting to understand the enhancement of erosion during plasma bombardment of liquid samples. Figure 4 shows the results of a flux scan on the erosion rate of lithium samples as their temperature increases. The increase of erosion yield is seen to be independent of the incident plasma flux, indicating that the loss mechanism is tied to the incident ions. Research into possible explanations for this behavior is continuing.

In addition to material loss due to erosion mechanisms, macroscopic material can be lost from liquid samples due to JxB forces in a plasma environment. Liquid surfaces have little resistance to forces applied and this may tend to be the most restrictive constraint on the use of liquids in a plasma environment. Such macroscopic ejection of material has been described in this report in the DiMES section. Observations from the liquid lithium limiter on CDX-U have also shown droplet ejection from the molten lithium surface. Figure 5 shows the time history of some lithium droplets lost from the limiter during a plasma discharge. The droplets can be seen as the bright dots (viewed through a Lithium I line filter) changing positions in the figure, against the stationary background of plasma interacting with the limiter surface. The trajectory of the droplets is being analyzed to understand their motion in the plasma and to estimate their ejection velocity for comparison to the JxB forces present in CDX-U. Droplet formation is observed in virtually all discharges in contact with the limiter, but their severity and the size of the droplets seems to vary. In contrast to the DIII-D DiMES results, during none of the CDX-U discharges did the presence of lithium droplets lead to a plasma disruption.

To date all the experiments performed by the PISCES research team have involved the use of stationary liquid targets. A design effort has also recently begun toward developing a system capable of delivering a flowing liquid sample for experimentation in the PISCES Laboratory. It is hoped that these preliminary designs and experiments will lead to deployment of a flowing system based on this effort in CDX-U, and eventually to a larger confinement device.

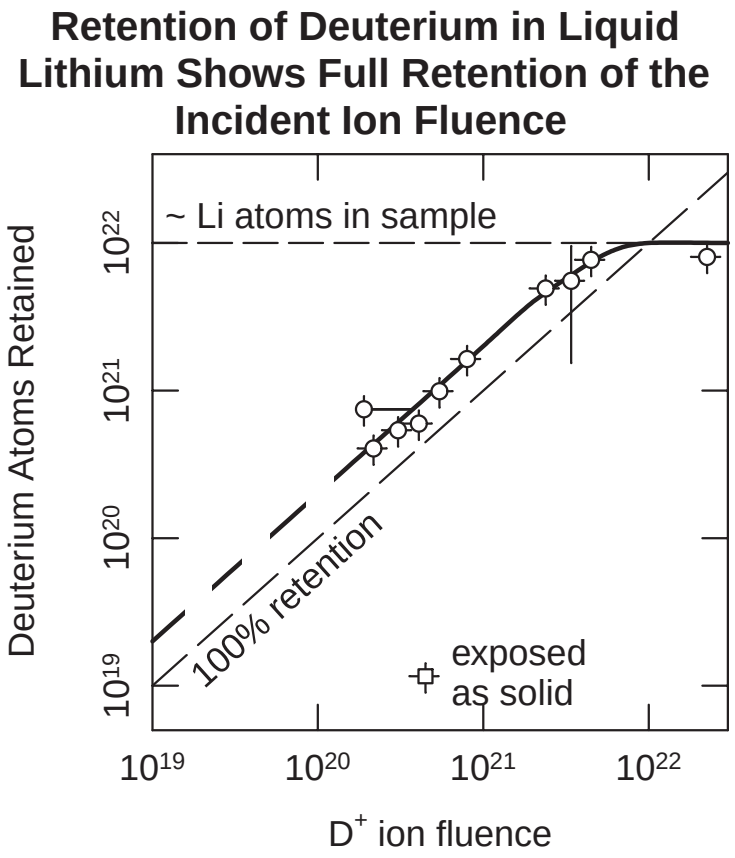

Figure 1. Deuterium atoms retained within static liquid-lithium samples (1 cm^2 x 0.3 cm deep) exposed to deuterium plasma bombardment in PISCES-B shows the very low deuterium recycling properties of liquid lithium. For comparison, the retention in a solid-lithium sample is also shown in the figure.

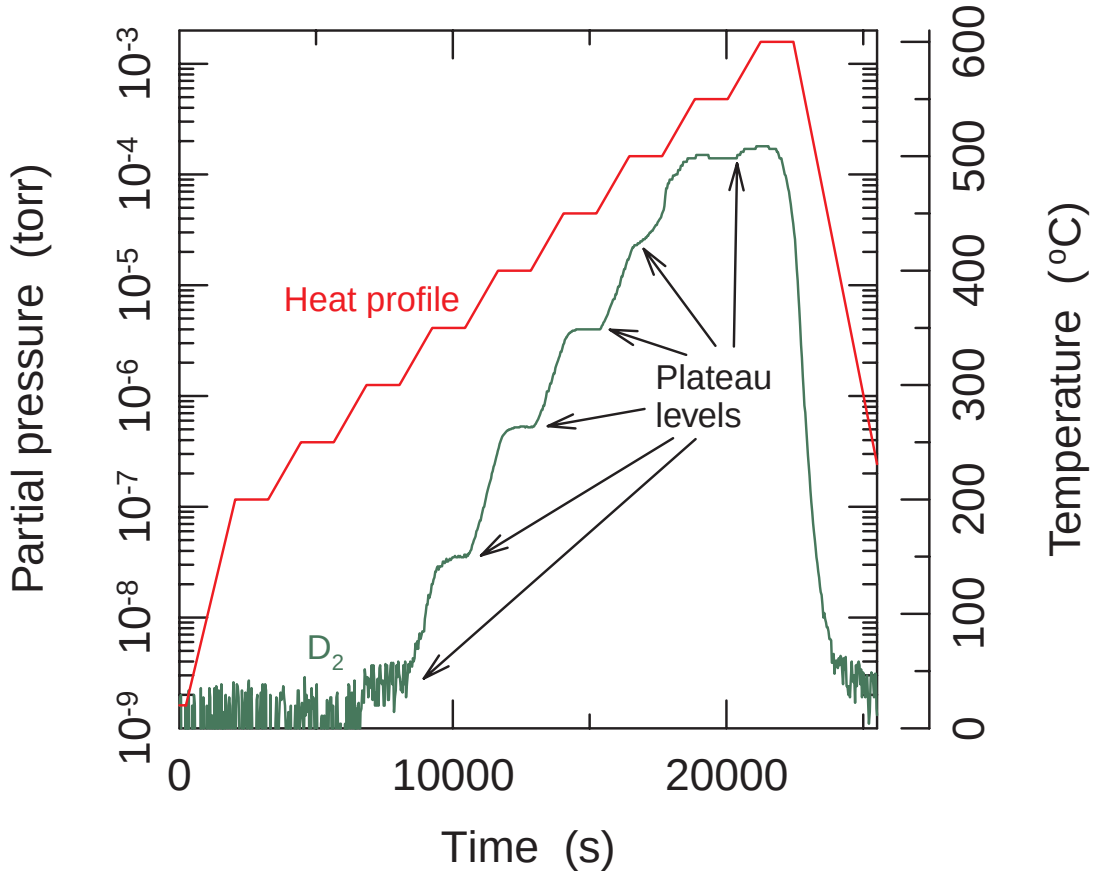

Figure 2. Controlled outgassing from deuterium containing lithium samples may allow a direct measurement of the recombination rate. By assuming that the deuterium concentration at the surface does not change appreciably during the outgassing, the plateau levels observed can be equated to the recombination rate constant.

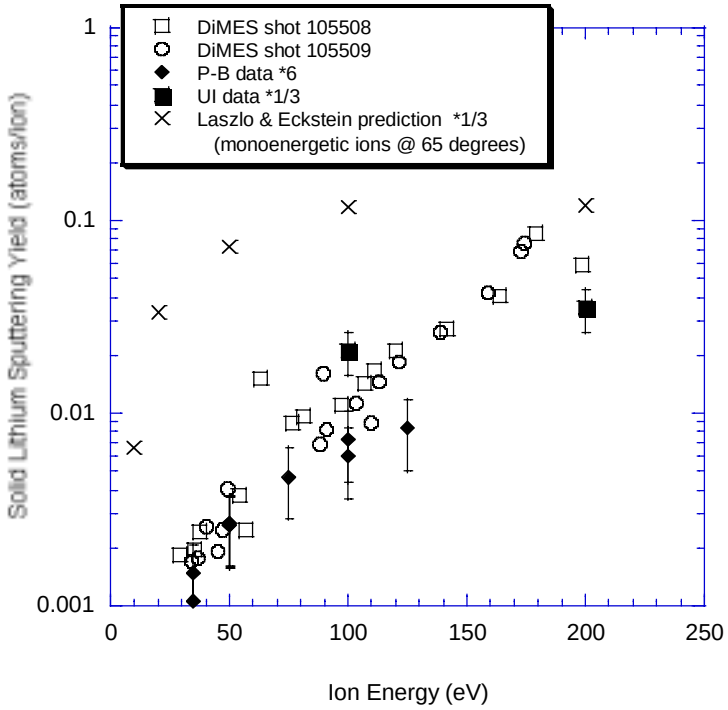

Figure 3. Neutral lithium atom sputtering yield measured on solid lithium shows good agreement between DiMES, PISCES-B and IIAX (University of Illinois) data, but all three are consistently less than the yield predicted by TRIM modeling.

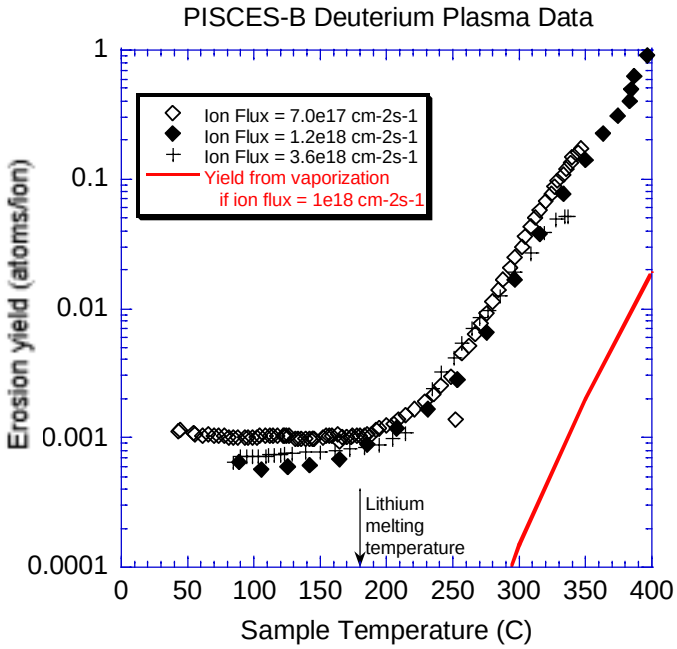

Figure 4. Erosion yield of liquid lithium samples depends on the surface temperature of the sample and is independent of incident ion flux.

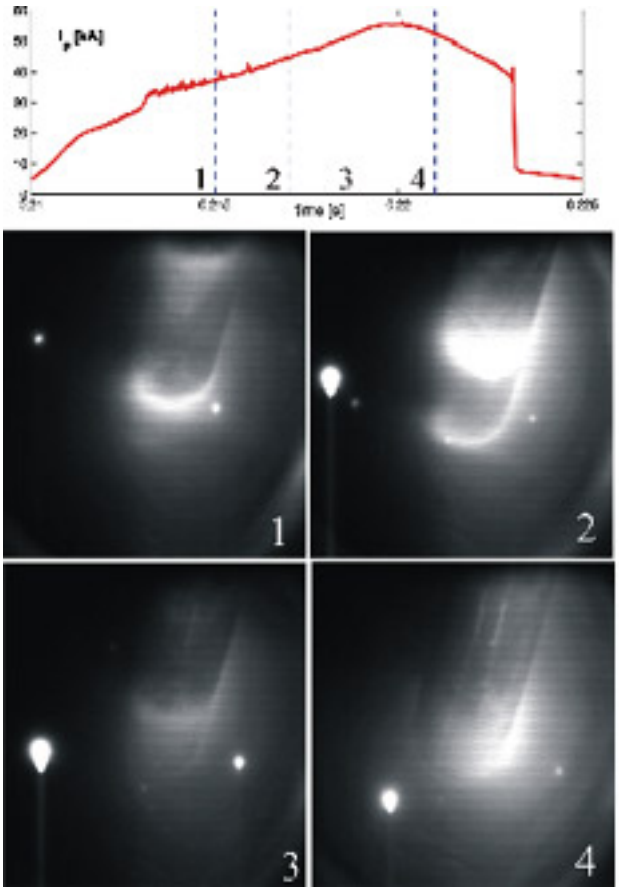

Figure 5. Neutral lithium line emission images from a fast camera viewing the plasma interaction with the liquid lithium limiter in CDX-U reveals the existence of droplets being ejected from the liquid surface. JxB forces are thought to be responsible and may prove to be the limiting constraint on liquid surfaces employed in a plasma environment.

IIAX Experiments with Liquid Li and Sn-Li (UIUC)

Contributed by J.P. Allain and D.N. Ruzic
University of Illinois, Urbana-Champaign

Objective

One of the critical issues in the design of liquid-metal divertor systems is the erosion behavior of a liquid-metal surface from bombardment of impinging ions. Therefore, one of the primary objectives is to obtain a fundamental understanding of the erosion processes of candidate liquid metal materials such as lithium and tin-lithium. The absolute lithium-sputtering yield in the solid-phase from D^+, He^+, and Li^+ bombardment at 45-degree incidence has been successfully measured [1]. The next objective is to measure the absolute lithium-sputtering yield from liquid-phase lithium and tin-lithium surfaces. VFTRIM-3D simulation is utilized to gain further insight into the physical processes, which occur during ion bombardment of candidate liquid-metals. The simulation model will be briefly discussed here and will be treated thoroughly in the plasma-material interaction modeling section of this report.

Summary

The absolute lithium-sputtering yield of liquid phase lithium and tin-lithium from bombardment of Li^+, He^+, and D^+ has been measured by IIAX at 45-degree incidence and incident energies in the range of 200-1000 eV. The temperature dependence of liquid tin-lithium sputtering from helium and deuterium bombardment has been measured for incident particle energy at 700 eV. The temperature dependence for helium bombardment of liquid lithium has been measured as well. In addition to the measurement of lithium sputtering, the secondary ion-fraction of lithium sputtering at a variety of conditions including variation in surface temperature and deuterium treatment has been measured. Measurements conclude that liquid-phase sputtering does not vary much from solid-phase sputtering at $T/T_m \sim 1.0$, however at $T/T_m > 1.5$ the lithium sputtering yield is anomalously enhanced at low incident energies. In addition, the secondary ion-fraction of sputtered lithium atoms is about 2/3 for both liquid lithium and liquid tin-lithium under various surface conditions.

Experimental Design and Setup

The Ion-surface InterAction Experiment (IIAX) is designed to measure the absolute, angular resolved and self-sputtering yields of many particle/target combinations [1-3]. A Colutron ion source is used to create and accelerate gaseous or metal ions onto a 0.018 cm^2 liquid metal target. Gaseous ions are obtained by means of electron-impact ionization while the lithium metal ions are obtained by thermionic emission from a LiCl powder. The bombarding ions are mass-selected through an E X B filter and decelerated

near the target by a five-element cylindrical electrostatic lens system. Complete details of the system can be found in published papers [1-3].

Liquid lithium sputtering

Figure 1 shows results for Li^+, He^+ and D^+ bombardment of liquid lithium at 45-degree incidence [2]. All sputtering yields for liquid lithium are greater than sputtering from lithium in the solid state. In both cases the relative low absolute sputtering yield of Li is directly related to the saturation of the surface by deuterium atoms. In the case of the solid phase, preferential sputtering mechanisms dominate the physical sputtering yield. In the case of lithium in the liquid phase, the relative bonding between atoms dominates the absolute sputtering of Li atoms.

Deuterium bombardment exhibits different maxima depending on the state of lithium. This suggests the enrichment of deuterium atoms in the bulk of liquid lithium shifting the maximum of the nuclear stopping cross section to higher energies.

The effect of deuterium saturation varies from the solid to liquid phase. Experimental data show that for solid lithium the sputtering yield of Li atoms is significantly decreased by saturation of the surface [1]. In contrast, although there is a strong solubility of deuterium in liquid phase lithium, D atoms readily migrate to the bulk and thus a larger lithium yield is obtained. In addition, the surface binding energy is effectively decreased by an increase in temperature.

Comparing the experimental results for liquid lithium to VFTRIM-3D modeling one notes the significance of Li-D bonding. Using other surface binding and bond energy models are not able to predict the experimental data. Use of the heat of enthalpy of Li-Li and Li-D bonds and the temperature adjusted surface binding energy gives the proper sputtering yield behavior. As the temperature is increased, we expect the sputtering yield of liquid Li to increase. Experimental results as a function of temperature will be the subject of a paper to be submitted in the near future.

Liquid tin-lithium sputtering

Figure 2 shows the results for Li^+, He^+ and D^+ bombardment of liquid-phase tin-lithium at 45-degree incidence [3]. The largest contribution to the absolute sputtering of lithium comes from bombardment by lithium ions onto liquid 0.8 Sn-Li. The maximum absolute sputtering yield of Li by Li bombardment is about a factor of two greater for helium bombardment and a factor of four greater for deuterium bombardment. This is due to a greater transfer of energy between Li bombarding ions and Li atoms on the surface, compared to D and He bombarding ions. In addition subsurface layers containing 80 a/o Sn act as a reflective wall thus leaving incident bombarding particles as highly-energetic backscattered particles, leading to more lithium sputtering. For example, incident Li atoms transfer about 16% of their energy to sub-surface Sn atoms and incident He atoms, 10%. This leaves backscattered Li and He atoms with sufficient energy to cause significant sputtering of surface Li atoms. Greater sputtering results from lithium bombardment due to their larger mass.

All sputtering yields for liquid tin-lithium are larger than those on pure lithium in liquid phase. This is primarily due to the fact that lithium is preferentially sputtered from the subsurface layers containing 80% Sn and 20% Li. In the case of pure liquid lithium, subsurface layers contribute very little lithium to the sputtering yield since in that case, deuterium is preferentially sputtered. Since solubility of deuterium in liquid tin-lithium is relatively low its contribution in decreasing the absolute sputtering yield of Li is also very low. Furthermore, the subsurface Sn-Li reflective wall as discussed above leads to greater lithium sputtering on the basis of energy transfer mechanisms. For example the maximum energy transfer factor for D atoms on Li is 0.70 compared to 0.066 for Sn.

In addition, due to preferential sputtering mechanisms, the relative bonding between atoms in liquid tin-lithium is critical. As in liquid lithium, in tin-lithium the surface binding energy is effectively decreased by an increase in temperature. However, for subsurface layers the effective surface binding energy is higher which, accounts in part for the almost non-existent sputtering of Sn from the surface.

Again as in the sputtering of pure liquid lithium the ion fraction of sputtered atoms is important and is discussed in the next section. Particles that sputter as ions will be quickly returned to the surface because of the plasma sheath. For the case of liquid tin-lithium, the ion fraction is measured to be 65% compared to < 10% for solid tin-lithium. This relatively large ion fraction coincides with those measured in pure liquid lithium [1]. This provides further evidence that Li atoms segregate to the surface of liquid tin-lithium and behave similar to pure liquid lithium.

These results indicate that 0.8 Sn-Li may be an ideal plasma-facing component for future high-heat flux fusion devices. The desirable low Z and high ion fraction of the sputtered flux is present due to the Li segregating to the surface. However, the disadvantages of a Li surface --- high evaporation rate, low boiling point, and high tritium retention --- are absent.

Secondary sputtered ion-fraction from liquid lithium and tin-lithium sputtering

Figure 3 shows the incident particle energy dependence of the secondary sputtering ion-fraction of lithium atoms from liquid lithium and liquid tin-lithium sputtering. The measurements shown are done for helium sputtering at 45-degree incidence. These fractions were also measured for deuterium and lithium bombardment and show similar results. Note that the ion fraction of sputtered atoms plays an important role on erosion characteristics of liquid lithium. Sputtered Li ions will never penetrate to the core plasma due to the sheath at the edge. In the case of liquid phase lithium and tin-lithium, about 65% of the sputtered Li atoms come off as an ion.

Temperature dependence of liquid lithium and tin-lithium sputtering

Figure 4 shows results for the temperature dependence of liquid lithium and liquid tin-lithium sputtering on surface temperature. As the temperature of the surface is raised to temperatures of the order 1.5-2.5 T_m, an increase in the physical sputtering yield is

measured. This increase already accounts for the increase in lithium erosion due to *evaporation* as measured by the QCO microbalance. This anomalous increase has also been measured in PISCES-B [4]. This temperature dependence is relevant in considering an operating temperature window for potential plasma-facing components of advanced fusion systems [5-7].

Sputtering theory states that the probability for a lattice atom to become sputtered is largely dependent on the transfer of energy from the incident particle to the underlying lattice, as well as the surface potential this atom must overcome before being sputtered. There are several factors believed to explain enhanced erosion of a liquid metal as the surface temperature is increased. These include: the topology of the surface, damage distribution theory as it pertains to compositional variation of the surface during bombardment, local enhanced liquid-metal evaporation or thermal sputtering and bubble formation. All these factors (not exclusively) may be relevant to both pure lithium and tin-lithium liquid metal sputtering enhancement with surface temperature.

The topology of the surface has been found to be an important factor for liquid metal sputtering [8]. Structure factor measurements and modeling of liquid metals show that the liquid vapor interface is not a smooth transition as that originally thought [9-13]. In fact, an underdense region of atoms is measured near the liquid/vapor interface, which is modeled by Morgan using molecular dynamics, finding that such atoms lead to an effective increase in the sputtering yield of the liquid metal. The question remains as to the dependence of this stratified region with surface temperature and its effect on physical sputtering.

Measurements have shown that deuteration of a lithium surface dramatically influences the sputtering yield of lithium due to preferential sputtering [1]. According to damage distribution theory developed by P. Sigmund and others, several primary and secondary effects may play an important role in the temperature dependence of the sputtering yield. Primary effects include preferential sputtering and ion implantation. Secondary effects include radiation induced concentration variation such as Gibbsian segregation and radiation enhanced diffusion. On one hand, segregation of the lower surface tension component in the liquid metal matrix begins. This leads to large numbers of deuterium atoms, in the case of D-soaked lithium, to reach the surface combine as D_2 molecules and desorb from the surface. On the other hand, diffusion of deuterium in the lithium BCC lattice is activated and D atoms readily diffuse to the lithium bulk. In addition, implanted deuterium recoils are preferentially implanted near the lithium matrix surface. Thus a balance of deuterium concentration is established in steady state, and as the temperature increases the net number of deuterium atoms on the lithium surface decreases. Therefore, due to preferential sputtering mechanisms [14] the absolute sputtering yield of lithium increases.

Another effect is localized evaporation enhancement or thermal sputtering. Work on temperature-dependent sputtering dates back to the work of M.W. Thompson and R.S. Nelson in their study of thermal spikes [15,16]. Additional work in the area of thermal sputtering was conducted by R. Kelly [17], K. Besocke et al [18] and M. Szymoriski et

al. [19]. The concept of a “thermal” spike occurs when an energetic incident ion deposits sufficient energy on a solid target causing a momentary temperature increase in the impact region. Typically the creation of thermal spikes is only expected for high-energy heavy-ion bombardment where large recoil energies, and hence “hot” spikes are possible. However, measurements in IIAX (Fig. 4) and PISCES-B [4], show similar sputtering yield behavior as that seen on thermal sputtering experiments conducted in the past [15,16]. The main difference being that now the measurements are done for liquid metal sputtering as opposed to solid phase sputtering. Therefore, one may use these earlier models developed from experiments as a starting point to understand liquid metal sputtering dependence on temperature.

In addition to all these mechanisms, bubble formation is also relevant. Dose dependent measurements have shown that significant nanoscale bubble formation can lead to an effective increase in the sputtering yield of a liquid metal. This work was carried out by L.B. Begrambekov et al. in Russia [20].

In the case of liquid lithium alloys, the effects of these kinematic and thermodynamic processes are similar. The lithium atoms in the tin-lithium matrix segregate to the surface as the temperature is increased. The number of lithium atoms that segregate to the surface is increased as the temperature rises, and their net effective surface potential is decreased thus leading to a larger absolute sputtering yield. As the temperature rises, the displaced and segregated atoms become more likely to be sputtered due to the heavy tin underlayer effectively reflecting incident particles. Similar studies have been carried out by D.M. Gruen and A.R. Krauss on the effects of monolayer coverages on substrate sputtering yields [21].

Future work

Future work in IIAX will include a through investigation of the temperature dependence of liquid-lithium sputtering from bombardment of Li^+, He^+ and D^+ bombardment. This will include understanding the dependence of momentum deposition from the incident beam on the effect of temperature as well as the dependence of segregation and desorption of implanted deuterium atoms on the surface temperature. A self-consistent model will be developed calibrating VFTRIM-3D to experimental data and the incident particle energy dependence of lithium sputtering parametrized with surface temperature will be developed. Other studies will also include liquid tin-lithium and tin sputtering. In addition, bubble formation will be surveyed as pertinent in each experimental campaign.

References:

[1] J.P. Allain and D.N. Ruzic, Nucl. Fusion, submitted 2000.
[2] J.P. Allain, M.R. Hendricks, D.N. Ruzic, J. Nucl. Mater. 290-293 (2001) 180.
[3] J.P. Allain, M.R. Hendricks, D.N. Ruzic, J. Nucl. Mater. 290-293 (2001) 33.
[4] R.P. Doerner, et al., J. Nucl. Mater. 290-293 (2001) 166.
[5] J.N. Brooks, T.D. Rognlien, D.N. Ruzic, J.P. Allain, J. Nucl. Mater. 290-293 (2001) 185.
[6] R. Bastasz and W.Eckstein, J. Nucl. Mater. 290-293 (2001) 19.
[7] R.F. Mattas et al., Fusion Engineering and Design, 49-50 (2000) 127.
[8] W.P. Morgan, J.Appl. Phys. 65, 3 (1989) 1265.
[9] S.A. Rice J. Non-Cryst. Solids, 205-207 (1996) 755.
[10] M.P. D'Evelyn and S.A. Rice, J. Chem. Phys. 78, 8 (1983) 5225.
[11] M.J. Regan and P. Pershan et al., Phys. Rev. B, 55,23 (1997) 15874.
[12] M.H. Shapiro et al., Nucl. Instrum. Methods B13 (1986) 348.
[13] D.Y. Lo and T.A. Tombrello, Nucl. Instrum. Methods B17 (1986) 207.
[14] P. Sigmund, Mat. Fys. Medd. Dan. Vid. Selsk. 43 (1993) 255.
[15] M.W. Thompson, Phil. Mag. 7 (1962) 2015.
[16] R.S. Nelson, Phil. Mag. 11 (1965) 291.
[17] R. Kelly, Rad. Effects, 32 (1977) 91.
[18] K. Besocke et al., Rad. Effects, 66 (1982) 35.
[19] M. Szymoriski et al., J. Phys. D: Appl. Phys., 11 (1978) 751.
[20] L.B. Begrambekov et al., At. Energ. (Sov. J. At. Energy) 64, 3, (1988) 212.
[21] D.M. Gruen and A.R. Krauss, J. Nucl. Mater. 123, 1-3 (1984) 1425.

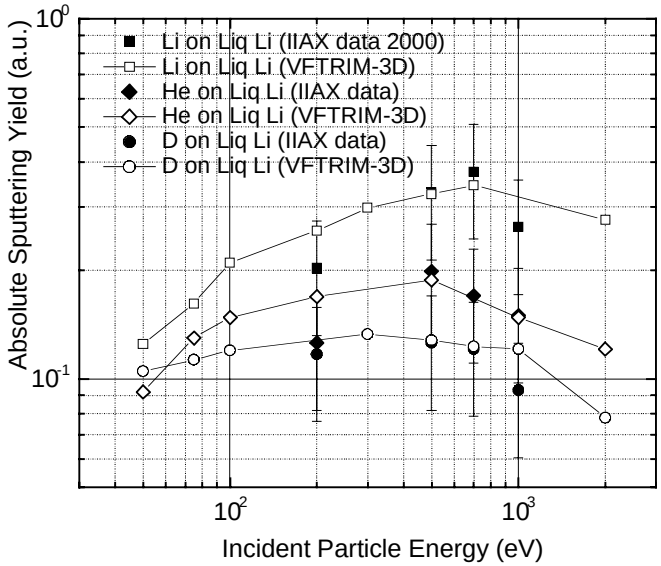

Figure 1. Li^+, He^+ and D^+ bombardment of liquid-phase lithium at 45-degree incidence measured in IIAX (Ion-surface interaction experiment). Plotted with experimental data is VFTRIM-3D simulation data.

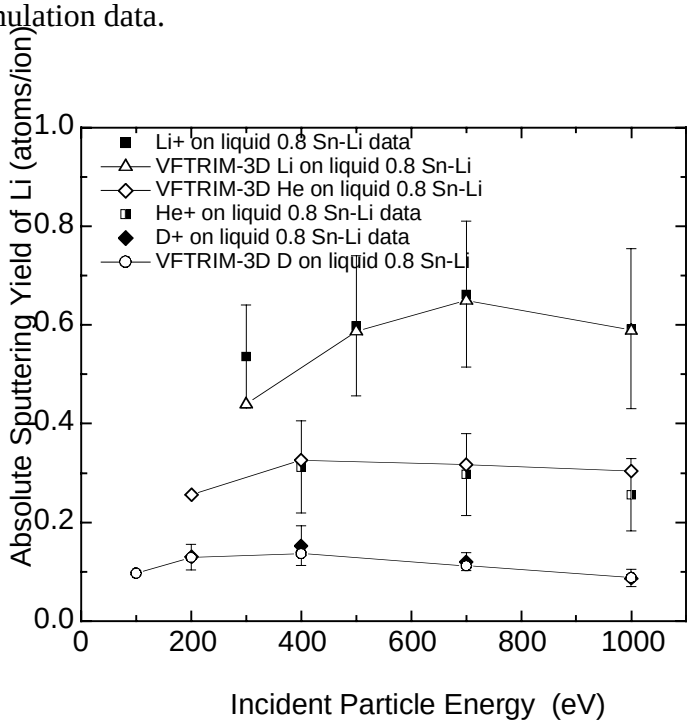

Figure 2. Li^+, He^+ and D^+ bombardment of liquid-phase tin-lithium at 45-degree incidence measured in IIAX (Ion-surface interaction experiment). Plotted with experimental data is VFTRIM-3D simulation data.

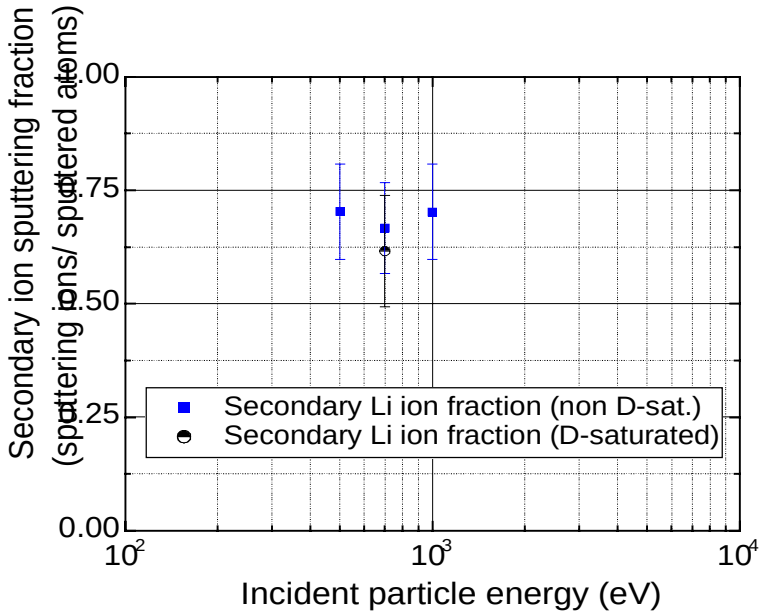

Figure 3. Secondary sputtered ion-fraction for liquid-phase lithium sputtering from helium bombardment at 700 eV and 45-degree incidence.

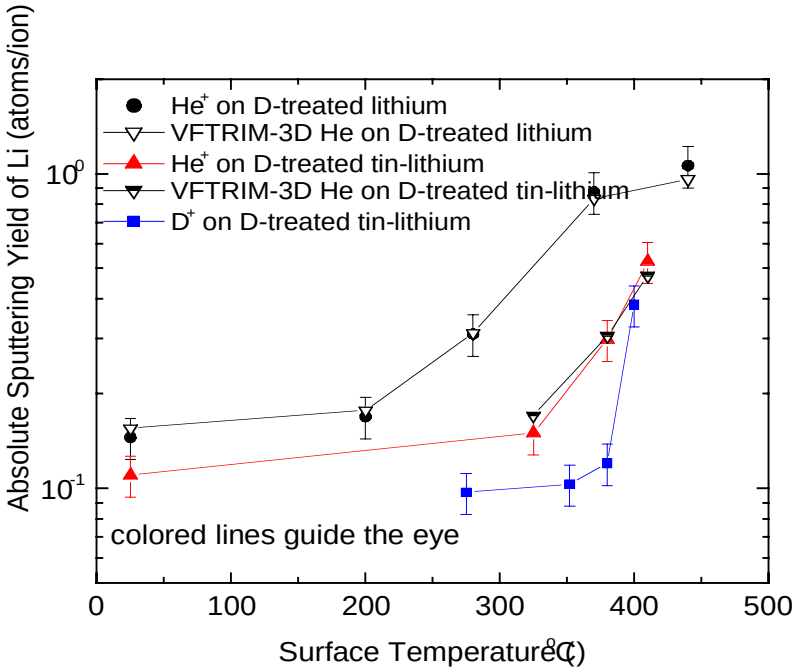

Figure 4. He^+ and D^+ bombardment of liquid-phase tin-lithium and lithium at 45-degree incidence measured in IIAX (Ion-surface interaction experiment) as a function of surface temperature. Plotted with experimental data is VFTRIM-3D simulation data.

3.0 Tokamak Experiments

Lithium Experiments in US Tokamaks

Significant progress has been made in the understanding on the use of lithium surface in tokamak devices. A summary and three reports follow.

Summary

R. Kaita of PPPL prepared the report on "Initial Experiments with the UCSD liquid lithium limiter in CDX-U". Hydrogen recycling of the lithium wall was found to be much reduced but not eliminated with a fresh solid lithium limiter. Argon Glow Discharge Cleaning (GDC) was found to be most effective in cleaning the liquid lithium limiter surface, which is reflected in the best vacuum pump out rate. Lithium-I emission was shown clearly when the lithium was interacting with the plasma. The effect of lithium getting of oxygen was also clearly shown. Droplets of lithium were occasionally observed with the liquid lithium limiter, but no disruptions occurred. Comparing to the DIII-D DiMES' radiative disruption result, this could be due to the relative low electron temperature of the CDX-U plasma, which allows a relatively long lithium ablation mean free path, reducing the deposition and ionization of the lithium in the plasma core as discussed in the report by Whyte. A toroidally continuous lithium tray at the lower divertor has been fabrication. Experiments with this lithium tray will provide crucial information on the possible MHD interaction of the lithium with the plasma, when the liquid lithium is toroidally continuous and electrical and thermal contacts between the melted lithium and the stainless steel tray are much higher than the Li-DiMES experiment.

D. Whyte of UCSD prepared the report on the "Exposure of solid and liquid lithium in the DIII-D tokamak using DiMES". To summarize the large amount of experimental data on the lithium interaction with low power L-mode, ELMing H-mode and locked mode plasma discharges the report is written as explanations and descriptions to the key reported viewgraphs. Based on measured data it appears that the contribution from physical sputtering yield of lithium is sufficiently low for it to be considered as an acceptable plasma-facing material in the tokamak. The remainder of the report emphasis is on the displacement of liquid surface due to JxB MHD effects. On all the MHD interactions, essentially all solid lithium coatings were heated to liquid state by the plasma, removed and distributed to the surrounding surface and some went into the plasma core. Movement of the liquid lithium and the emission of neutral and ionized lithium radiation in the scrape off layer, in the divertor region and in the core were clearly recorded from the very different plasma discharges. The injection of lithium into the plasma core under the low power L-mode discharge and the subsequent cause of a locked mode disruption were most unexpected. The source of the driving current is due to the presence of the tokamak parallel current and the current density is enhanced by its interception with the non-uniformity of the lithium surface. The liquid metal group from UCLA is modeling this MHD effect. More detailed assessment of the lithium injection and its similarity with the physics of pellet injection is given in the third report by Evans. This low power L-mode experiment also indicates the enhanced impact from radiation of lithium in the core when the plasma temperature is > 1 keV. It shows the detrimental

impact to the energy balance of the plasma core, and provides the plausible explanation on why the radiation collapse effect was not observed in CDX-U and T11-M experiments when the lithium droplets were passing through the core.

T. Evans of GA prepared the report on "The Analysis of a DIII-D disruption sequence induced by a small lithium sample subjected to a low power L-mode plasma". The low power L-mode plasma discharge was analyzed carefully. The key diagnostics used for this analysis are the DIII-D tile current array located at the same major radius as the DiMES sample and the SPRED system, which monitors the time evolution of the lithium radiation in the core plasma. The reduction and recovery of the tile current indicates the modification and re-establishment of the parallel current at around the time when the lithium was melted. It confirms the possibility that the parallel current is the source of current density, J, which caused the movement of the liquid lithium on the DiMES sample surface and the subsequent change in direction in the lithium as return current, which led to the enhanced JxB effect that injected the lithium into the plasma core. The enhancement of J in the melted lithium is most likely due to the interception of the parallel current by the non-uniformity of the lithium surface in the order of mm scale. Whereas this non-uniformity is most likely caused by the initial lithium movement over the lid of the lithium cup. It is interesting that the injected lithium blob behaves very similar to the injection of lithium pellet. The timing and quantification of radiation in the core and the subsequent generation of locked mode, energy deposition and ionization in the plasma core can then be explained.

Results from the DiMES experiments indicate the MHD effect will cause movement of a melted lithium coating. When the parallel current is intercepted by the non-uniformity of a the lithium surface, the current density can be enhanced and re-directed in such a direction that the JxB effect can cause a radial injection of lithium into the hot plasma core and cause a radiative collapse and lead to a disruption. The DiMES results suggest that the MHD effect could be a critical issue and must be resolved. But how strong an influence on the disruptive result is due to the limited geometry, and limited thermal and electrical contacts of the lithium in the DiMES graphite cup remains to be analyzed. These experimental and modeling results will be compared to the toroidally continuous lithium tray experiment to be performed by CDX-U. The UCLA/GA/UCSD MHD modeling would be an essential next step to project the results from the CDX-U experiment, and to assess the merits of using liquid metals as the plasma-facing material in reactor relevant tokamak divertor configuration. Further experiments can then be proposed to study the avoidance of this detrimental form of liquid metal MHD effect inside the tokmak plasma chamber.

Initial Experiments with the UCSD Liquid Lithium Limiter In CDX-U

Significant physics and engineering problems need to be addressed before liquid metals can be considered a viable solution to the plasma wall problem. As a step toward this goal, the first experiments involving the use of solid and liquid lithium as a plasma limiter in CDX-U have recently begun, utilizing a lithium covered rail 5 cm in diameter, 20 cm long which was developed at UCSD. The lithium limiter can be inserted or removed via a double gate valve airlock system to prevent exposure of the lithium to air. When the limiter is fully inserted, it forms the upper limiting surface for the discharge and is intended to define the last closed flux surface for the discharge. If the limiter is retracted, ceramic boron carbide rods form the upper limiting surface for the discharge. The limiter has an internal heater and has been operated in contact with the plasma over the temperature range of 20 - 260^{o} C.

The results of the first operation of CDX-U with a solid lithium limiter are shown in Fig. 1. Here we compare the D-α emission at the limiter surface with a lithium coating which has not been previously exposed to plasma, to the emission from a lithium coating which has been deuterated by exposure to plasma and gas puffing. Note that although recycling is markedly reduced for the case of initial operation with a solid lithium limiter, it is not eliminated. We have not yet observed any condition, for liquid or solid lithium over the ~20 - 260^{o} C temperature range, for which recycling is completely eliminated. At this point it is unclear whether surface impurities may be responsible for the residual recycling.

The deuterium prefill required to obtain breakdown was 60% higher in the case of a "fresh" lithium surface than for either the deuterated case, or for normal operation with high recycling boron carbide limiters.

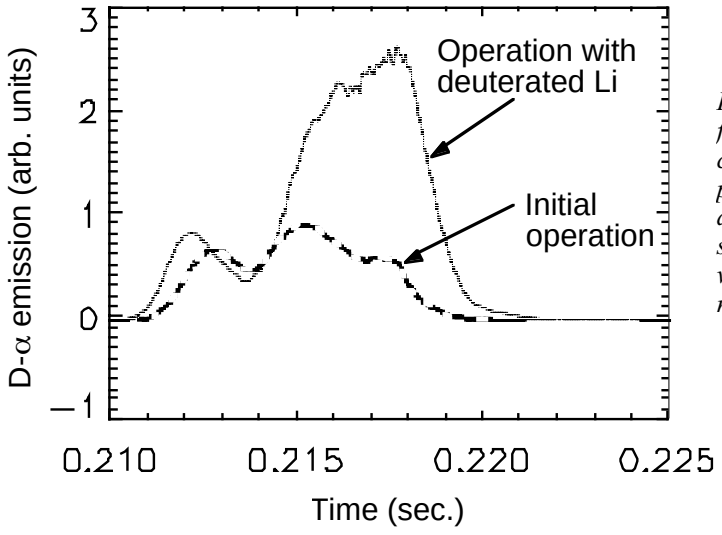

Figure 1. Recycling comparison for a "fresh" lithium limiter coating (exposed to a base pressure of 3 x 10^{-7} T but not deuterated) and a deuterated surface. Discharge line density was identical to 5%; traces are normalized to the plasma current.

Surface cleanliness has been a significant issue. Glow discharge cleaning (GDC) in an argon glow with the lithium rail limiter serving as the cathode has been found to be reasonably effective at removing visible surface coatings. Ion bombardment is sufficient to liquefy the lithium and heat the surface to 200 - 300^{o} C. GDC is most effective if the lithium is liquefied.
Deuterium pumping by the limiter is significantly enhanced following an argon glow. Pumpout rates following a tokamak discharge are compared for the cases of a freshly discharge cleaned and a deuterated lithium limiter in Figure 2. The upper two curves are for a solid lithium limiter and the lowermost curve is for a liquid limiter, which appears to show the best pumpout rate.

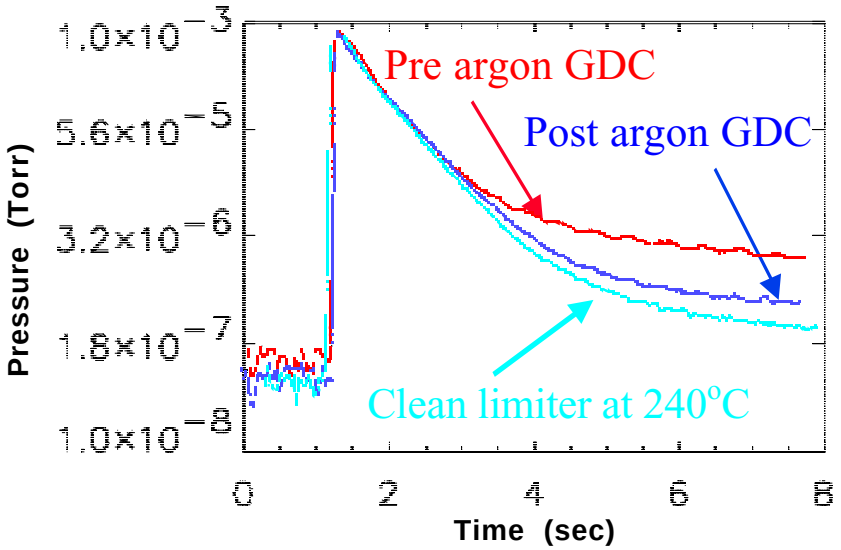

Figure 2. Deuterium pumpout following a discharge for a deuterated lithium limiter and a freshly discharge cleaned surface.

Significant lithium influx has been observed in discharges using the liquid lithium limiter. In these experiments, the limiter was kept at 250^{o} C, which is above the melting point of lithium. Spectroscopic examination of the lithium light from the surface of the limiter shows strong Li I emission at 670.8 nm during the discharge. Fast camera images of the limiter using the same lithium interference filter show clear bands of emission that correspond to contact with the plasma (Figure 3).

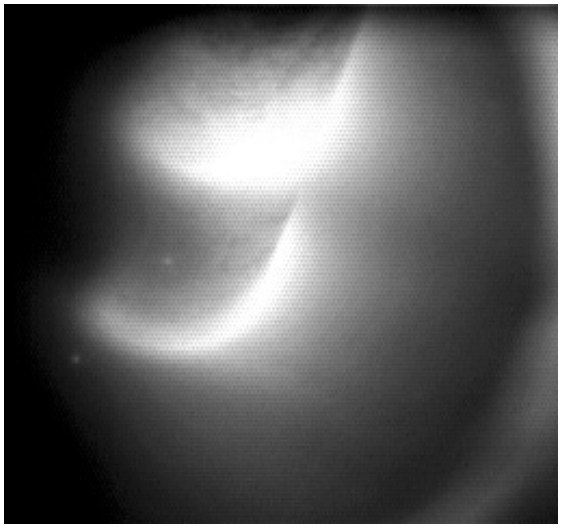

Figure 3. Image of the liquid lithium limiter taken through a lithium filter. The view shows the surface that faces the plasma at a framing rate of 1000 frames per second. The emssion is most conspicuous at the plasma contact point (upper band) and the tip of the limter heat (lower band).

Filterscope data for the 670.8 nm LiI and the 441.6 nm OII emission are compared in Figure 4 for discharges with a liquid lithium limiter after GDC (upper panel) and a solid lithium limiter (lower panel) after extended plasma operation. There is a reduction in oxygen levels, which suggests that a clean lithium surface is effective for gettering. In addition to lower emission levels with the clean limiter, the discharge is longer because of the reduced radiation losses.

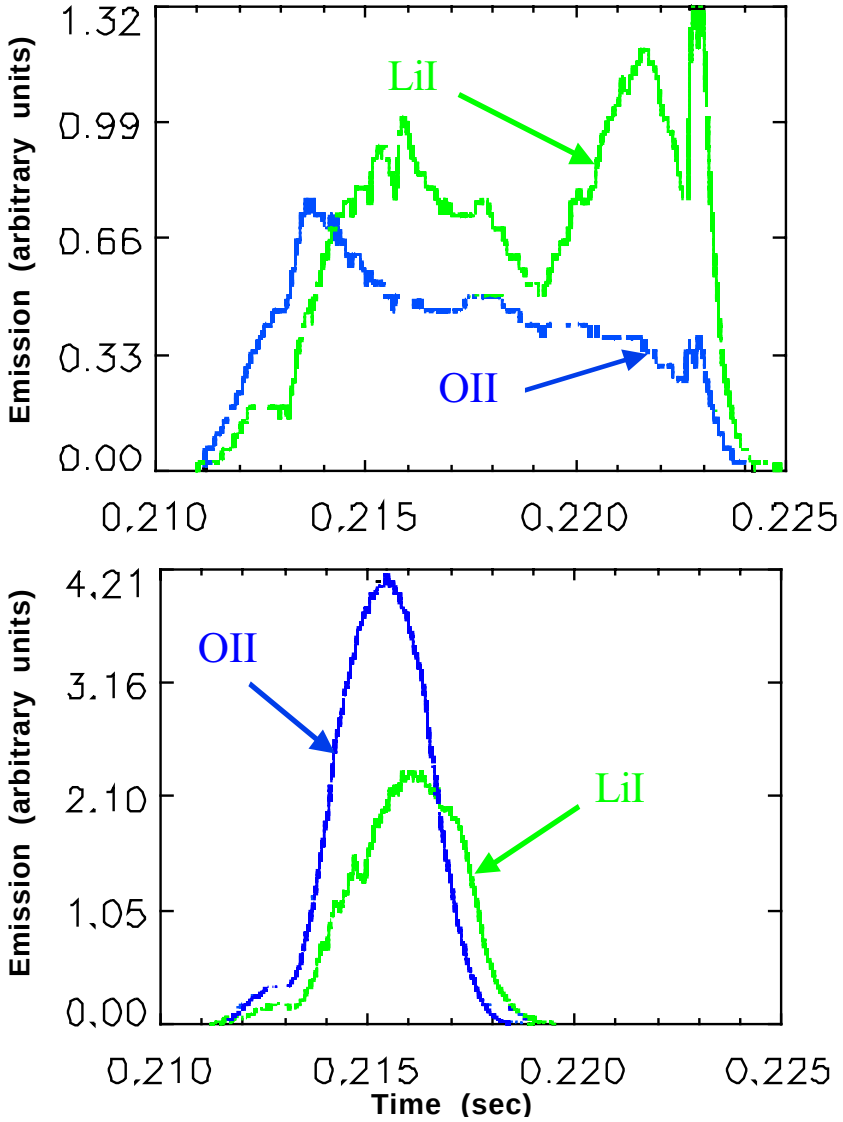

Figure 4. Comparison of oxygen and lithium emission for before (upper panel) an after (lower panel) extended plasma operation. Oxygen level decreases with time in clean limiter case, but peaks well above lithium after extended exposure to plasma.

Edge density and temperature profiles are comparable with discharges with boron carbide and liquid lithium limiters (Figure 5). Since the lithium rail limiter presents only a modest contact area for the plasma, the results suggest that the edge parameters are affected by other surfaces where recycling occurs.

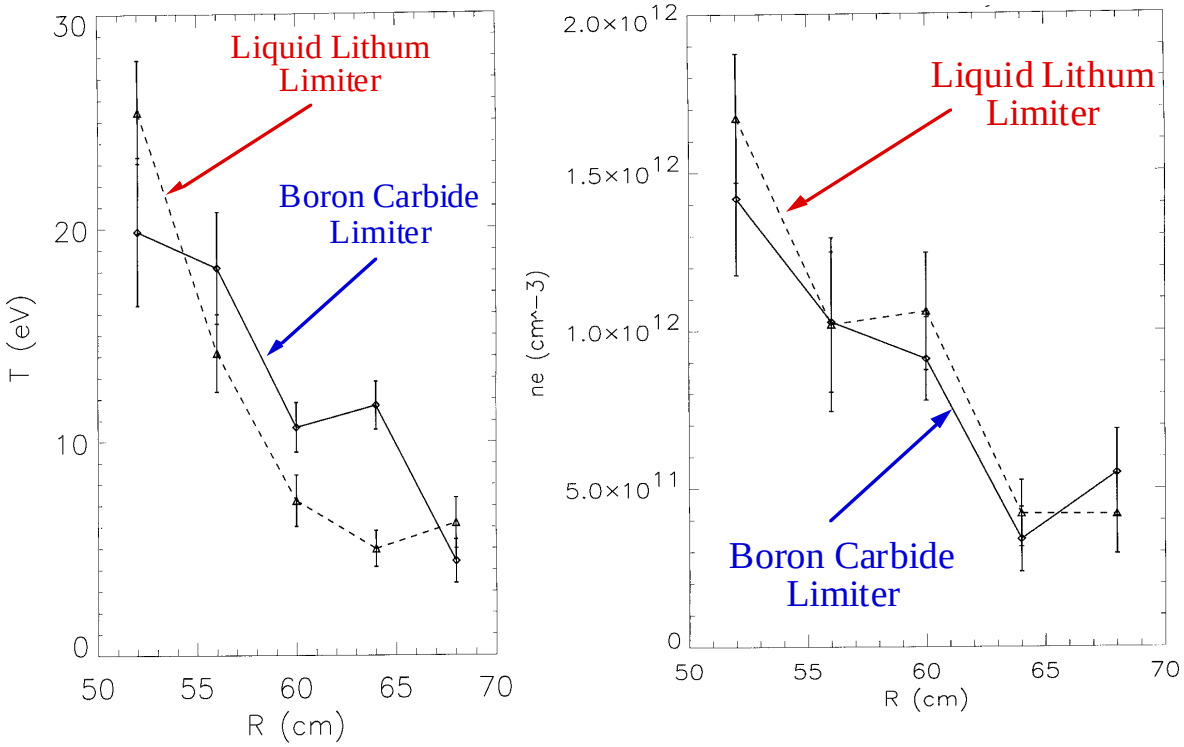

Figure 5. Edge temperature and density profiles in boron carbide and lithium limiter plasmas.

Droplets of lithium were occasionally observed with the lithium limiter operated at 250° C. The sequence of photographs in Fig. 6 were taken through LiI filter with a visible camera in the same view of the limiter as in Fig. 3. While they could be up to about a millimeter in size, as shown in the last frame, they did not disrupt the plasma. This is similar to what occurred in T-11M. Sprays of droplets were seen in lithium limiter discharges, but disruptions did not occur.

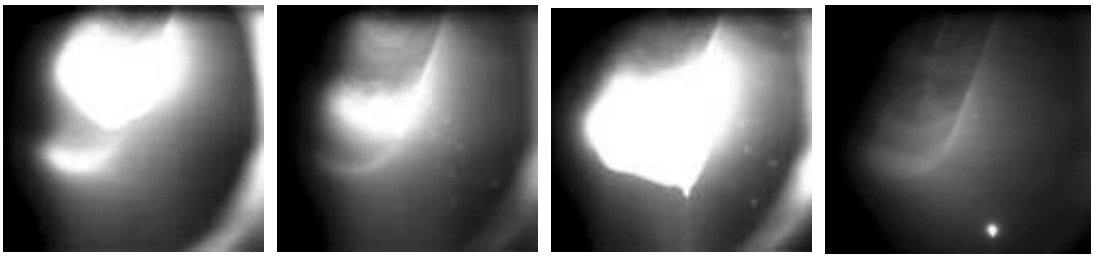

Figure 6. Camera images in 1 ms intervals showing droplet formation below lithium limiter.

After the initial experiments with the liquid lithium rail limiter were completed, the pressure inside the CDX-U vacuum vessel was first increased to about half an atmosphere of air for a couple of days. The chamber was then fully vented, and air was circulated through it for an

additional few days before any ports were removed for access. This process was sufficient to make the lithium inside the vacuum chamber unreactive.

Inside the vacuum chamber, there was a thin lithium film along a radial strip about 10 cm wide directly above the lithium limiter. Below the limiter, there was a deposit about 13 cm in diameter, and with a maximum thickness of approximately 4 mm. This was created when molten lithium dripped from the limiter during argon discharge cleaning. Both the film above the limiter and the deposit below it were restricted to disposable stainless steel foil that protected the top and bottom of the vacuum vessel. The cleaning procedure then became primarily a matter of removing the lithium with the foil. No coatings or deposits of lithium were found elsewhere, other than a few millimeter sized spheres on the bottom of the vacuum vessel.

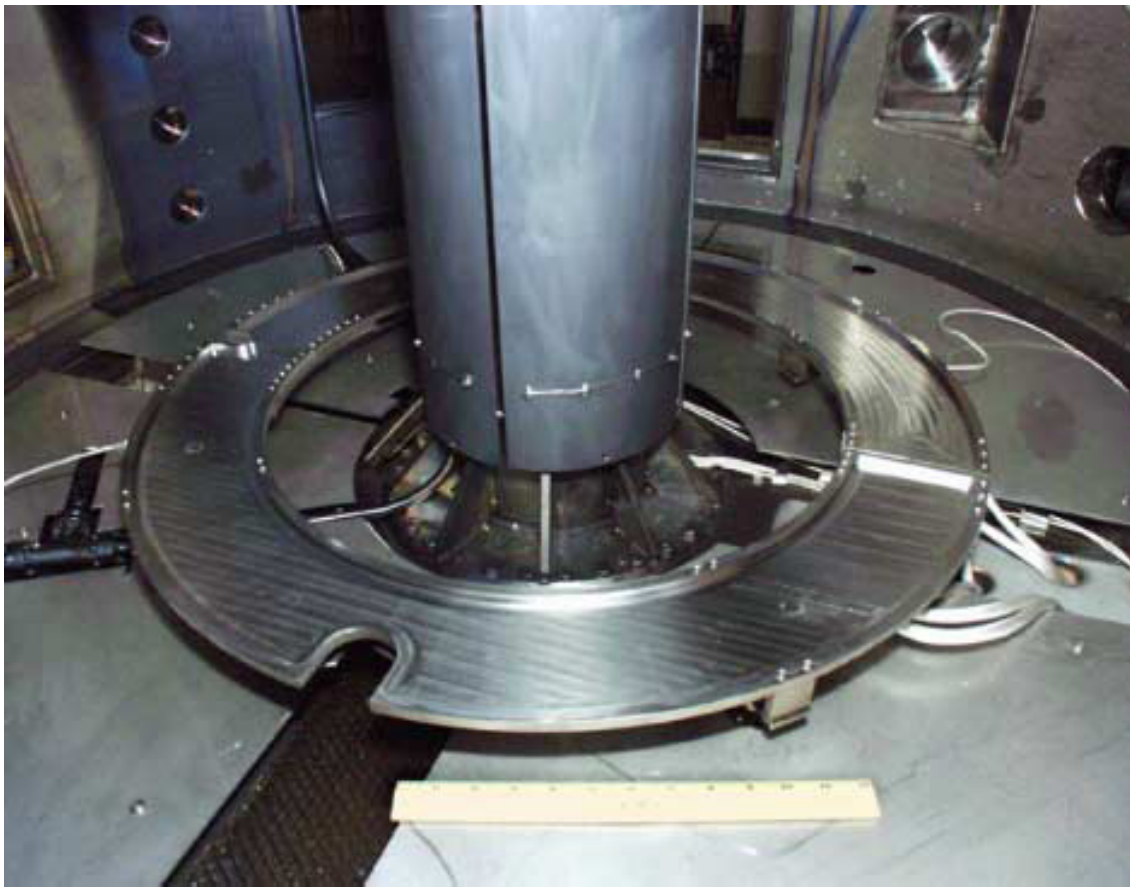

Figure 7. Photograph of new fully toroidal limiter tray inside CDX-U vacuum vessel.

A fully toroidal limiter, consisting of a 10 cm wide tray to be filled with liquid lithium, was installed in CDX-U during the vent (Fig. 7). This will increase the lithium surface area to 1600

cm^2 and the in-vessel volume to approximately 0.5 liter. The boron carbide limiters on the center stack were replaced with a heat shield that was coated with titanium carbide. A heat shield was also placed below the tray, and an array of thermocouple sensors was installed around the interior of the plasma chamber. The purpose of this next step is to investigate how a large lithium surface will affect CDX-U discharges, and study the effects these plasmas will have on the magneto hydrodynamics of the liquid lithium.

For the toroidal limiter, the first experiments will be performed only with magnetic fields to determine the effect of eddy currents on the liquid lithium. The simplest measurement is to look for any motion of the lithium with a fast visible camera. The observations can them be compared with fluid MHD calculations for the CDX-U field and limiter geometry.

Limiter plasmas can then be attempted with edge temperatures in the range of tens of electron volts. Since the discharges are short, the lithium temperature can be controlled with heaters in the toroidal tray. This enables the study the interaction of plasmas with solid and liquid limiters as a function of lithium temperature.

Vertical displacement events can also be induced by selectively eliminating poloidal fields, and the effect of a plasma striking a liquid lithium surface can be studied. These experiments will all be performed with limiter discharges. In the future, additional poloidal field coils will be added to enable divertor plasmas with strike points on the toroidal lithium surface.

This work was supported by USDoE contract DE-AC02-76-CH0-3073.

Exposure of Solid and Liquid Lithium in the DIII-D tokamak using DiMES

D.G. Whyte, ***UCSD***
C.P.C. Wong, T.E. Evans, W.P. West ***General Atomics***
R. Bastasz, ***Sandia National Laboratories***
J.P. Allain, ***University of Illinois Urbana-Champaign***
J.N. Brooks, ***Argonne National Laboratories***

Experiments

Lithium has been tested as a plasma-facing surface material in the divertor of the DIII-D tokamak using the DiMES sample changer system. Circular thin foils of solid lithium were conformed into a shallow 2.54 cm diameter "cup" on the DiMES sample surface (Fig. 1). Samples were not actively heated, relying instead on the incident plasma to heat and liquefy the lithium.

Lithium has been exposed in the solid and liquid phase to a variety of divertor plasma conditions. These include both low power L-mode and higher power ELMing H-mode discharges. The large array of plasma and spectroscopy diagnostics on the DIII-D/DiMES system has acquired high-quality data on the plasma-surface interaction of lithium in a tokamak divertor (Fig. 2). For example, we have obtained three-dimensional spatial imaging of the removed lithium fluorescing in the divertor plasma (Fig. 3), as well as high-resolution spectroscopy (Fig. 4) showing effective energy ~1.3 to 1.8 eV, of the sputtered lithium. Such data is invaluable for benchmarking sputtering and transport models, and to understand the interaction between the divertorlasma and the lithium surface. Fig. 5 compares divertor plasma and lithium brightness data between two discharges; excellent control of the plasma and high-resolution shot-to shot reproducibility is demonstrated. In the following we will summary the key observations from the solid and liquid lithium surface experiments.

Lithium physical sputtering is acceptable

As a solid, Fig. 5 shows the sputtering rate of the lithium surface. Fig. 6 shows that the effective physical sputtering yield of lithium under divertor strikepoint conditions is <10%. This is significant in that the result intrinsically includes self-sputtering due to prompt lithium redeposition and the glancing angle of incidence of the magnetic field found in the divertor, both effects that enhance the total sputtering yield. The measured yield versus incident energy compares well with scaled results from laboratory measurements. Lithium yield is also in close agreement with preliminary effective yield calculations provided by J. Brooks of ANL that include self-sputtering. Therefore, it appears that lithium physical sputtering yield, which is not expected to change significantly from solid to liquid phase, is sufficiently low to be suitable for application as a plasma-facing material in the tokamak. As with the laboratory measurements, the sputtering yield is considerably less than predicted by Laszlo and Eckstein (Fig. 6). This can be partially explained by the non-removal of ions sputtered due to the sheath; however, a full understanding of this discrepancy is not in hand. Figure 7 shows that as expected, the ionization mean-free-path for the physically sputtered lithium was found to be very small (<< 1 cm) in the divertor, very effectively shielding the core plasma from the lithium erosion.

Divertor MHD forces macroscopically remove liquid lithium

For all DiMES exposures, including L-mode, ELMing H-mode and a discharge with a locked MHD mode, upon liquefaction, the lithium was macroscopically removed from the DiMES sample due to local JxB forces caused by the interaction of the conducting liquid and the intrinsic divertor plasma currents.

Parallel Scrape-Off Layer (SOL) thermoelectric currents are an intrinsic part of poloidal divertor plasmas, and are established in the plasma from parallel potential gradients setup by poloidal temperature asymmetry (Fig. 8). The most significant location of these currents is near the separatrix due to its higher plasma conductivity. As expected, the

measured SOL current shows significant spatial variation across the divertor surface (Fig. 9). The plasma/divertor surface boundary and the available conduction paths in the vessel determine the closing path for such currents as illustrated by the schematics of Fig.10. Since these conducting paths are primarily non-parallel to the magnetic field, B, this produces JxB forces on any divertor surface components. Obviously, such forces are of concern for free liquid conducting surfaces.

Plasma MHD events (e.g. edge localized modes, ELMs) can transiently increase SOL currents by over an order of magnitude due to the sudden release of keV particles into the SOL. For the DiMES exposures, such MHD events simultaneously provide a burst of thermal energy to liquefy the lithium sample. The result is that the JxB body forces can instantly remove the liquid lithium. This is most obvious in the case of an exposure of the lithium sample to a stationary MHD mode (locked-mode); the direction and magnitude of the measured approximately radial movement (Fig. 11) agree exactly with the expected JxB direction from locally measured vertical SOL current density in the divertor plate (Fig. 9).

The MHD event of ELMs is also a great concern since ELMs are a product of high confinement regimes (H-Mode), presently the desirable operating regime for tokamaks. For the case of lithium exposure 5-10 cm from the strikepoint of a modest power H-mode with ELMs, it took only three ELM events to completely remove the lithium from the DiMES sample (Fig.12). Another clear sign that the ELMs remove macroscopic portions of the lithium is the strong lithium contamination of the core plasma as shown in the middle panel of Fig. 12. The heat flux and vertical current evolution as a function of time are also given.

The DiMES lithium exposure of February 2001 used a very low power, non-ELMing L-mode plasma in order to avoid the uncontrolled removal of the lithium from ELMs or disruption (Fig. 13). However, the liquid lithium was also removed by this benign divertor plasma.

The initial exposure of the sample to a sweeping divertor plasma resulted in some melting of the lithium with very little energy density deposited to the sample (Fig. 14-15). This melting is expected from the poor initial thermal contact between the lithium and sample, as seen in ex-situ tests of a foil sample at Sandia. Some macroscopic losses were seen in this case. However, three subsequent identical exposure discharges showed no signs of neither melting nor particulate removal, indicating that the initial melting had likely improved the thermal contact between the lithium and the graphite sample surface, and the sample remained solid.

Despite the small SOL currents found in L-mode, the lithium sample was also macroscopically removed by JxB forces. This occurred during a discharge with stationary plasma conditions, the strikepoint location was fixed ~3 cm inboard of the lithium (Fig. 16). A large release of lithium was observed, showing near-vertical injection of lithium towards the plasma core (Fig. 17). The constant heating provided by the plasma, q~ 0.3 MW m^{-2} eventually melted the lithium. Overheating of the lithium to highly evaporative temperatures (T > 1000K) is ruled out in this case for two reasons: 1) the absence of the development of lithium evaporation measured via atomic Li spectroscopy (Fig.18) and 2) thermography analysis that indicates a maximum surface temperature of < 700K (Fig. 19). Pictures of the exposed sample (Fig. 20) clearly show that the Li coating has been melted and removed from the Li-cup holder.

While still under investigation, the most likely cause of the lithium removal is summarized here. Imaging indicates that the lithium, presumably liquefied by this time, was forced up and outside of the cup diameter (Fig.21-22). Because this forced-out lithium now pushes up vertically into the plasma, it is forced to intercept parallel SOL current density. While this is much larger than current densities collected by a horizontal surface (i.e. $J_{plate} \sim J_{parallel} \sin\theta$; $\theta \sim 1\text{-}2\ °$), it does not directly lead to body forces since J is parallel to B. However, to complete the circuit the return path of this collected current is preferentially conducted back through the lithium sample, since lithium has ~100 times greater electrical conductance than the graphite of the sample holder. Thus a high-density radial current must flow from the forced-out lithium back to the main lithium sample and

then through the sample to the vessel. Using the measured direction of J in this case, the radial current leads to a vertically upward JxB body force on the lithium when the lithium is forced radially inward out of the cup. Indeed, the macroscopic removal occurs within ~10 ms of the initial inboard movement of the lithium. The estimated body-force acceleration (~1-5 $J_{parallel}$ x B ~ 100- 500 m s^{-2}) is sufficient to explain the measured vertical ejection of the lithium (Fig. 22).

In this case the JxB movement of the lithium is complicated by the non-uniformity of the surfaces. Indeed, the non-uniformity is one of the principal reasons for the movement of lithium. Therefore, we have undertaken a modeling effort in collaboration with UCLA to better characterize the JxB forces. Of particular interest is the role, if any, that the limiting cup plays. Nevertheless, the overall result of these experiments is that divertor MHD forces readily moved the liquid in both the radial and vertical direction.

Macroscopic lithium particulates penetrate to core plasma and disrupt the plasma

One of the outstanding features associated with the JxB removal of the lithium was the large influx of lithium to the core plasma. In the case of the ELMing exposures, the lithium caused temporary large increase in core plasma radiated power (Fig. 12). In the L-mode exposures, a sufficient amount of lithium entered the core plasma so as to cause a radiative disruption (Fig. 23). The amount of lithium entering the core plasma is ~ 10-50 mm^3 as inferred from core lithium spectroscopy and electron density increase. This is an appreciable fraction of the entire lithium sample with a volume of about 500 mm^3.

This result is understood from the physics of pellet ablation (Fig. 24). If one considers the particulate ejected by the JxB forces as a macroscopic particle (> 1 mm), with velocity ~ 10 m/s (as inferred from body forces and image sequences) then it is expected that the divertor plasma is not capable of stopping the particulate. The ablation of the dense cloud that forms around the pellet is very inefficient for electron energies below ~ 1 keV. Then

for the DiMES experiment, an upward traveling particulate moves through the divertor only to be ablated and deposited in the keV core plasma. This is in agreement with the pellet ablation theory and indicates that if the plasma core is not sufficiently hot and large (e.g. CDX-U and T-11M) the lithium projectile will pass through and not affecting much of the plasma. With the injected lithium from DiMES, this deposits sufficient lithium in the core plasma to cause a radiative collapse. This is easily understood when one considers that a 1 mm radius lithium pellet contains a number of lithium atoms comparable to the entire DIII-D plasma particle inventory. More detailed analysis of the pellet injection model is provided in the accompanying note by Evans.

Pellet ablation stands in stark contrast to the excellent shielding provided by the divertor for sputtered and evaporated lithium. *When lithium, or any material, is removed as macroscopic particulates, the divertor plasma is not capable of shielding the core plasma*. Clearly this is a serious concern for the viability of continuous liquid surfaces in divertor. This explains why the DiMES lithium sample, comprising < 0.1 % of the divertor surface, was capable of disrupting the DIII-D plasma. One can tolerate little or no JxB ejection of material in the form of macroscopic particulates. Also, the tolerable amount of particulate decreases with increasing atomic number (and hence radiation efficiency) of the candidate liquid. The fundamental question becomes the possibility of avoiding the JxB injection transport of liquid metal material into the hot plasma core.

Sandia National Laboratories provides DiMES Lithium samples

DiMES sample #106 with lithium metal insert – before exposure.

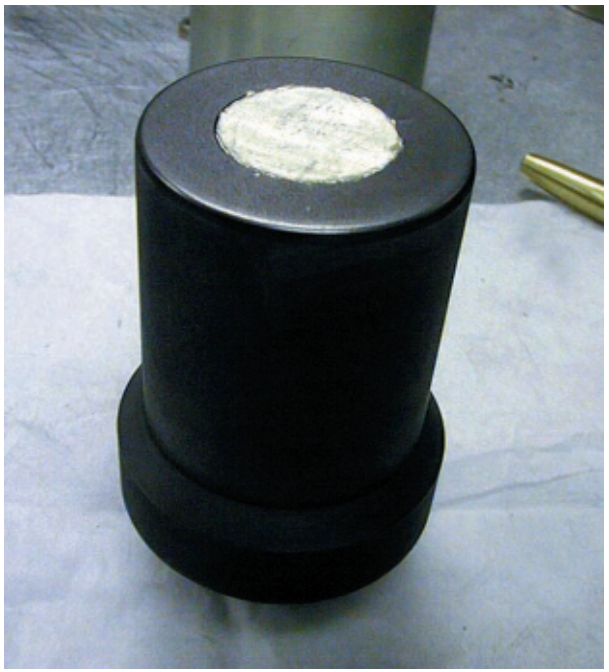

DiMES #106 is a graphite sample (ATJ) with a Li filled well (2.54 cm diameter, 1.3 mm deep).

RB:SNL:8724:2000-0628-02

Sandia National Laboratories

DiMES/ DIII-D provide an extensive array of plasma and PSI diagnosis

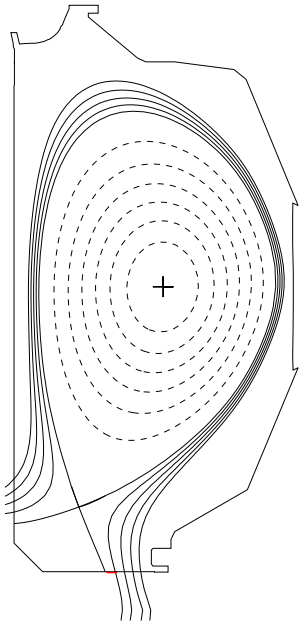

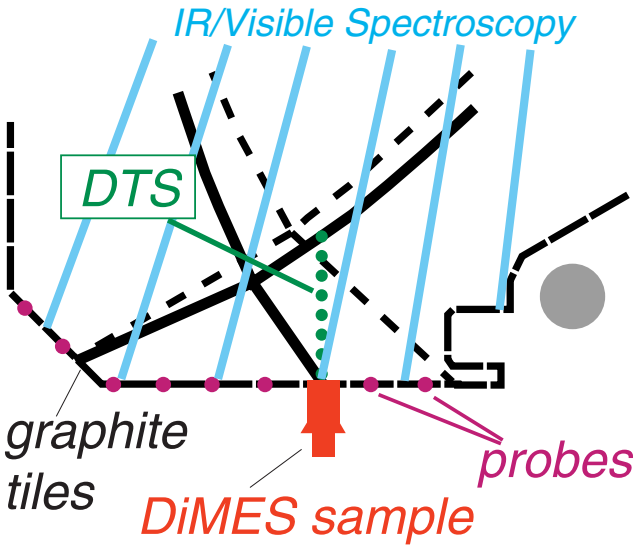

- Lower single-null plasmas used
- DiMES viewed by one visible spectrometer, three visible cameras equipped with Li filters and and IR camera.
- Solid lithium sample: O.D. 2.54 cm, thickness 1.3 mm, all-graphite backing.

Twin set of Tangential cameras and R+2 Camera Now Provide 3-D Images of Lithium Removal at DiMES

Tangential view

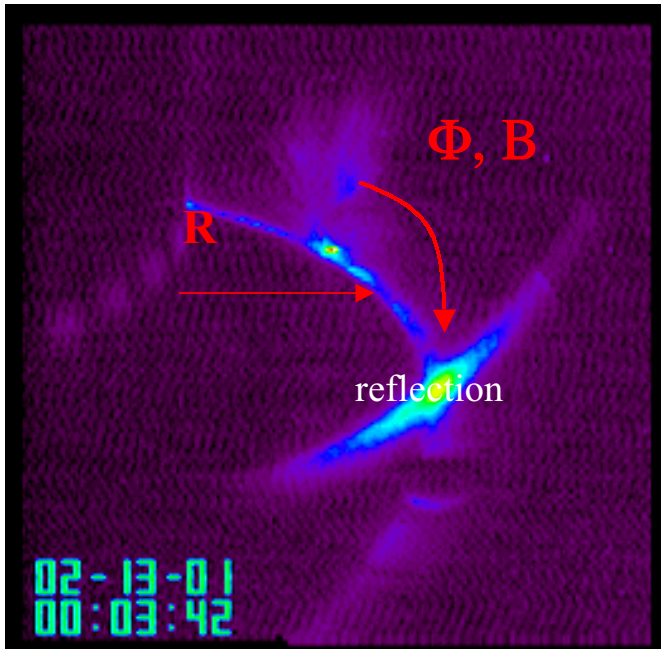

Top View (R+2)

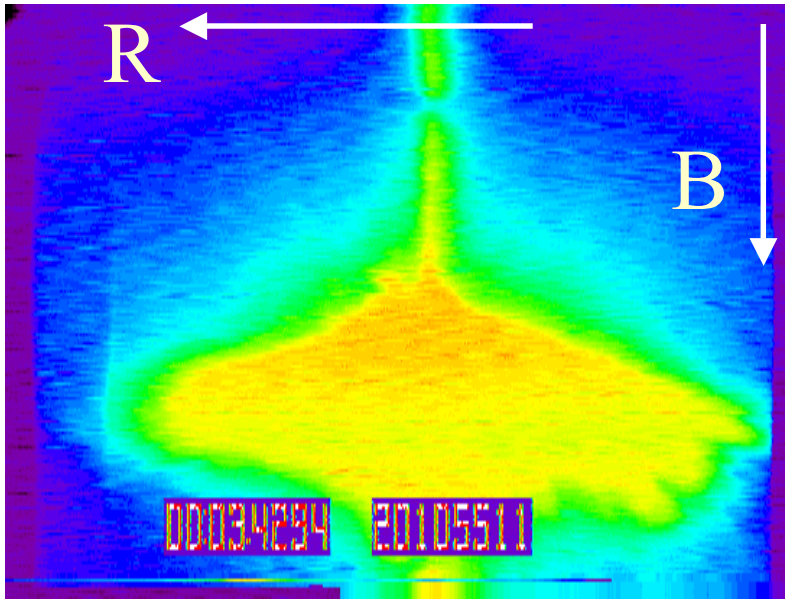

N.B. mirror image shown

High spectral resolution spectroscopy of lithium light provides fundamental data on the nature of lithium sputtering

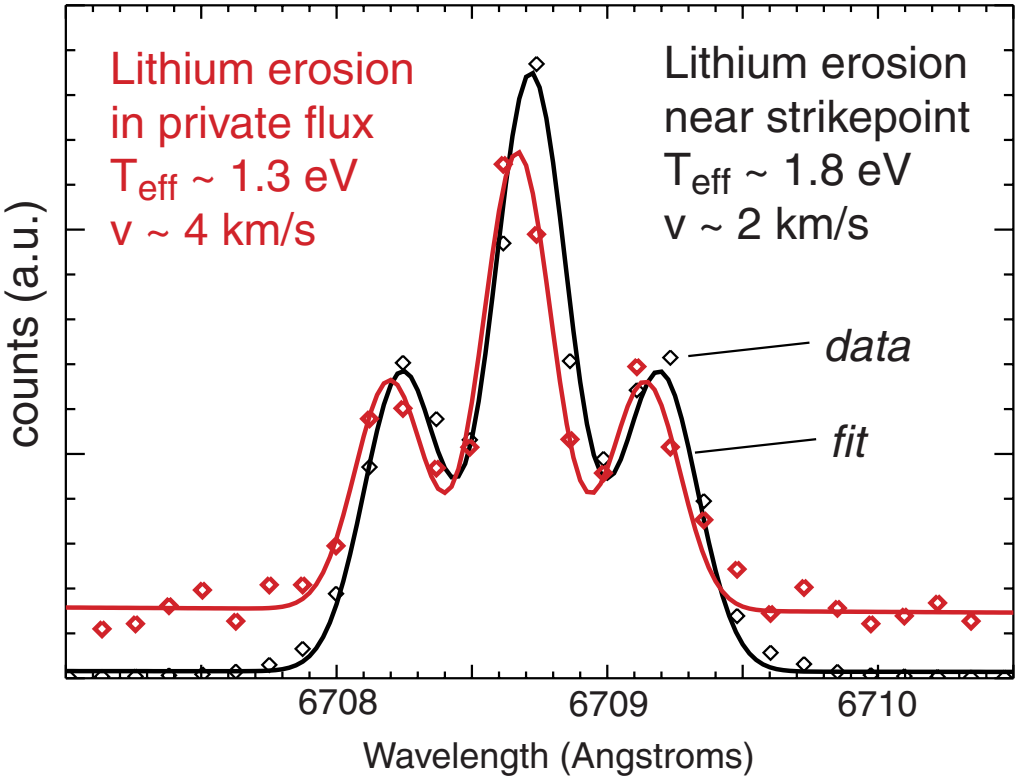

Spectrometer directly viewing DiMES
Solid lithium sample

- T_{eff} Ą velocity distribution of sputtered Li
- V Ą average directed velocity of Li away from surface
- Data is in approx. agreement with Lithium surface binding energy (E~1.6 eV) and expected ejection velocity (~5 km/s)
- Emissions from sputtered atomic lithium vary depending on location of lithium in divertor, indicating some changes in erosion mechanisms.

Plasma & Spectroscopy Diagnostic Provide High Resolution Divertor plasma and Li erosion

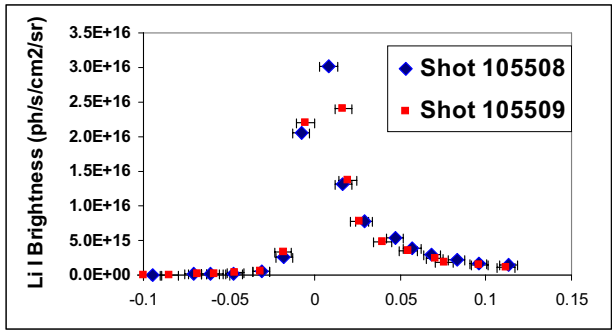

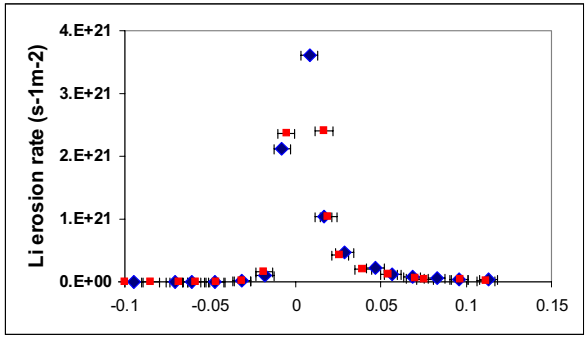

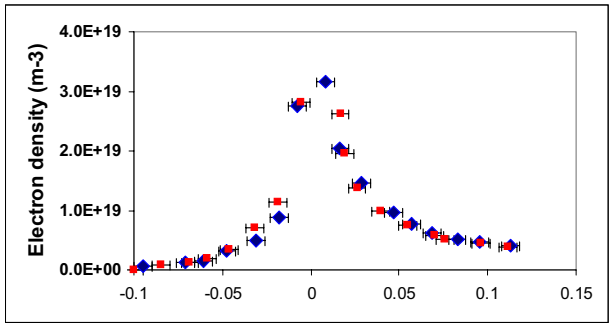

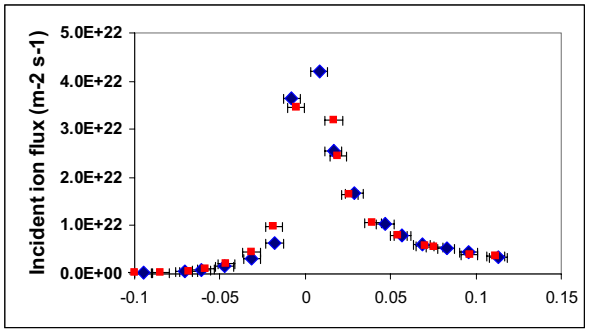

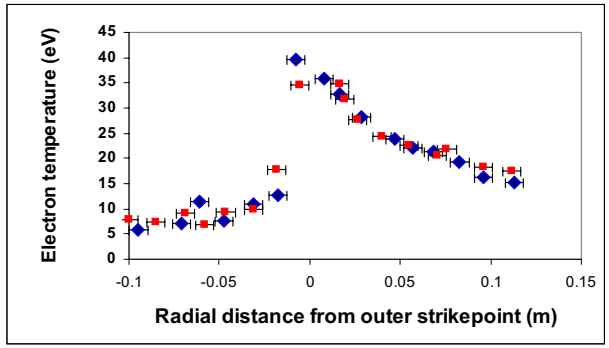

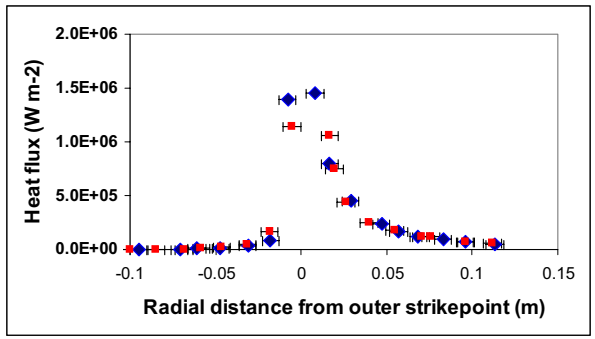

Excellent Shot-to-shot Reproduciblity

D.G. Whyte, ALPS report, July 2001

Fig. 5

Yield of solid Lithium from reproducible, "well-behaved" swept discharges agrees well with other yield measurements

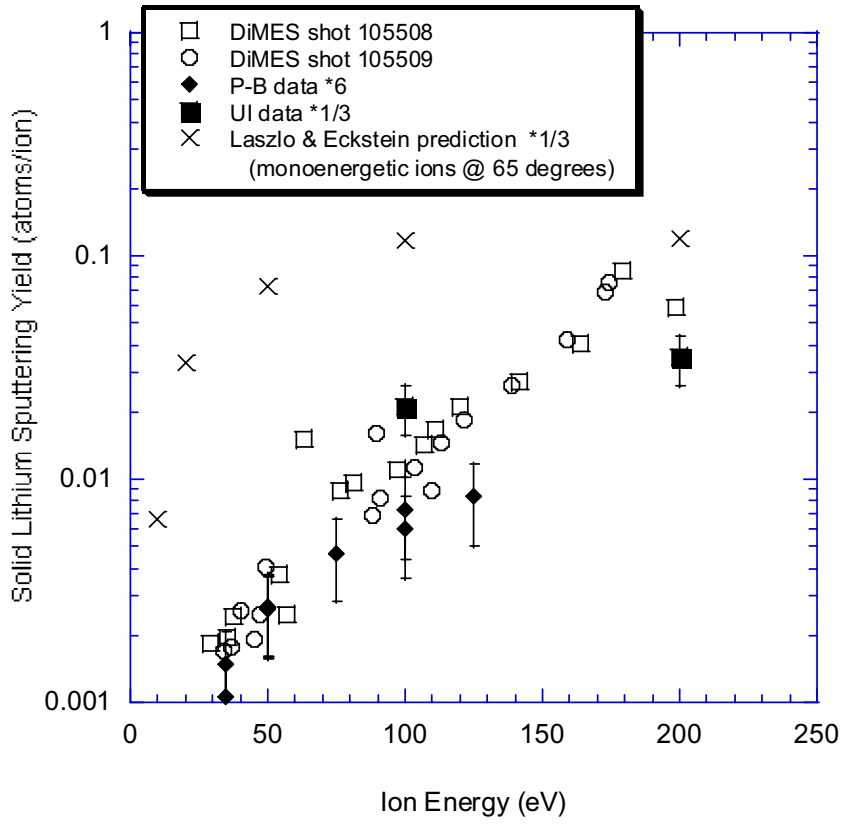

- **Yield measurement:**
  - **Incident flux from Langmuir probe**
  - **Li efflux from measured Li I brightness x $S/XB(n_e,T_e)$ for transition**
- **N.B. This is the same technique as developed on PISCES to measured Li erosion yield.**
- **Effective yield is < 10 %.**
- **Lab data corrected for ion sputtering (UI x 1/3) and angle of incidence (PISCES x 6).**

Imaging of Li I light during quiescent erosion of solid lithium indicates that lithium is ionized << 1cm from target

Tangential viewing geometry

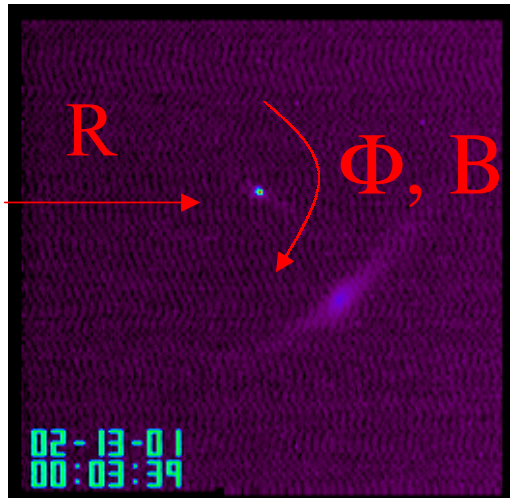

Vertical extent of Li I light Is smaller than camera resolution of few mm.

Top-Viewing Camera

Quiescent erosion

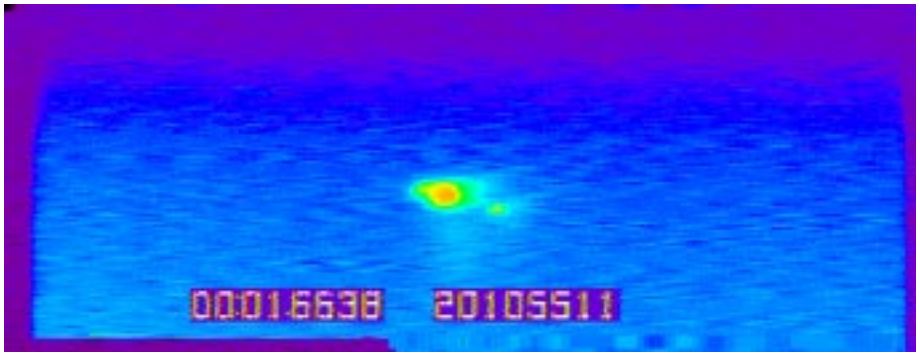

Li diameter: ~ 2.5 cm

Large currents are typically driven in the SOL of tokamak plasmas, giving rise to JxB forces at plasma-surface interfaces

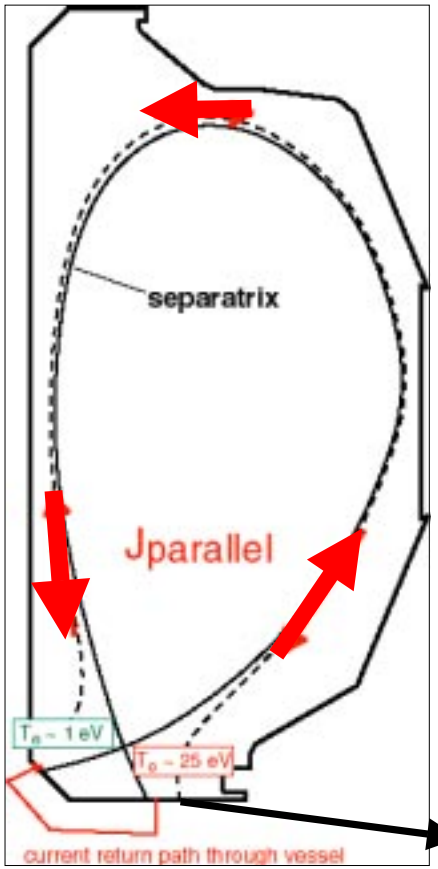

- Electric potential between cold inner and hot outer divertor drives $J_{parallel}$.
  - Electric field ~ 0.1 V/m, $J_{parallel}$ ~ 10^5 A/m^2
- Current path returns through the vessel, J_Z
- MHD events like ELMs enhance J_Z because they "dump" hot plasma into outer SOL.
- Note: JxB forces will *always* be present near strikepoint regions, even in absence of MHD events.

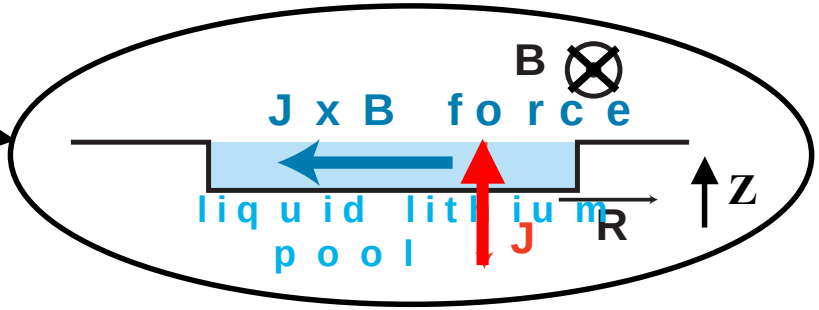

Fig. 8

Measured SOL currents can have spatial variation across divertor plasma. Large gradients found near separatrix.

Low-power L-mode case

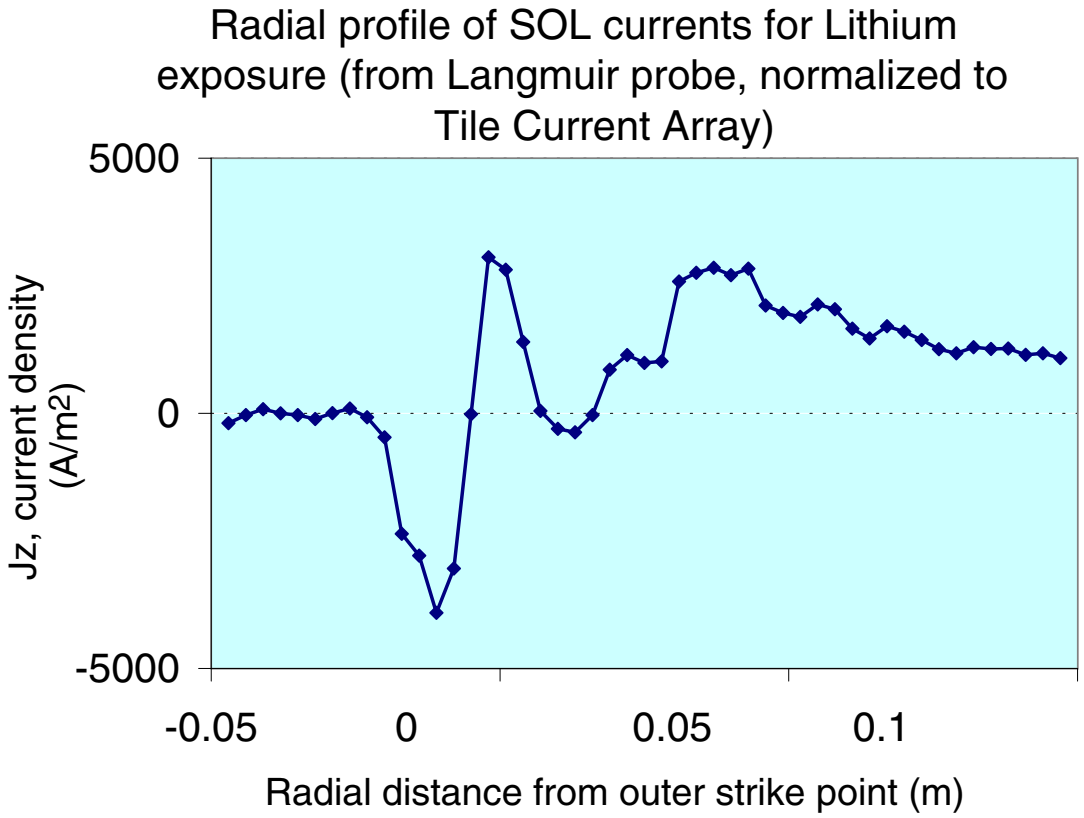

Positive J_Z denotes current vertically upward from divertor

JxB forces can lead to several movement scenarios for the liquid surfaces in the divertor.

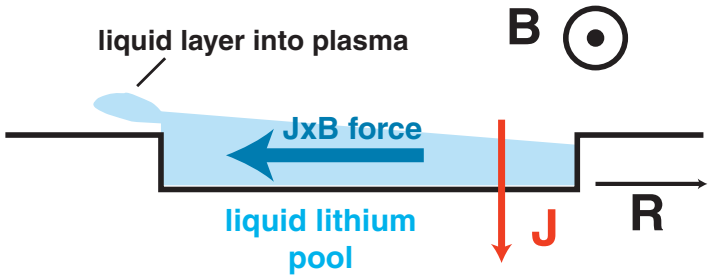

- Splashing out of the static pool.

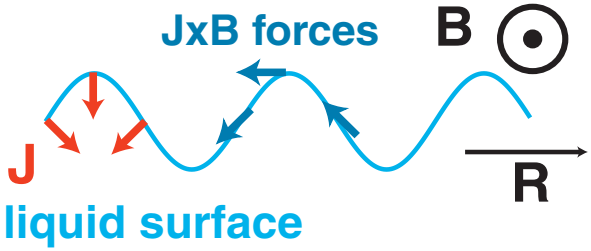

- JxB acts like a "shearing" force on surface perturbations.

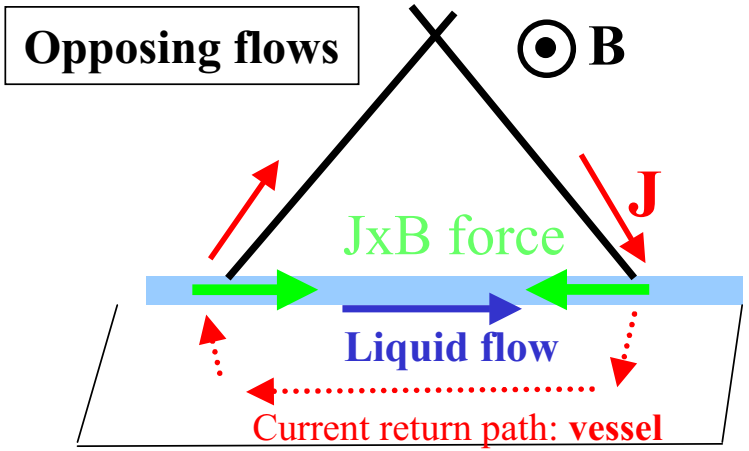

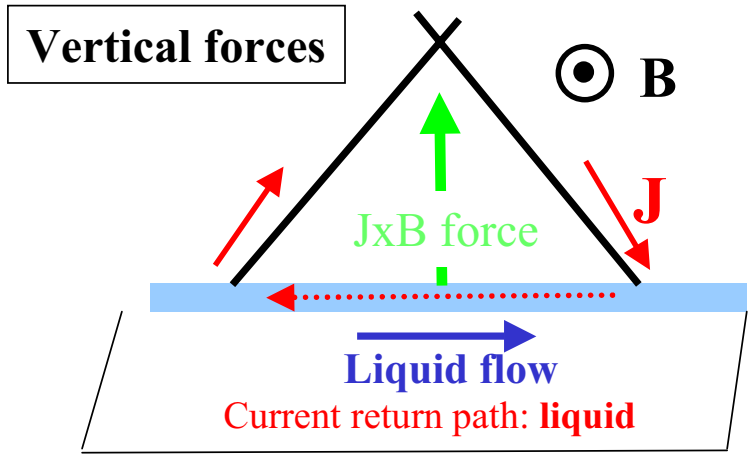

JxB movement of the liquified lithium during a locked-mode MHD event on DIII-D

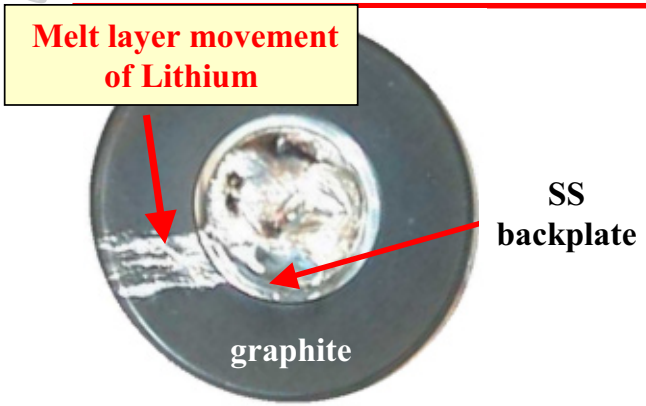

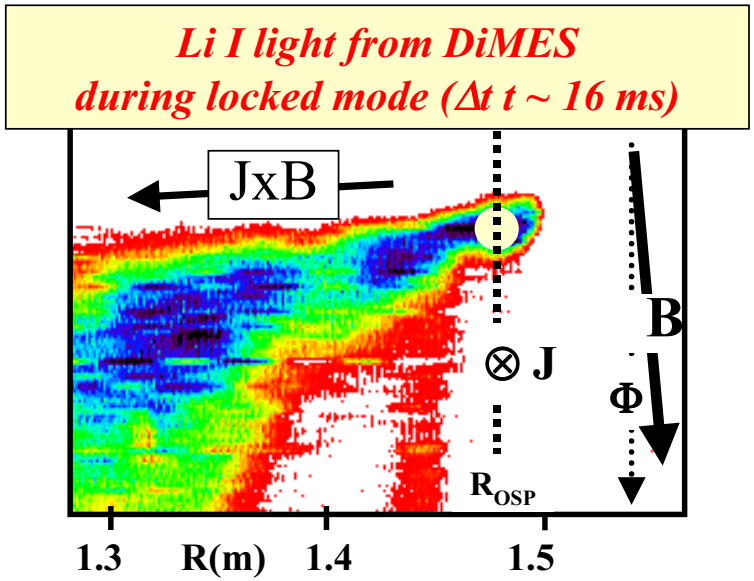

- Rapid loss of ~ half of core plasma's stored energy in ~70 ms during locked-mode
  - Outer strikepoint at DiMES, R_{OSP} = 1.48 m
  - q ~ 5 MW/m^2
- Thermal analysis indicates:
  - Entire lithium sample liquified at onset of locked-mode.
  - Maximum surface temperature ~ 300 °C.
- **JxB forces are cause of movement**
  - Coincident with peak measured current density into divertor wall (J_z ~10^4 A/m^2)
  - Correct orientation of movement.
- ***Consequences***
  - Removal of entire 0.25 mm lithium foil thickness on portions of sample!
  - Equivalent thickness of ~1 μm of lithium from DiMES sample found in core plasma.

D.G. Whyte, ALPS report, July 2001

Fig. 11

JxB removal of lithium caused by ELMs in H-mode

Li sample exposure on DIII-D

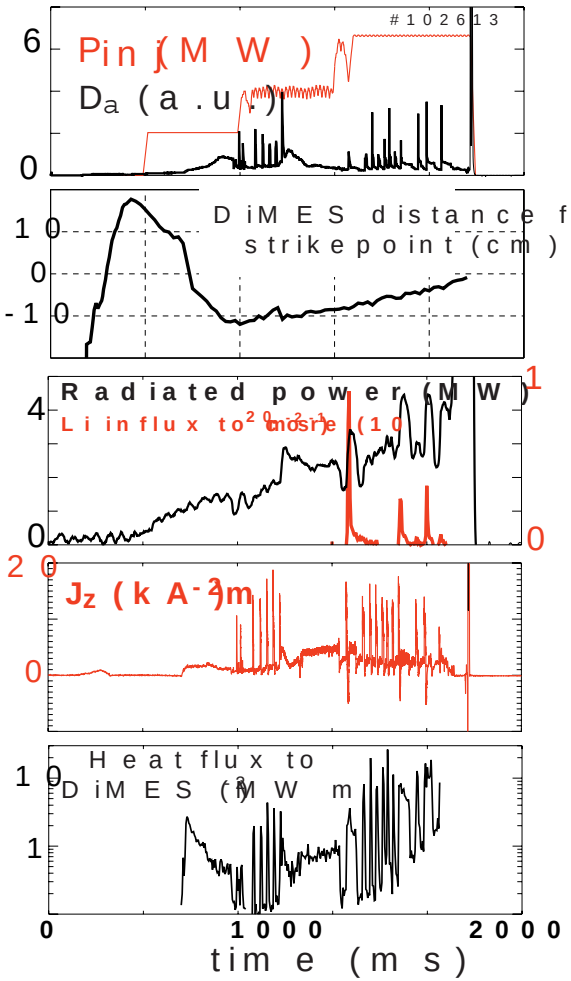

- **Medium power ELMy H-mode plasma.**
- **Strikepoint 5-10 cm from DiMES**
- **Modest quiescent heat flux ~1-2 MW m^{-2}.**
  - Thermal analysis indicates that the lithium melts near 1000 ms during exposure shot.
  - ELMs cause brief ten-fold increase in q to ~10 MW m^{-2} and further heat lithium
- **J_z associated with ELM causes JxB forces that remove ~0.1-0.2 mm layer of lithium per ELM**
  - 4-5 ELMs completely removed Li sample!
  - Large increase in radiated power from Li influx, consistent with ~0.1 mm removal of Li layer.
  - ~1-2% of lithium removed arrives in core plasma.
  - Li influx causes temporary reduction in confinement.
- **Lithium sample represents only 1/10,000 of wetted divertor area in DIII-D, yet macroscopic removal of lithium can nearly disrupt the plasma!**

D.G. Whyte, ALPS report, July 2001

Fig. 12

A lithium sample was exposed to very low power DIII-D divertor discharges

- Lower single-null plasma:
  - I_p = 1.1 MA, n_e = 2.5x10^{19} m^{-3}, B_T=2 T.
- L-mode confinement (i.e. no ELMs) maintained with very low heating power:

  P_{NBI} ~ 0.5 MW + P_{ohmic} ~ 0.7 MW = P_{in} ~ 1.2 MW.
- DiMES viewed by one spectrometer, three visible cameras and IR camera.
- Solid lithium sample: O.D. 2.54 cm, thickness 1.3 mm, all-graphite backing.

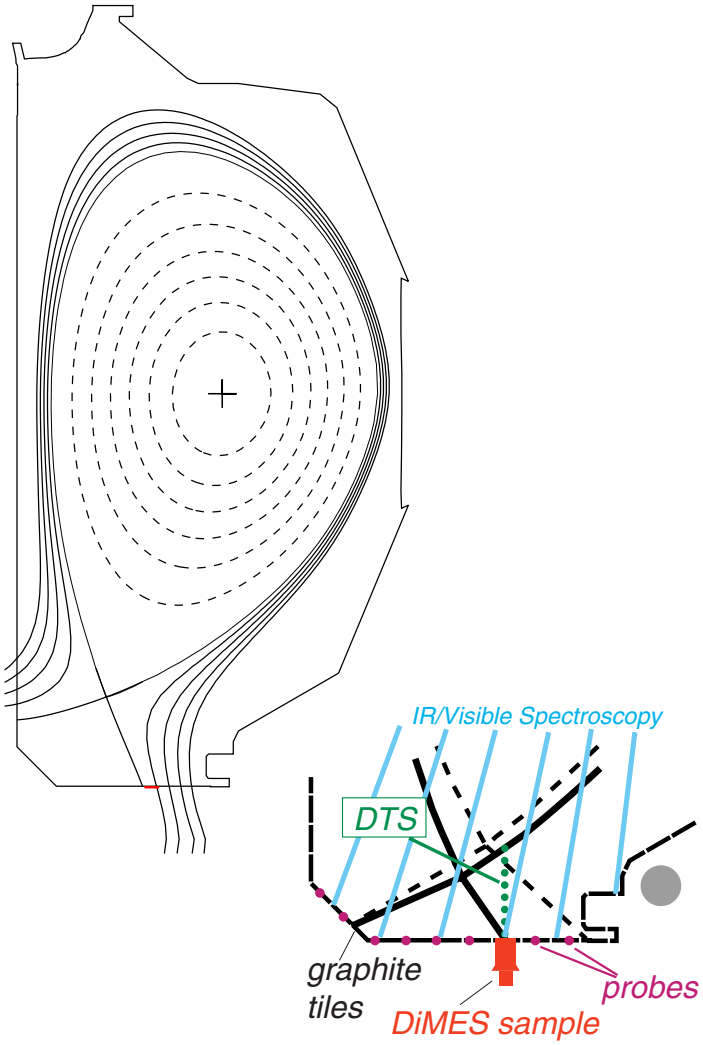

(This is nearly the lowest power discharge available in DIII-D)

The first four L-mode exposures swept the OSP past the Li sample

- First exposure discharge (105506):
  - Side-viewing camera showed significant “bursts” of lithium removal when the OSP was moved near (see next slide).
  - Subsequent exposure was more quiescent.
  - The lithium bursts had little or no effect on the core plasma.
  - Visual inspection of the sample showed a reflective surface, indicating the lithium had melted.
  - Vertical thermo-electric currents ~ .1 A/cm^2 measured near OSP, going out of plate.
- Next three exposures (105507-09)
  - No large influx of lithium.
  - Reproducible shot-to-shot for lithium removal
  - Effective yield near separatrix ~ 10%.

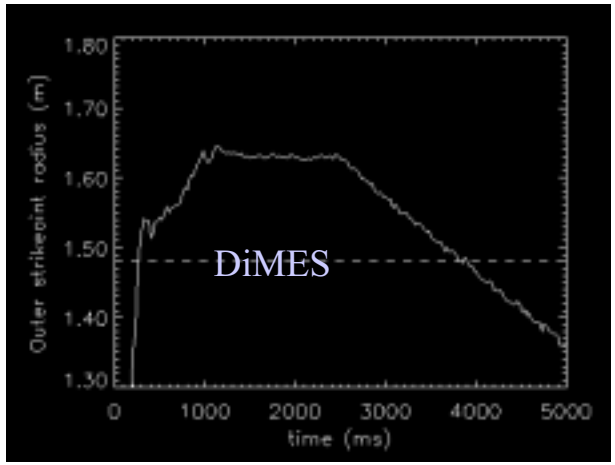

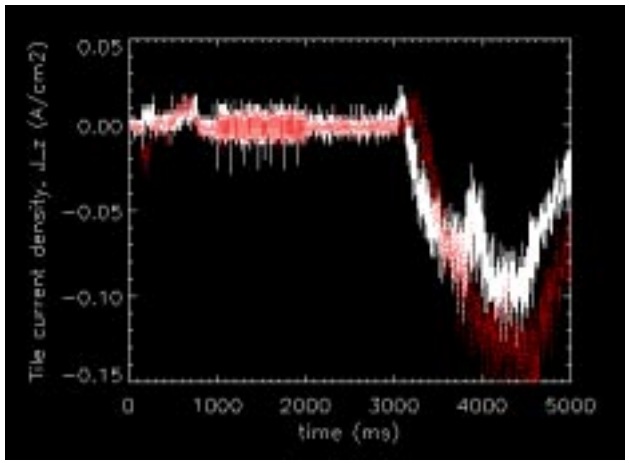

White: f=135°, Red: f=310°
f_{DiMES}=150°

The very first OSP exposure of the lithium resulted in some partial melting and limited MHD removal of Li

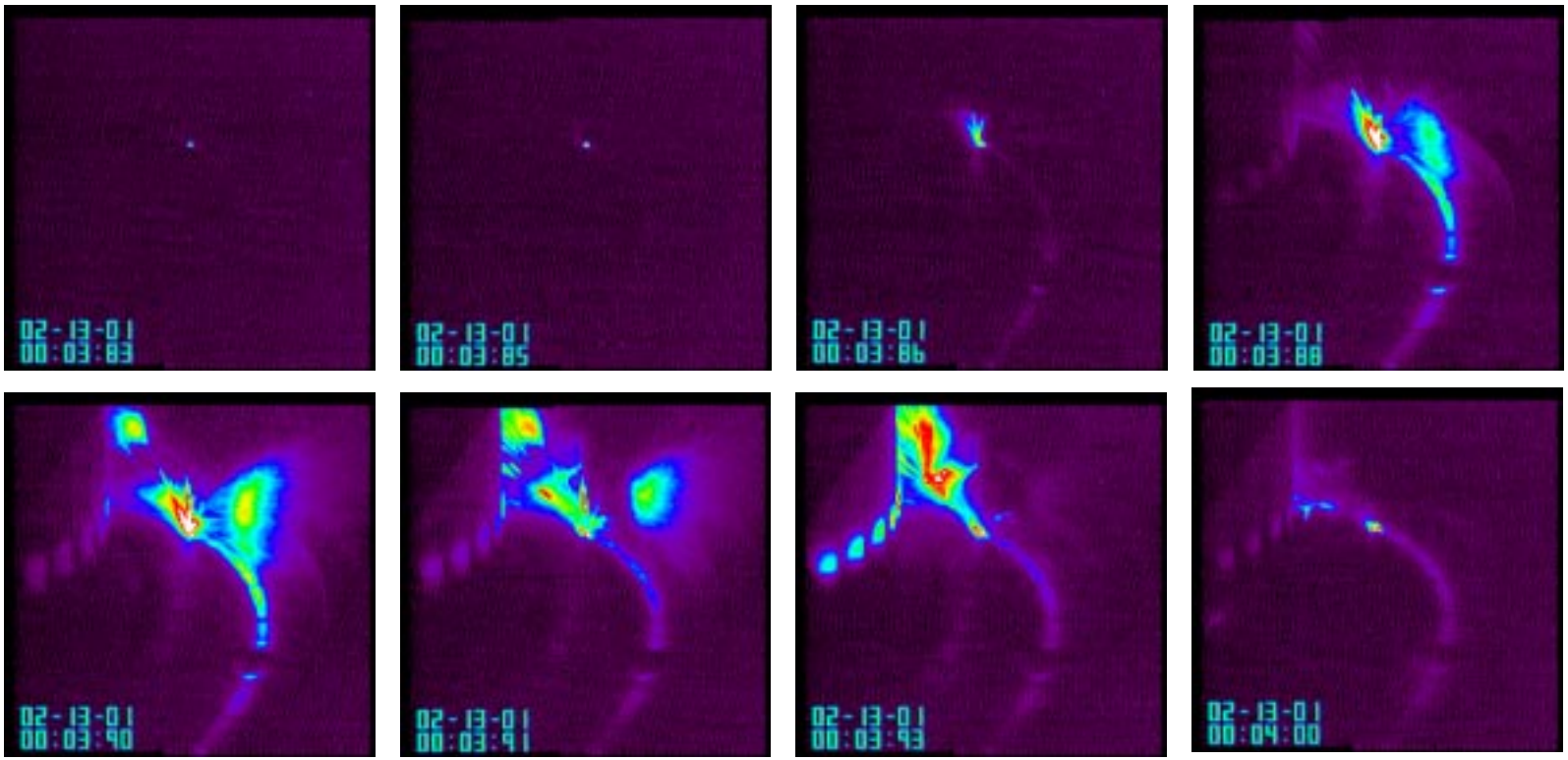

R

Φ, B

J_Z

Li I light

(670 nm)

Two discharges fixed the strikepoint position during the shot

- **Shot 105510:**
  - OSP ~ 5 cm inboard of DiMES for t >1000 ms.
  - T_e ~ 20 eV, q ~ 0.15 MW/m^2
  - Steady erosion throughout the shot, at a level consistent with the swept discharges.

- **Shot 105511**
  - OSP ~ 3 cm inboard of DiMES
  - T_e ~ 30 eV, q ~ 0.3 MW/m^2
  - Increasing lithium removal rate t>3000 ms.
  - Radiative disruption occurs at 3478 ms.

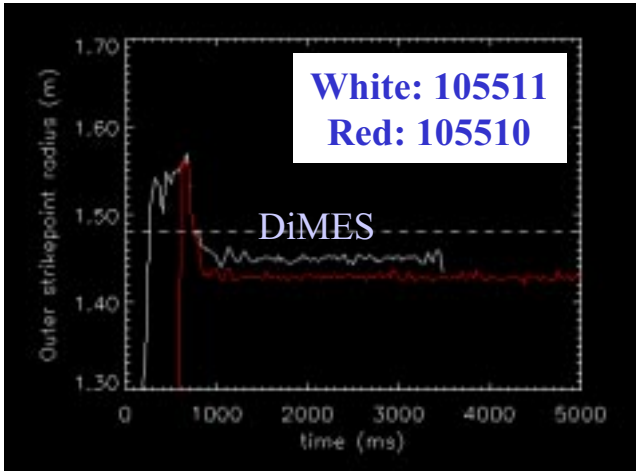

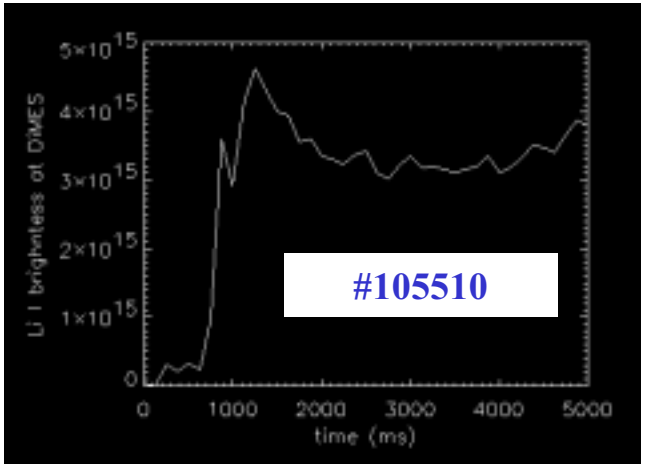

Video sequence of Li I light in divertor , following the large release of Li that causes the disruption (105511)

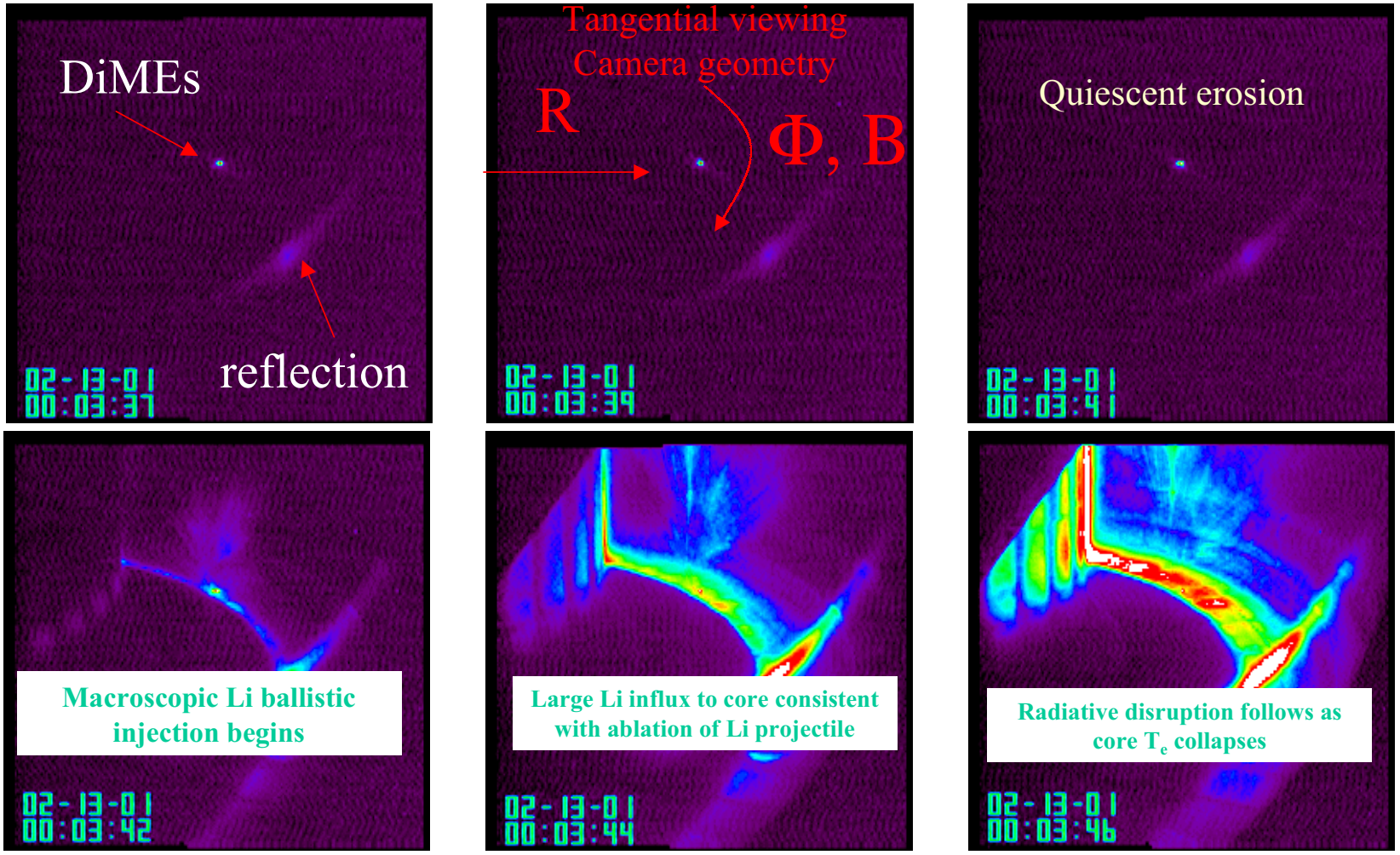

Visible atomic Li spectroscopy verifies that the surface temperature could not have greatly exceeded 700K during discharge due to absence of evaporation.

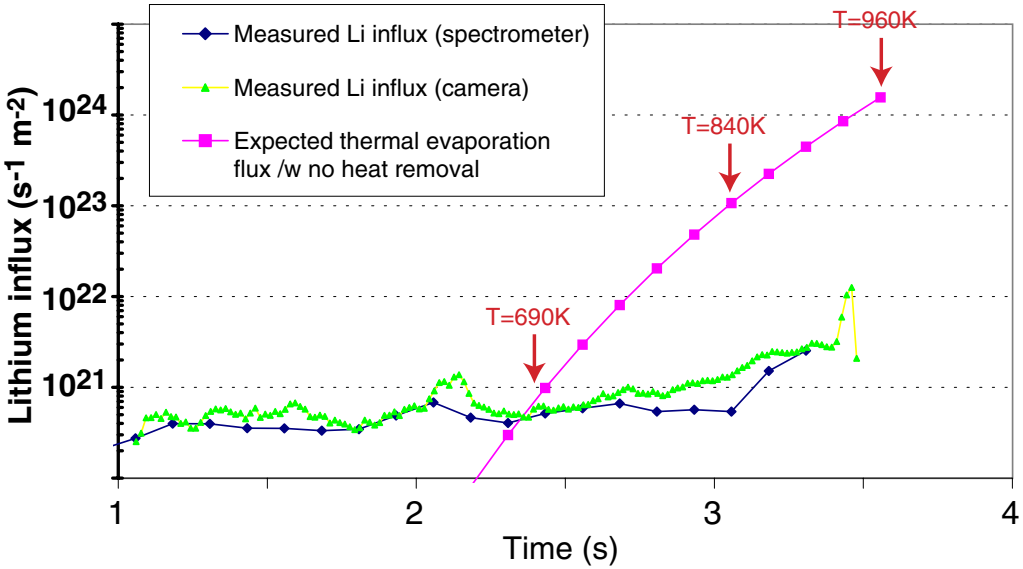

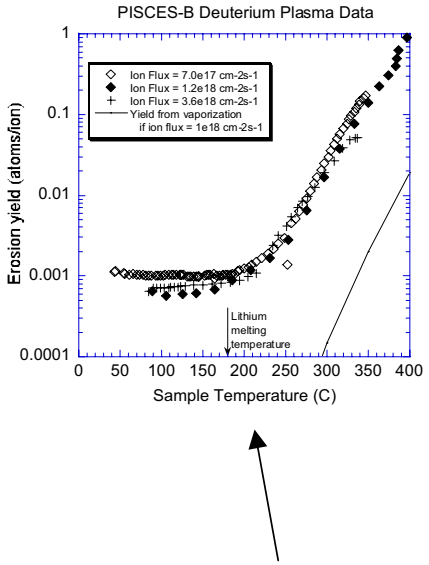

- Above 700K the lithium evaporation itself is the most accurate means of measuring T_{Li}…yet this evaporation is clearly not present up to the point of the "ballistic" injection event.
- The injection event occurred instantly (<20 ms): seems to rule out over-heating as the cause.
- With no thermal contact the sample should heat up to ~1000 K in ~2.5 seconds (SNL result)
  - We should explore reason why our sample seemed to have better thermal contact.

IR Thermography Analysis Indicates that the Lithium Surface Temperature Does Not Go Above 700-800 K. Visual clues from Li imaging suggest that lithium melts somewhere around 2.5-3 seconds into discharge.

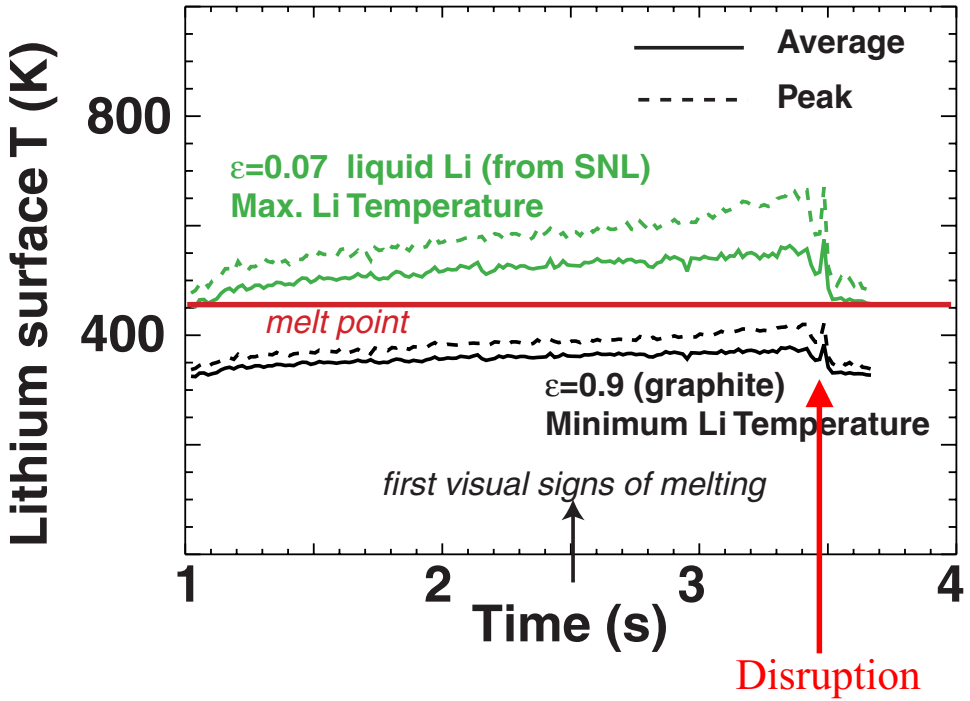

- "Corrected temperature" of Li based on:
  - SNL provided ε_{Li}~0.07
  - Solving equality of non-linear Planck's law in IR wavelength region for different emissivity materials.
- Most likely ε and T is in-between these two extremes.
  - Initial temperature should be ~300K.
  - For ultra-pure lithium ε_{Li}~0.04 Ą T_{max}~800K.

Li sample after exposure to of a low power L-mode discharges

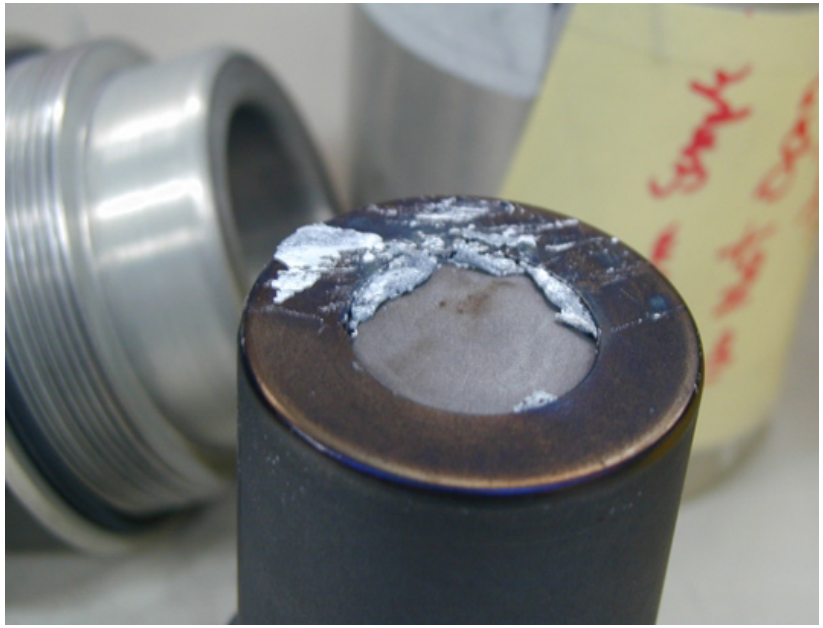

- $q \sim 0.3 MW/m^2$
- Li has clearly melted and been displaced
- Unclear on relative amount lost through initial JxB event and final Li caused radiative disruption.

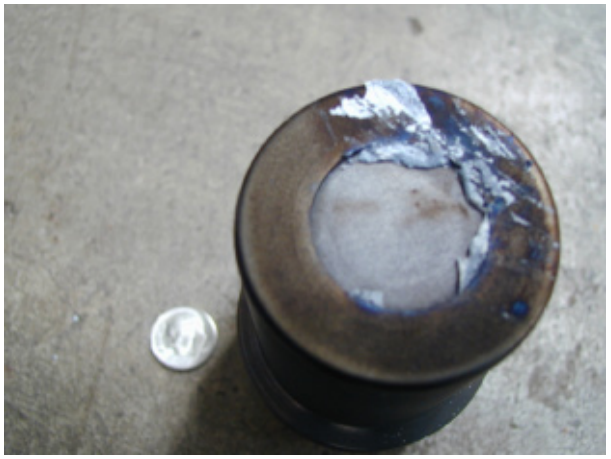

Camera Li I Images Show that the Liquefied Lithium moves on the DiMES sample

- Exposure for discharge that ends in lithium radiative disruption:
  Ŵєє ~ 0.3 MW m^{-2}
  3 cm outboard of OSP

- Radial outward movement of the lithium seen here is consistent with measured J_z x B direction in steady-state portion of discharge after liquefaction.

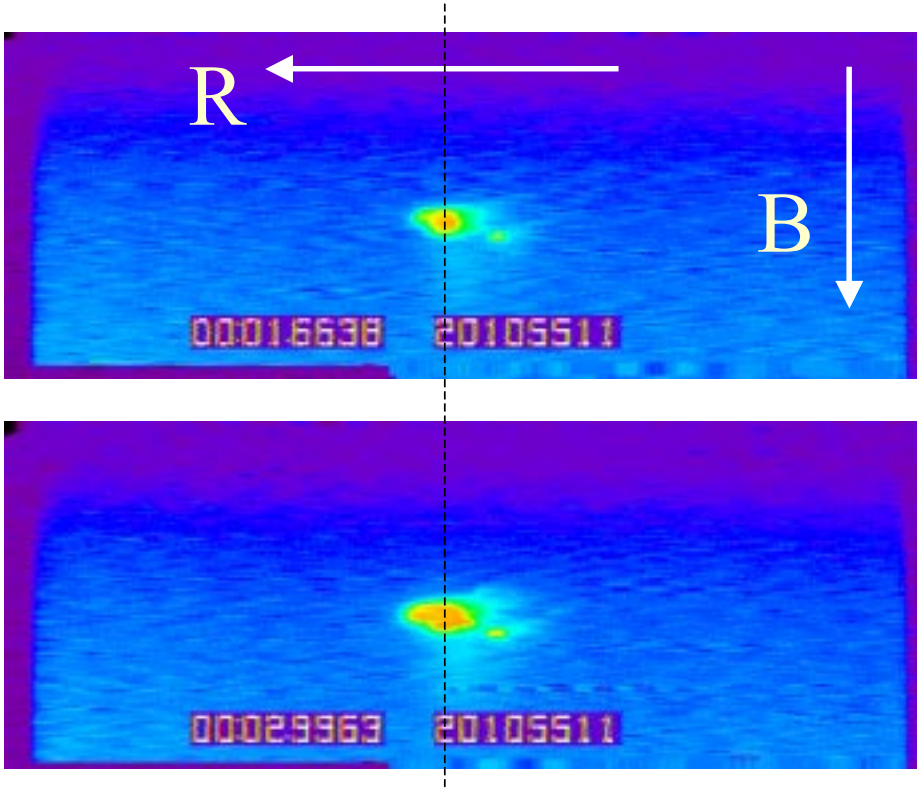

Note: mirror image shown

Vertical upward J_rxB force is most likely cause of large lithium removal.

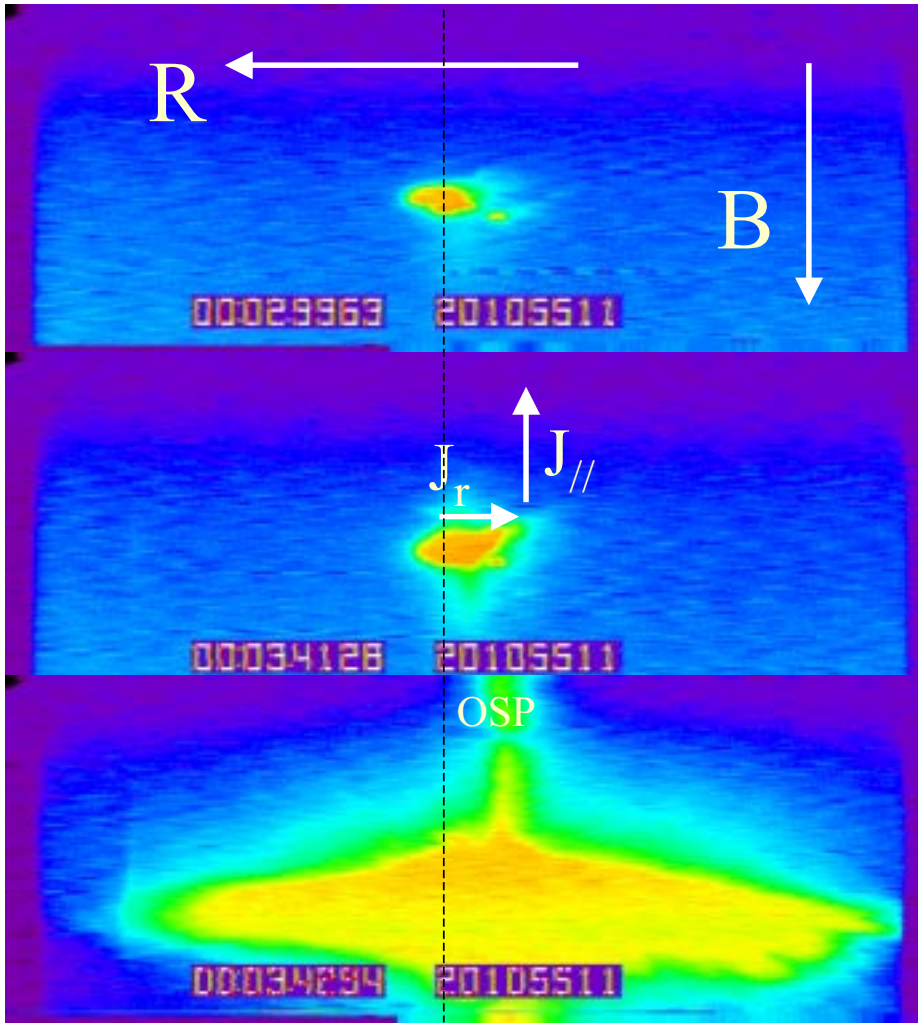

Note: mirror image shown

- Just before removal, the lithium moves radially inward inside of the DiMES cup.
- The large parallel current intercepted by this blob will cause J_r back through DiMES sample.
- Center of lithium release is actually inboard of original DiMES lithium location in cup.
- Estimate of vertical JxB/ρ acceleration seems large enough to cause removal
  - $J_{parallel}$ ~ 35 kA m^{-2}
  - B = 2.1 T
  - a~ $(JxB)\rho^{-1} A_{face}/A_{conduct}$ ~ 150-600 m s^{-2}

The disruption is caused by a radiative limit due to an enormous influx of Li to the core plasma

- Lithium completely dominates all other lines on core XUV spectrometer.
  - S/XB technique give 0.2-1x10^{23} lithium ionizations / s into core.
- Core plasma density doubles in ~ 30 ms coincident with core Li emission
  - Implies Li influx / ionization rate ~ 10^{22} s^{-1} in core plasma.
- Radiative power becomes much larger than input power leading to a radiative collapse
  - Estimate of Li caused radiated power matches well with bolometer.

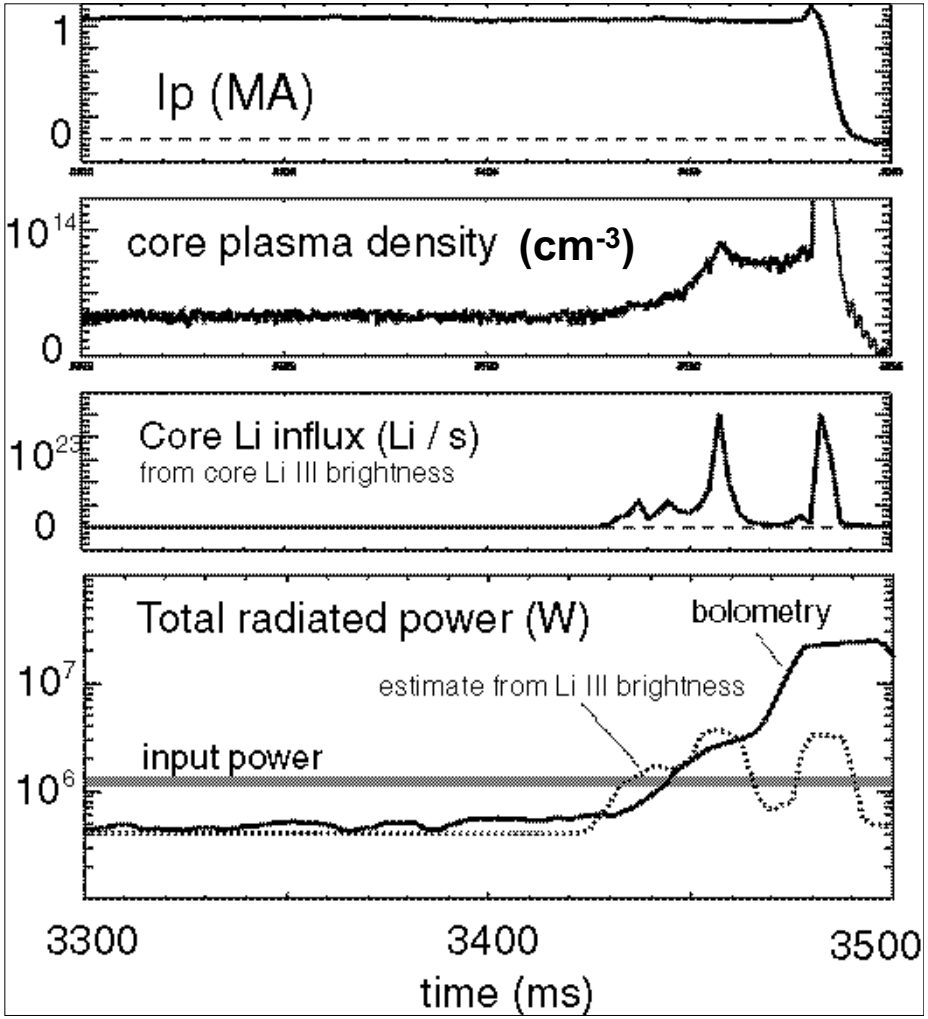

Fig. 23

Unlike sputtered or evaporated lithium, projectiles ~ 1mm radius with ~ 10 m/s will easily pass through the low temperature divertor and enter the core plasma to cause radiative collapse.

Video sequence shows that lithium projectile travel vertically at ~20 m/s andpasses through divertor to core plasma

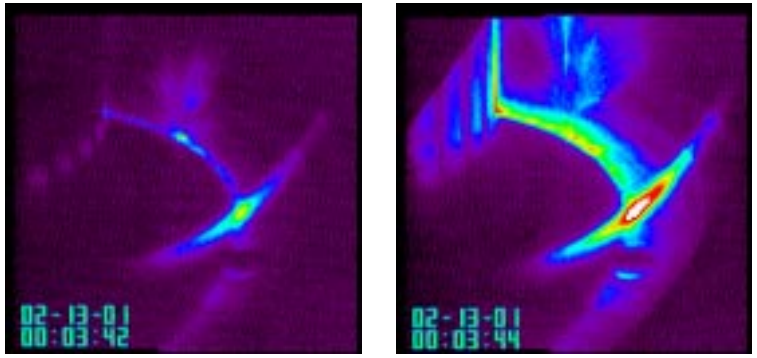

Pellet ablation theory shows that only the hot core plasma can stop the projectile

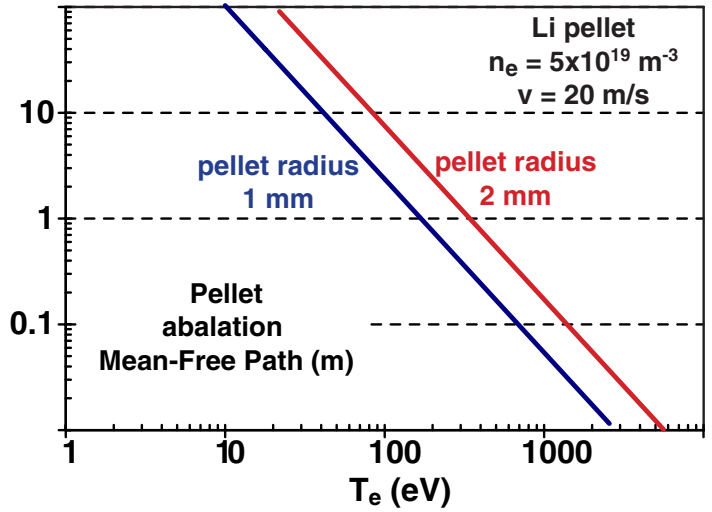

Ablation MFP $\propto v_{pellet}\, r_{pe;;et}^{5/3}\, T_e^{-5/3}\, n_e^{-1/3}$

Note: if core plasma is not sufficiently hot and large (e.g. CDX-U, T11-M) the projectile will pass through and not greatly affect plasma.

The Analysis of a DIII-D Disruption Sequence Induced by a Small Lithium Sample Subjected to a Low Power L-mode Plasma

T. E. Evans[1], D. G. Whyte[2], C. P. C. Wong[1], and W. P. West[1]

[1]General Atomics
[2]University of California, San Diego

Abstract

Based on a unique set of data obtained during a lithium sample exposure in a well-diagnosed DIII-D discharge we have found that relatively low levels of heat flux, due to a low power L-mode plasma, are sufficient to melt a small lithium sample. Once the sample melts, it appears that the currents flowing in the SOL cause it to deform and intercept significantly more parallel current, which then initiates a series of events that result in a disruption of the plasma. The most plausible scenario for the onset of the disruption sequence is the ballistic ejection of a 10-40 mg liquid blob traveling approximately 30 m/s from the vicinity of the sample. The ejected blob enters the core plasma and causes a radiative collapse that contracts the current profile and induces a locked mode. The locked mode reduces the core confinement and triggers a vertical displacement event (VDE) type disruption event which dumps the remainder of the core kinetic energy, that is not radiated away by the lithium in the outer core region, into the lower divertor. Finally, the current quench phase of the disruption converts the energy in the poloidal field into kinetic energy and dumps a fraction of this into the divertor.

Experimental Background

A DIII-D DiMES probe [1] was designed to accommodate a small 2.54 cm diameter lithium sample contained within a 1.3 mm deep graphite holder (i.e., approximately 350 mg of lithium). The lithium sample consisted of multiple layers of a thin, high purity, lithium foil pressed into the graphite holder. A sequence of four plasma discharges were run in which the outer strike point of a low power, lower single null, L-mode discharge was swept slowly across the lithium sample in order to assess the sputtering and transport properties of lithium in the plasmas with stationary plasma parameters and to calibrate the diagnostics systems. Previous experiments in ELMing H-mode plasmas were difficult to analyze because of the repetitive nature of the high heat flux introduced during the ELMs and the complete removal of the lithium layer due to $\mathbf{j} \times \mathbf{B}$ effects. Thus, these L-mode experiments were done with relatively low divertor power flux ($\leq$ 300 kW/m^2) to better accommodate studies of the basic plasma-surface interaction and transport properties of solid and liquid lithium surfaces. The goal was to heat the lithium sample slowly then study its sputtering and transport properties as a function of the sample's temperature. In particular, we wanted to get detailed information about the lithium plasma-surface interaction and transport properties near and just above the solid to liquid phase transition boundary.

After completing four swept outer strike point discharges, the plasma was positioned with the outer strike point fixed approximately 5 cm inside (R_{strike_out} = 1.43 m) the center of the lithium sample (R_{Li_center} = 1.48 m) and a stationary L-mode discharge was run. This plasma ran normally without any significant changes in the lithium sample and without any increase in the divertor or core plasma Li line radiation. On the next shot in this series (shot number 105511) the outer strike point position was moved outward to about 3 cm from the center of the lithium sample. Prior to shot 105511 only the first swept strike point case showed any signs of melting or increased Li radiation. It is possible that during the first swept shot the individual layers of lithium foil may have briefly melted and emitted a small burst of lithium, which was detected spectroscopically. If this is the case, then the sample would have re-solidified after the first swept shot and could have established much better thermal and electrical contact with the graphite holder. All of the shots in this experimental sequence were run with a toroidal magnetic field of 2.05 T, a plasma current (Ip) of 1.2 MA, an Ohmic heating power of 1.1 MW, a neutral beam heating power of 2.6 MW and an elongation of 1.7. Additional experimental details are outlined in a companion summary (see by D. Whyte et. al.)

Shot 105511 was the final discharge in the experimental series. During this shot the sample apparently melted and released a substantial influx of lithium into the core plasma were it initiated a radiative collapse of the edge followed by a locked mode and a disruption. Details of the magnetic equilibrium relative to the position of the DiMES probe are show in fig. 1 below at 3425 ms approximately 2400 ms after the beginning of the Ip plateau.

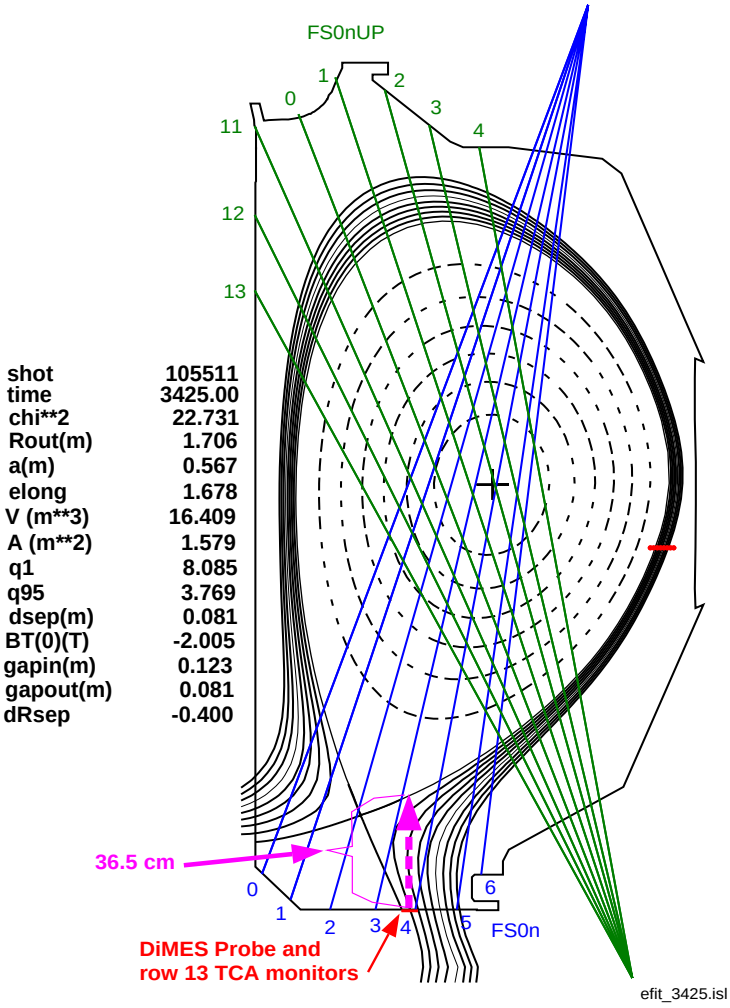

Fig. 1 - The plasma shape and position for shot 105511 at 3425.0 ms.

At this time in the discharge the outer strike point is positioned about 3 cm inside the center of the lithium sample and within 4 cm of the inner edge of the row 13 Tile Current Array (TCA) monitors. This effectively put the lithium sample within a few e-folding lengths of the peak in the poloidal heat flux. Note that the vertical distance from the surface of the DiMES probe to the separatrix is 36.5 cm at this time. The average electron temperature along this vertical path in the divertor is approximately 20-30 eV and the average electron density is of order 2×10^{13} cm^{-3}.

Summary of Experimental Data

The row 13 TCA monitors shown in fig. 1 are comprised of 3 individual detectors centered at a major radius R = 1.48 m (the same radius as the center of the DiMES probe) but separated toroidally to measure the toroidal distribution of the SOL current flowing

parallel to the magnetic field. The row 13 TCA monitors are located at toroidal angles $\varphi = 45^{o}$, 135^{o}, 310^{o}. These monitors spatially integrate the current flowing in the SOL and private flux region over a 13 cm wide radial extent. Parallel currents in the SOL can be generated by electron temperature difference at the ends of the flux tubes connecting the inner and outer divertor target plates in lower single null plasmas such as shot 105511. Typically, T_e at the outer strike point is higher than that of the inner strike point causing a thermoelectric current ($\mathbf{j}_{th}$) to flow out of the low field side target plates (i.e., the row 13 tiles in fig. 1), over the top of the plasma, and into the high field side target plates. The circuit is completed through the vacuum vessel toroidally and poloidally. For the configuration shown in fig. 1 $\mathbf{j}_{th}$ typically flows out of the target plates centered on the DiMES probe radius and into the center post target plates just above the 45^{o} tile on the high field side. In this case, we use the convention that $\mathbf{j}_{th}$ is positive.

During the Ip plateau of shot 105511 each of the row 13 TCA monitors register a relatively steady net negative current (positive $\mathbf{j}_{th}$) of between 10-15 A/tile until about 3416 ms into the shot. Under some conditions the TCA monitors register currents of up to 150 A/tile during ELMs and in excess of 1 kA/tile during disruptions. While these currents flow parallel to the magnetic field in the plasma, inside the solid graphite targets just below the plasma-surface interface they flow normal to the surface and thus have a component perpendicular to the magnetic field in the solid material. This perpendicular $\mathbf{j}_{th}$ component produces a force on the solid material, which attempts to move it radially outward. Due to differences in the radial T_e profile along the target plate surface from the inner to outer strike points, $\mathbf{j}_{th}$ can also have a radial profile across a tile. Under some conditions $\mathbf{j}_{th}$ could be positive over part of a tile and negative over the remainder of the tile. This possibility has been suggested by divertor Langmuir probe measurements made during strike point sweeps of the plasma but needs additional quantification. Each of the TCA monitors integrates the $\mathbf{j}_{th}$ profile over a 13 cm wide region so changes in the direction of $\mathbf{j}_{th}$ over a single monitor would reduce the magnitude of the measured total current flowing into or out of the tile. In order to understand the dynamics of a solid or liquid sample placed in the DiMES probe, it is necessary to know the radial profile of $\mathbf{j}_{th}$ and the geometry of the sample (which in the case of a liquid can change as a function of time due to the applied $\mathbf{j}_{th} \times \mathbf{B}$ force).

In fig. 2 we show the signals from the three row 13 TCA monitors during the final 85 ms of shot 105511 (upper frame) and the evolution of the plasma current during this time in the shot (lower frame).

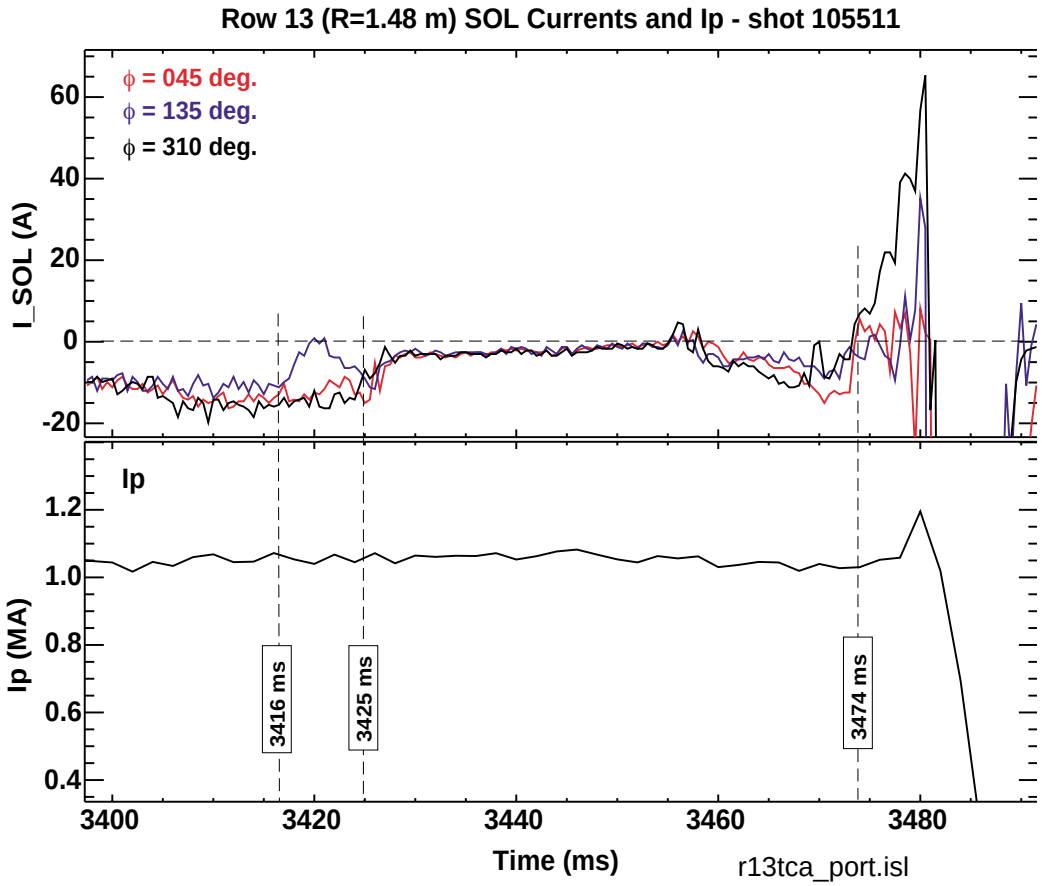

Fig. 2 - Upper frame: Tile Current Array monitor signals in the row 13 tiles during the termination phase of shot 105511, Lower frame: Plasma current during the final 85 ms of shot 105511.

Note that during the onset of the current termination sequence, 3474 ms < t < 3480 ms, the SOL current develops a relatively large negative non-axis-symmetric halo-like current component which may be due in part to an increase in a negative $\mathbf{j}_{th}$ component (i.e., into the tile) during a vertical displacement event and the subsequent thermal quench. Following the thermal quench, Ip begins to drop in the core at approximately the L/R decay rate of a 100 eV plasma and a large positive halo current forms (cutoff in the upper frame of fig. 2 in order to emphasize the behavior of the SOL current earlier in the shot). These Ip quench induced halo currents are not driven by the thermoelectric effect but by the collapse of the poloidal magnetic flux and can reach peak values ranging from 25-45% of the plasma current when integrated toroidally and poloidally.

Based on our best understanding of the data available leading up to the disruption shown in fig. 2, we suspect that the integrated heat flux to the lithium sample exceeded that needed to convert all or part of the sample to a liquid. The data suggests that the solid-to-liquid transition most likely occurred just prior to the dip in the $\varphi = 135^{o}$ TCA monitor

current starting at 3416 ms in fig. 2 (upper). The $\varphi = 135^{o}$ TCA monitor is located 15^{o}, or ~39 cm, upstream along the magnetic field from the lithium sample in the DiMES probe. At $\varphi = 135^{o}$ the field line that connects to the lithium sample it about 2 cm above the surface of the TCA monitor. A cloud of singly ionized lithium ions traveling at $v_{li} = 8.6 \times 10^{3}$ cm/s due to the background plasma ion thermal gradient force would pass over the $\varphi = 135^{o}$ TCA at approximately 3420 ms if it were released from the sample at 3416 ms. Simulations of the thermalization of low charge states of carbon impurity ions sputtered from the DIII-D target plates with the MCI code [2] indicate that velocities of order 10^{4} cm/s are typical for impurity ions near the divertor floor.

It seems reasonable from experiments done in PISCES [3] and measurements made at the University of Illinois [4] that once a significant fraction of the lithium sample liquefies it may begin sputtering neutrals at an enhanced rate. These neutrals are ionized very near the surface and the local force balance between the background deuterium ion flow toward the surface and the ion thermal gradient force away from the plate will determine what fraction of the singly ionize lithium moves upstream from the sample. As the lithium ions move upstream they radiate and locally cool the flux tubes in the vicinity of the cloud which may explain the transient drop in the SOL current on the $= 135^{o}$ TCA monitor at 3420 ms. This feature in the row 13 TCA signals is the first indication of a significant change in the local conditions near the lithium sample and most likely indicates that the current flowing out the Li DiMES sample has also dropped to zero by 3420 ms. At this point in the discharge the SOL current and the radiated power from the divertor plasma starts to become more toroidally symmetric as the cloud continues to propagate and spread.

We note that following the drop to zero at 3420 ms the current flow out of $\varphi = 135^{o}$ TCA monitor begins to build up again. At the same time the signals on the other row 13 TCA monitors start to decay. By 3425 ms the SOL currents have reestablished their original axisymmetric distribution and are all decaying toward zero. By this point in the discharge we believe the lithium cloud has spread out enough to cover most of the divertor and SOL. The lithium radiation has most likely equilibrated T_e spatially and is driving it to lower values uniformly around the SOL, which globally reduced the driving potential for $\mathbf{j}_{th}$. After t = 3427 ms $\mathbf{j}_{th}$ is essentially zero everywhere in the SOL and thus can no longer produce any significant $\mathbf{j}_{th} \times \mathbf{B}$ forces on the plasma facing components or the lithium sample.

As T_e drops in the divertor (t > 3427 ms) it appears that we reach a detached-like state across the entire divertor region with very little heat flux reaching the target plates or the lithium sample. We also note, in the upper frame of fig. 2, that the signals in the row 13 TCA monitors begin to rise again slowly at about 3455 ms following a 25 ms decay from about 5 A/tile to zero. This increase, starting at 3455 ms, results from the growth of a locked mode on the q = 2 surface, which first appears on the pr12 and pr13 locked mode detector signals at 3452 ms (see the upper frame of fig. 3). Various types of locked and resistive wall modes are commonly observed on the TCA monitor signals but the signals shown between 3455 and 3474 ms in the upper frame of fig. 2 are rather unusual in terms of the characteristics more typical of a standard locked or resistive wall mode. Locked

modes usually produce non-axisymmetric thermal electric current with amplitudes of 50-100 A/tile rather than the 10-20 A/tile seen during the locked mode on shot 105511. This difference may be attributed to a build up in the lithium density throughout the SOL and into the outer core region of the plasma. The lithium radiation should moderate the power flow from the core into the divertor and reduce the thermoelectric potential needed to drive $\mathbf{j}_{th}$.

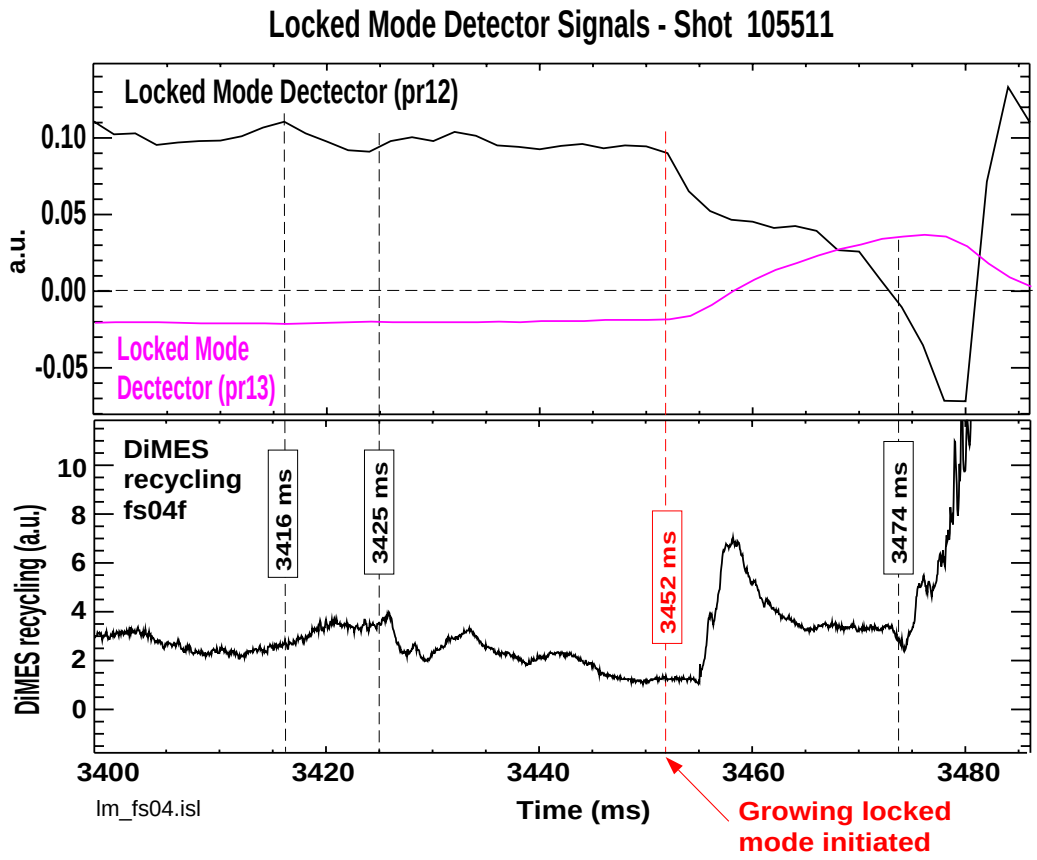

Fig. 3 - Upper frame: locked mode detector signals pr12 and pr13 show the onset of a growing locked mode at 3452 ms, Lower frame: D_α recycling light from filterscope chord 04 (fs04f) looking near the DiMES probe (see fig. 1) shows an increase in recycling as the locked mode grows after 3455 ms.

The upper frame of fig. 3 clearly shows the onset of a growing locked mode at 3452 ms compared to the earlier, relatively featureless, behavior of the pr12 and pr13 signals prior to that point. The lower frame of fig. 3 confirms the growth of the locked mode in that we see an increase in the deuterium recycling at approximately the same radial location as the DiMES probe and the row 13 TCA monitors. This signal suggests that the locked mode destroys the core confinement inside the q = 2 surface and dumps some of the heat and particles from the core into the divertor. While the lithium in the core moderates the

magnitude of the heat flux reaching the divertor targets it does not completely eliminate it during the locked mode.

As the locked mode depletes the stored kinetic energy inside the q=2 surface, the plasma beta drops and the DIII-D vertical control system is unable to prevent the plasma from moving toward the inner wall of the vessel. This triggers a rapidly growing vertical displacement event at approximately 3478 ms (about the time that Ip starts to increase as the internal inductance of the plasma changes due to a current profile redistribution) which drives the plasma downward until the x-point contacts the lower divertor target plates (somewhere in the vicinity of the DiMES probe). Once the x-point touches a lower divertor surface a rapid thermal quench dumps the remainder of the plasma's stored kinetic energy into the SOL and lower divertor. This initiates the Ip quench in which all the energy in the poloidal magnetic field is converted to kinetic energy and deposited on the plasma facing surfaces. The current quench also inductively drives large non-axis-symmetric halo currents in the SOL, which are measured with the TCA arrays. These currents can be seen in the signals of the row 13 TCA monitors (upper frame of fig. 2) starting at 3480 ms where the signals switch polarity from positive (current flowing into the tiles) to negative (current flowing out of the tiles). The full amplitude of the signals have been cut-off in the figure to emphasize the earlier features starting at about 3416 ms. The magnitude of the halo current induced during the Ip quench in shot 105511 was of 600 A/tile.

An inspection of the data from the DIII-D CO_2 laser interferrometer chords shows that the core n_e started to increase slowly ($dn_e/dt = 6.9 \times 10^{20}$ $m^{-3}s^{-1}$) from 2.5×10^{19} m^{-3} at 3428 ms until t = 3444 ms and then increased at a more rapid rate to 6.1×10^{19} m^{-3} at 3458 ms. This implies that a solid lithium fragment (or liquid droplet) with a radius of approximately 1.6-2.6 mm (or 10-40 mg of lithium) would be required in order to cause this increase in n_e. The size of the lithium droplet cannot be accurately determined due to the uncertainty in the charge state distribution of the lithium in the core. The data shown in fig. 4 supports the idea that a single fragment (or droplet) of lithium was responsible for the density increase and the radiative cooling that triggered the contraction of the edge current profile and the q = 2 locked mode.

The upper frame of fig. 4 shows the electron temperature profile at 3416 ms (black) just before the dip in the $\varphi = 135^{o}$ row 13 TCA signal. At 3426 ms the electron temperature profile (shown in yellow) appears to have dropped slightly beyond 59 cm although this type of variation is not unusual in plasmas of this type. By 3446 ms we clearly see a dramatic drop in the temperature profile beyond 54 cm (blue) while the data points inside 48 cm are not affected. This change in the electron temperature profile is well correlated with the increase in the line-integrated n_e between 3428 and 3444 ms (i.e., the slow density rise discussed above). The Thomson data for n_e at t = 3446 ms shows a substantial increase in the edge density (beyond 55 cm) which implies that essentially all of this line integrated n_e increase is due to a local source of lithium in the outer region of the plasma (i.e., outside 75-80% flux surface). This increase in density and drop in T_e is consistent with the Li-III radiation shown in the lower frame of fig. 4. Here we see that the Li-III radiation slowly starts increasing after 3425 ms (similar to the increase seen in the line integrated density). The first peak in this plot occurs at t = 3438 ms followed by a

dip and a second peak at approximately 3445 ms (roughly the time at which we see the increase in the dn_e/dt mentioned above).

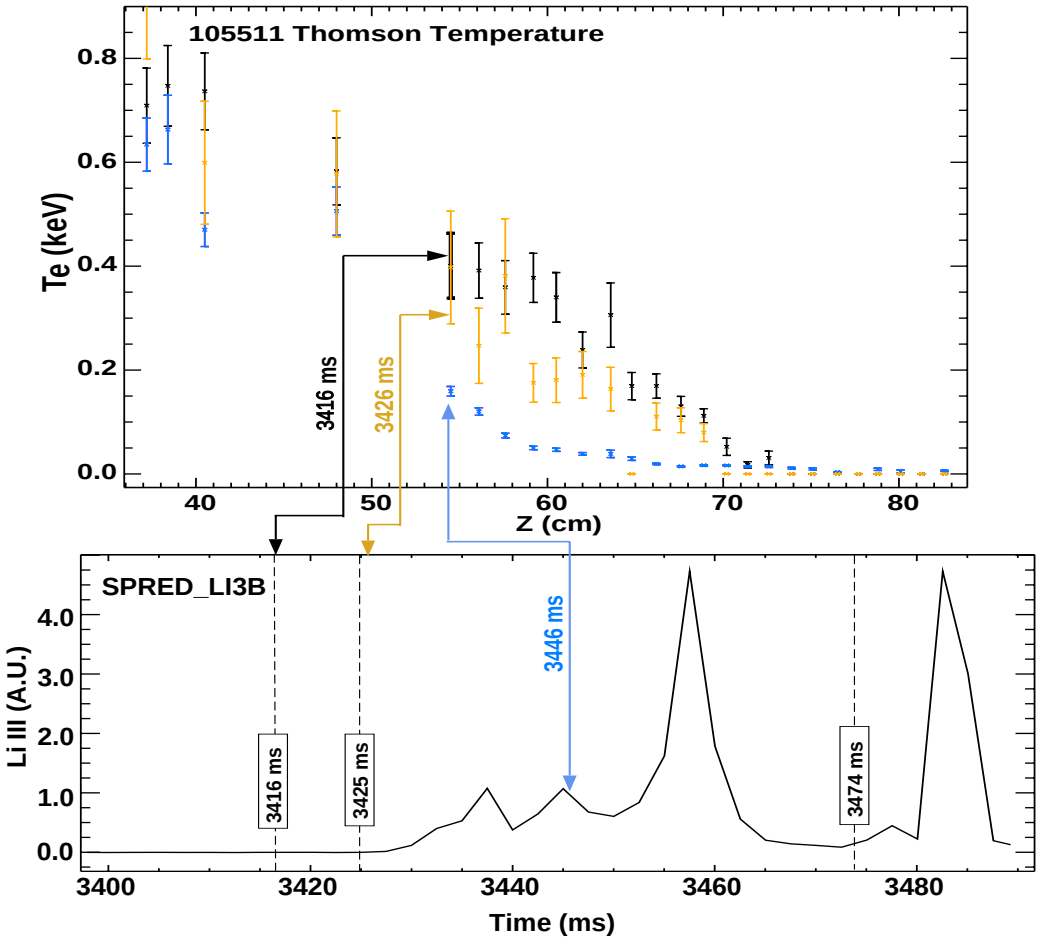

Fig. 4 - Upper frame: T_e profile as a function of vertical height along the Thomson scattering system chord at three times during discharge 105511, Lower frame: Li-III line brightness from the SPRED diagnostic system showing an increase in core lithium radiation prior to the formation of the q=2 locked mode, during the locked mode and during the disruption.

The third peak in the Li-III is well correlated with the peak in the D_α recycling light shown in the lower frame of fig. 3. This is a signature of the q = 2 locked mode which dumps part of the core heat and particles into the edge and SOL region of the plasma. The final peak in the Li-III brightness is a signature of the thermal quench and the onset of the current quench as the x-point makes contact with the plasma-facing surfaces in the lower divertor. These larger peaks suggest that a significant amount of thermal energy is released from the core during the formation of the locked mode and during the final disruption sequence.

Discussion

The data obtained during shot 105511 suggests that the lithium sample became fully or partially liquefied shortly before the dip in the $\varphi = 135^{o}$ row 13 TCA signal. Our hypothesis is that part of the free liquid surface in the DiMES sample holder arched upward and moved radially inward due to the $\mathbf{j}_{th} \times \mathbf{B}$ forces applied by the vertical component of the thermoelectric current in the flux tube connecting the sample to the inner wall (see the geometry in fig. 1). These radially extended arched blobs would have intercepted significantly more heat flux and could have released a cloud of lithium neutrals that rapidly ionized and moved up the ion thermal temperature gradient along the magnetic field. This lithium cloud may have provided a local radiative cooling mechanism that equilibrated the electron temperatures at the ends of the flux tube and drove the thermoelectric current to zero. Video images viewing the sample from above show a radial spreading of the lithium surface both inward and outward just prior to the dip in the $\varphi = 135^{o}$ row 13 TCA signal. As the thermoelectric current decayed to zero, between 3416 and 3420 ms, the vertical and radial forces on these extended lithium blobs would have also gone to zero.

Apparently, as the lithium cloud spread across the rest of the SOL, between 3420 and 3425 ms, the flux tube began to reheat and the T_e equilibration was lost. This resulted in an increase in the thermoelectric current flowing through the lithium sample. Assuming the usually polarity for this current (out of the tile on the low field side) the blob that was extended radially inward would have experienced a vertical $\mathbf{j}_{th} \times \mathbf{B}$ force pointing up toward the core plasma. This force would have been large enough to eject part of the radially extended blob up into the divertor with a velocity of order 30 m/s. Such a blob, traveling normal to the divertor surface, would have traversed the 36.5 cm distance to the edge of the hot plasma in about 12 ms. Assuming the blob was launched at the peak of the $\varphi = 135^{o}$ row 13 TCA signal (at t = 3425 ms) it would have arrived at the edge of the hot plasma roughly at the time of the first Li-III brightness peak in the lower frame of fig. 4 (t = 3437 ms). Pellets injected radially into the plasma near the midplane often emit a burst of radiation as they enter the edge of the plasma followed by a pronounced dip. This behavior is not well understood.

It is reasonable to assume that the lithium blob was not ejected perfectly normal to the divertor surface. This simply implies that the velocity of the blob has to scale as the cosine of the angle between the surface normal and the launch trajectory times 30 m/s in order to traverse the divertor in 12 ms. Thus a launch angle of 45^{o} off the surface normal implies a velocity of about 42 m/s as opposed to 30 m/s for a surface normal launch. Using this velocity we find that the second peak in the Li-III signal, which occurs about 7-8 ms after the first, would have put what was left of the blob about 24 cm into the bottom of the plasma or roughly at the vertical height of the outermost dashed flux surface shown in fig. 1. This flux surface corresponds to a z of 59 cm for the Thomson chord shown in fig. 4, which is about where the slope in the radial T_e profile becomes significantly steeper. This second peak in the Li-III brightness probably corresponds to the final ablation phase of the blob and suggests that all of the lithium originally

contained in the blob was deposited outside the region defined by the midpoint of the two outer dashed flux surfaces shown in fig. 1. Thus, the data suggests a vertical penetration depth of between 20 to 35 cm from the separatrix location.

The ablation physics involved in the flight of this blob through the divertor and core plasma is complicated by the fact that it is not a cryogenic solid material (for which most ablation theories apply) and it is most likely a liquid rather than a solid. The ablation of refractory materials such as lithium and carbon involve significantly different physics effects than that of cryogenic materials such as deuterium and helium. The ablation of liquid helium jets has been discussed by Parks et al. [5] but in the case of a large, slow (~ 30 m/s) moving, free surface liquid droplet or blob effects such as deformation and/or breakup could have a significant impact on the ablation rate and thus on the penetration depth. Nevertheless, we can make a rough order-of-magnitude approximation of the penetration depth (L_{pen}) using the following approach and assuming a launch normal to the sample surface:

$$L_{pen} = N_{blob} v_{blob} (dN_{blob}/dt)^{-1} \qquad (1)$$

where N_{blob} is the number of lithium particles in the blob, v_{blob} is the velocity of the blob, and dN_{blob}/dt is the ablation rate of the blob. Neglecting the effects such as plasma elongation we have from refs. 5 and 6 the following expression for the Li ablation rate:

$$dN_{blob}/dt = 4.47\times10^{15} M^{-1/3} r_b^{4/3} n_e^{1/3} T_e^{5/3} \qquad (2)$$

where M is the atomic mass of the lithium, r_b is the radius of the blob, n_e is the electron density and T_e is the electron temperature. In the divertor we assume an average temperature along the path of the blob of 20 eV and an average density of 2.0×10^{19} m^{-3}. Using a 10 mg initial mass we have $N_{blob} = 6.0\times10^{21}$ particles and take the velocity to be v_{blob} = 30 m/s. This results in a divertor plasma penetration depth of approximately 300 m. Along the vertical path of the blob in the core plasma we assume an average temperature of 600 eV (based on the upper frame of fig. 4) and an average density of 3.0×10^{19} m^{-3}. This results in a core penetration depth of approximately 0.9 m (i.e., near the center of the discharge and not unreasonable considering the device dimensions shown in fig. 1). These rough approximations of the penetration depths in the divertor and core are at best correct to within a factor of 2 or 3 since we have not taken into account plasma profile effects and the complexities that are involved with the ablation of a liquid blob. In addition, the leading constant used in eqn. 2 is for helium and certainly will be somewhat different for a refractory liquid such as lithium.

These rough estimates of the lithium blob penetration demonstrate that the divertor plasma would have had relatively little effect on the flight of the object as it passed through this region. The relatively small ablation rate in the divertor should have removed only a small fraction of the original blob. This is qualitatively consistent with the small, slowly increasing, Li-III signal between 3425 and 3437 ms shown in the lower frame of fig. 4. This estimate also highlights the fact that once the blob enters the core plasma the ablation rate is substantially enhanced by the higher T_e (where T_e on axis is 1.7 keV). Thus, most of the blob's mass (probably about 95%) is deposited in the outer

region of the core plasma, which is also consistent with the Li-III signal in fig. 4. A more accurate estimate of the divertor and core penetration depths has been carried out using an ablation code, which accounts for the shape of the T_e profile. While the code does not account for the liquid material effects, it does include refractory material effects. The results of the code runs for shot 105511 with a 5.2 mm diameter (40 mg) solid fragment of lithium is L_{pen} = 0.66 m. This agrees reasonably well with the rough estimate made above for the penetration depth. We note that both the penetration depth from the rough analytic estimate and from the ablation code predict a deeper penetration than the T_e profile data shown in the upper frame of fig.4 suggests. This can be accounted for if we assume a launch angle with a toroidal component. This would increase the ablation path length and reduce the penetration depth. In addition, since the detailed ablation physics of a liquid droplet is not accounted for in these calculations that could easily result in an over estimate of the penetration depth.

Conclusions

Experiments in DIII-D have shown that when a small 2.54 cm diameter lithium sample composed of layered foils is exposed to the SOL heat flux profile near the outer strike point of an L-mode plasma for approximately 2500 ms (during the Ip plateau) the core Li-III radiation peaks rapidly resulting in an edge radiative collapse followed by locked mode and a plasma current disruption. An analysis of data from these experiments suggests that the disruption sequence was most likely initiated by the injection of a single large blob of liquid lithium, moving at approximately 30 m/s, which penetrated about 35-40 cm into the core plasma before burning out.

The sequence of events see in DIII-D can be divided into three distinct phases. The first involves the initial ejection of the blob, which probably accounts for loss of about 5-10% of the initial mass of the sample. The second involves the heat flux and current from the locked mode which probably accounts for the removal of another 20-30% of the initial mass and the third phase involves the disruptive thermal quench and halo currents which probably account for the removal of the remaining 60-75% of the initial mass of the sample. Each of these phases involve complex physics issues that are not completely understood at the present time suggesting that additional experimental measurements are needed and that the development of more advances theoretical tools will be required to full asses the plausibility of using liquid metals as plasma facing materials in high heat flux regions of the vessel, particularly when SOL currents are also present. We are working with the UCLA modeling group to understand the MHD effects leading up to the injection of the lithium blob since a key issue for future research is whether MHD effects, such as those discussed above, can be avoided with flowing system or a different choice of geometry.

Acknowledgements

We would like to thank Dr. P. Parks for providing data from his pellet ablation code on the ablation of solid lithium fragments .

References

[1] C. P. C. Wong, et al., ., J. Nucl. Mater., **258-263** (1998) 433

[2] T. E. Evans, D. F. Finkenthal, M. E. Fenstermacher, et al., J. Nucl. Mater., **266-269** (1999) 1034

[3] D. Whyte, personal communication.

[4] J. P. Allain, personal communication.

[5] P. B. Parks, M. N. Rosenbluth, S. V. Putvinski, and T. E. Evans, Fusion Tech., **35** [1999] 267.

[6] B. V. Kuteev, V. Yu Sergeev, and S. Sudo, Nucl. Fusion, **35** (1995) 1167.

4.0 Heat Transfer in Liquid Surfaces

Heat Transfer in Liquid Surface PFCs

ALPS Heat Transfer Group
Richard E. Nygren, Sandia National Laboratories
Claude Reed, Argonne National Laboratories
Sergei Molokov, Coventry University
Tina Tanaka, Tom Lutz, Jim McDonald, Ken Troncosa, Mike Ulrickson,
Bob Bastasz and Mike Clift, Sandia National Laboratories

The evaluation of the heat removal capability is a very basic performance parameter for liquid surface (LS) concepts. Designing reasonable experiments to measure this capability is challenging and will require thoughtful development. The initial efforts in ALPS on heat transfer have focused on characterization of the issue through simple calculations and planning and simple experiments on liquid metal surfaces to get some experience with the challenges that we may face in diagnostics for future liquid surface PFC tests.

Magneto-hydrodynamic (MHD) effects control the flow of liquid metals in a magnetic field and this in turn affects heat transport. The primary MHD effects are (1) the suppression of turbulence that would more rapidly distribute heat throughout the bulk of the flowing liquid in the absence of a magnetic field and (2) a large pressure drop.

The maximum heat load that a liquid plasma facing surface can sustain for steady state applications is limited by the surface temperature at which the impurity influx into the plasma from vaporization is unacceptable.

The areas addressed in heat transfer are:

- MHD activities
- IR measurements on Liquid Metals
- Sn-Li melting Experiment
- Li loop development
- Li handling experience
- Heat flux limits for flowing liquids
- Notes on the thermal Properties of Sn
- IR camera at UCLA and CDXU

1. MHD Activities

S. Molokov (Coventry University), C.B. Reed (ANL)

1.1. An International Collaboration for MHD Experiments on Jet Divertors

1.1.1 Summary

Progress on understanding MHD effects in ALPS and specifically the MHD issues associated with a jet-based liquid metal divertor has reached the point where MHD experiments are needed to compare with modeling results obtained thus far. A comprehensive plan is summarized which brings together key MHD people and institutions from around the world to form an international collaboration on MHD experiments and modeling for jet divertors in ALPS/ALIST. Several of the collaborators and/or institutions can provide some of their own funding, making this a high leverage activity.

1.1.2 Background

In Molokov & Reed (2000a), a comprehensive review of available free surface MHD work was undertaken to lay the groundwork for selecting the most promising approach for an ALPS free surface divertor, from an MHD point of view. The three main concepts covered by the review included a flowing film, a jet curtain or jet-based scheme, and a droplet curtain. The recommendation, based on the review, was to pursue jet-based divertor designs.

Work in 2000 identified the main thermal, fluid, and MHD problems associated with a jet divertor listed in Table 1.

Table 1. MHD Problem Areas for Jet Divertors

1	Pressure drop in the supplying duct due to a nonuniform field and bending of the duct
2	Transition from duct flow to manifold flow (the manifold problem)
3	Transition from manifold flow to nozzle flow
4	Transition from duct flow to jet flow (the nozzle problem) and the meniscus effect
5	Jet stability in both steady state and transient magnetic fields
6	Heat transfer analysis, including thermocapillary convection
7	Impact of a jet on a liquid metal surface
8	Impact of a jet on a solid wall, and splashing
9	LM film or rivulet
10	The problem of draining

These ten problem areas are illustrated in the figure below.

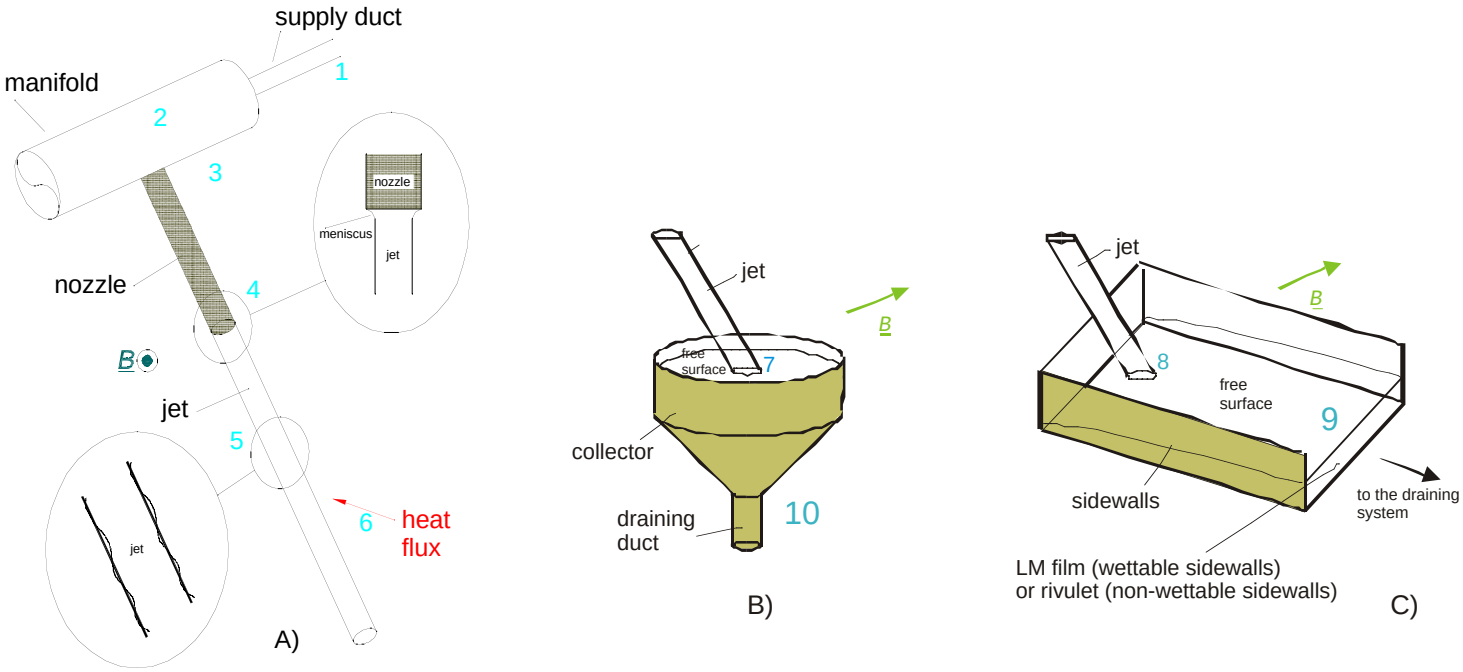

Substantial results for area 1 (pressure drop in the supplying duct due to a nonuniform field and bending of the duct) are reported in detail below. Rivulet results, area 9, were published last year, (Molokov & Reed, (2000b) and Molokov, Cox & Reed (2001)). Preliminary results in areas 4 (transition from duct flow to jet flow (the nozzle problem) and the meniscus effect) (Molokov & Reed, (2000d)), and 6 (heat transfer analysis, including thermocapillary convection) (Molokov, Cox & Reed (2001)) were also reported this year. First results on the problem of splashing, area 8, were reported in Molokov (2000) and at an ALPS Project Meeting Molokov & Reed, (2000d).

1.1.3 The Collaboration

Presently, all ANL MHD efforts are directed at the modeling side of the jet divertor problem. However, all ten of the areas identified in Table 1 are complex three dimensional problems for which experiments will be required to guide and benchmark the theoretical and modeling work.

At the recent Fourth International Pamir Conference on MHD at the Dawn of the Third Millennium (September 2000), summaries of the current modeling work on the ALPS jet divertor, were presented Molokov (2000) and Molokov & Reed, (2000c). Based on these two presentations, a number of conference attendees expressed an interest in participating in future phases of the ALPS jet divertor MHD work, both experimental and analytical.

To capitalize on this expression of interest, and the MHD expertise of these researchers, a meeting was organized at Coventry University, in June 2001, to establish an international collaboration on fusion-related liquid metal MHD in support of ALPS/ALIST. The list of attendees included:

S. Molokov	(Coventry, UK)
S. Aleksandrova	(Coventry, UK)
I. Cox	(Coventry, UK)
L. Bühler	(Karlsruhe, Germany)
O. Lielausis	(Riga, Latvia)
Y. Kolesnikov	(Riga, Latvia)
F. Debray	(Grenoble, France)
V. Bojarevics	(Greenwich, UK)
R. Moreau	(Grenoble, France)
C. B. Reed	(Chicago, USA)
Z. Xu	(Sichuan, China)
M. Ulrickson	(Albuquerque, USA)
Th. Alboussiere	(Cambridge, UK)
J. Reimann	(Karlsruhe, Germany)

The near term central goal of the Collaboration is to develop models and perform experiments on jet divertors within the context of the ALIST working group of ALPS. One of the major attractions of the Collaboration is the opportunity to perform free surface MHD experiments at the Grenoble High Magnetic Field Laboratory (GHMFL), in fusion relevant MHD parameter ranges.

Briefly, the key individuals and their level of interest are as follows:

Coventry University, Prof. Sergei Molokov

Prof. Molokov is currently leading the ALPS MHD modeling effort. He has previously performed MHD modeling work at FzK and also at the Institute of Physics in Latvia, and is quite familiar with the main researchers in the MHD free surface field working at both of these institutions. Prof. Molokov also maintains his previous contacts with the lead magnet test engineer from the Grenoble High Magnetic Field Laboratory (GHMFL), Dr. Francois Debray. Prof. Molokov organized the Coventry meeting.

Grenoble High Magnetic Field Laboratory (GHMFL), Dr. Francois Debray

One of the highest leverage aspects of this Collaboration is the use of GHMFL at no cost for EC researchers. GHMFL was built to meet the requirements of scientists for high magnetic field experiments. It is located in Grenoble, France, a French-German laboratory, jointly operated by the Max Planck Institute fÜr FestkÖrperforschung, in Stuttgart (MPI-FKF) and the Centre National de la Recherche Scientifique (CNRS). Scientists have access to the magnetic field facility provided they have written a proposal for experiments in high magnetic

fields and have obtained the approval of the Program Committee to carry out their research, DeBray, et. al. (2000). Five years ago the Laboratory undertook the development of 20 MW magnets. Two of them are now in operation and deliver fields up to 30 Tesla in a room temperature bore of 50 mm diameter. A 20 MW magnet consists of two concentric 10 MW magnets. The outer 10 MW part alone achieves a field up to 10 Tesla in a 376 mm diameter bore. This large diameter is convenient for MHD flow studies under high, fusion-relevant, magnetic fields. A preliminary discussion with Dr, DeBray at the Pamir Conference led to his attending the Coventry meeting and a follow-up presentation to the GHMFL Laboratory Director, Reed & Molokov (2001), in which it was described how the GHMFL magnets would be used to carry out the collaborative jet testing. Based on our description of the Collaboration, Dr. Debray indicated that a series of MHD jet experiments could be scheduled in the 286 mm bore 6T solenoid magnet within a few months following an application to the Program Committee by the Collaboration.

Table 2. Overview of GHMFL Jet Test Collaboration

Timing	Year 1	Year 2	Years 3-4	Years 4+
GHMFL Magnet	M5 (10 MW)	M5 (10 MW)	M9 (20 MW)	Under Construction
B-field, T	6	6	10	7
Magnet Bore, mm	286	286	376	800
Field time scale	Steady State	Steady State	SS & Transient	SS & Transient
Table 1 Area	4, 5	3, 4, 5	1-5, 7-10	1-5, 7-10

Institut National Polytechnique (INP) de Grenoble (MADYLAM)
Profs. R. Moreau, Y. Fautrelle and Dr. Jacqueline Etay

MADYLAM is a free standing MHD laboratory within INP. The MADYLAM staff have a longstanding interactive history solving industrial MHD-related free surface problems in steelmaking and Al refining. Prof. Moreau attended the meeting at Coventry University on establishing the international collaboration. At a follow-up meeting and presentation at MADYLAM, Prof. Moreau and his staff indicated a strong interest in joining the Collaboration. It was also pointed out that the close proximity of MADYLAM to GHMFL, and previous successful collaborations between the two Laboratories, would make the MADYLAM contribution even more effective. Prof. Moreau and his staff have submitted a specific proposal to participate in the Collaboration. Their collaborative activities will be both experimental and analytical in nature. The modeling work will be done collaboratively with Prof. Molokov. The MADYLAM staff will be supported from their own internal R&D funds; only the support of a Post Doc. researcher is required from ALPS funding. The bulk of the experimental work will be performed in the MADYLAM laboratories (without a magnetic field) where a gallium jet experimental apparatus will be constructed and made operational. Following these shakedown tests, the jet apparatus will be transported within Grenoble to GHMFL for experiments at 10 Tesla and higher.

An overview of the progression of these GHMFL experiments is given in Table 2. The companion modeling activities will guide the experiments and the models will be benchmarked by the GHMFL data.

Forschungszentrum Karlsruhe, Drs. J. Reimann, R. Stieglitz and L. Buhler

Drs. Reimann and Stieglitz are the main FzK MHD experimentalists, they and Buhler participated in the ANL-FzK flow tailoring collaboration. At the Pamir Conference, the FzK people expressed an interest in re-establishing the ANL-FzK collaboration of the late 1980's and early 1990's. The collaborative activities would be both experimental and analytical in nature. The modeling work performed by Dr. Buhler would be done collaboratively with Prof. Molokov. Drs. Reimann and Buhler attended the meeting at Coventry University on establishing the international collaboration. In a follow-up meeting at FzK, a number of options were discussed for broadening the scope of their current activities to include the free surface PFC area, thereby opening the door for their participation in the Collaboration. FzK's involvement is being pursued as an important element of the Collaboration.

Institute of Physics, Latvia, Prof. Olgerts Lielausis

Some of the most recent and most relevant jet divertor experiments were performed at the Institute of Physics, Bucenieks et. al. (1994). Their role will be both modeling and experimental; possibly providing instrumentation, or some part of the main experimental apparatus, or performing experiments in their laboratories on one of the ten issues identified above. Prof. Lielausis attended the meeting at Coventry University on establishing the international collaboration.

Southwestern Institute of Physics (SWIP), China

ANL participated in a personnel exchange with SWIP in the early 1990's; Dr. Zengy Xu spent 6 months at ANL/ALEX helping with the conversion from NaK to Li. The groundwork to re-establish this collaboration was laid during the past year. Dr. Xu attended the meeting at Coventry University on establishing an international collaboration in fusion-related liquid metal MHD and agreed to redirect his ongoing experimental MHD program on manifolds and 3D MHD effects in insulated ducts, to support the Collaboration in areas 1 (pressure drop in the supplying duct due to a nonuniform field and bending of the duct), 2 (transition from duct flow to manifold flow (the manifold problem)), and 10 (the problem of draining) of Table 1. ANL is also coauthoring an ISFNT-6 paper with SWIP on the MHD effects of defects in insulator coatings. Additionally, with ANL support, Prof. Molokov is offering a Master's-Ph.D. scholarship award at Coventry University to a young MHD researcher from SWIP. The purpose of this scholarship is to transfer a strong theoretical and modeling capability to the SWIP researchers. The researcher has been identified, and she will begin her studies at Coventry in the fall of 2001.

1.1.4 Conclusion

A high leverage international collaboration in support of both the modeling and experimental needs of the ALPS/ALIST jet divertor task area has been initiated. Some additional funds will be required to support increased efforts at ANL, at Coventry for more of Prof. Molokov's time, and some funding to support a Post Doc. at MADYLAM in Grenoble. The payoff is very high; MHD testing at reactor relevant fields and near reactor relevant sizes. This collaboration is expected to bridge the experimental gap in MHD work for the next several years.

1.2 Modeling MHD duct flow with insulated walls

1.2.1 Introduction

Magnetohydrodynamic (MHD) flows in circular ducts play a fundamental role in liquid metal blankets and divertors for fusion reactors. Concerning blankets, both inlet and outlet pipes have circular cross-section. A circular inlet pipe, for example, supplies a liquid metal from outside of the reactor area, where no magnetic fields are present, then enters a strong, nonuniform magnetic field, bends, and extends up to a manifold that feeds an array of coolant ducts (see e.g. Hua&Gohar, 1995). The flow is fully three-dimensional, since there is a combined effect of a strong, nonuniform magnetic field and bending. Similar characteristics has flow in divertor elements, where a circular duct bends in a nonuniform magnetic field region (Karasev, Tananaev (1990), Mattas et al. (2000)).

When a liquid metal flows in a strong magnetic field, electric currents are induced. These currents in turn interact with the magnetic field and the resulting electromagnetic force induces a high MHD pressure drop and significant nonuniformities of the velocity profile in the duct cross-section. The pressure drop in particular is considered to be one of the most critical issues for self-cooled blankets. The magnitude of the electromagnetic force with respect to viscous and inertial forces is determined by two parameters, the Hartmann number, Ha, and the interaction parameter, N, respectively. For large-scale tokamaks, such as ARIES and ITER, the value of both parameters may reach very high values, of the order of 10^5, which means that the electromagnetic forces dominate both viscous and inertial forces. For smaller machines, such as NSTX the parameters are far lower: Ha = 10-10^2, N = 0.5-50. The latter parameter range is also characteristic for some laboratory experiments. The values of parameters for C-MOD are in the intermediate range.

To reduce the MHD pressure drop duct walls are made electrically insulating, which results in electric currents of lower magnitude. Most recent designs of blankets and divertors assume that the walls are covered with insulating coatings which provide perfect, or almost perfect electrical insulation. Reed et al (1995) show experimentally that the pressure drop in a round pipe covered with an insulating coating is indeed significantly reduced with respect to that with bare conducting walls.

Even with perfect insulation, however, MHD effects are not completely eliminated. Pressure drop owing to three-dimensional effects may still reach sufficiently high values to remain an important issue for self-cooled blankets and divertors. There are also questions as to how sensitive is the flow to various parameters, such as the Hartmann number, the magnitude of the field gradient, the position of the nonuniform field region in the duct, the degree of bending, etc. We address these issues in the three-part study.

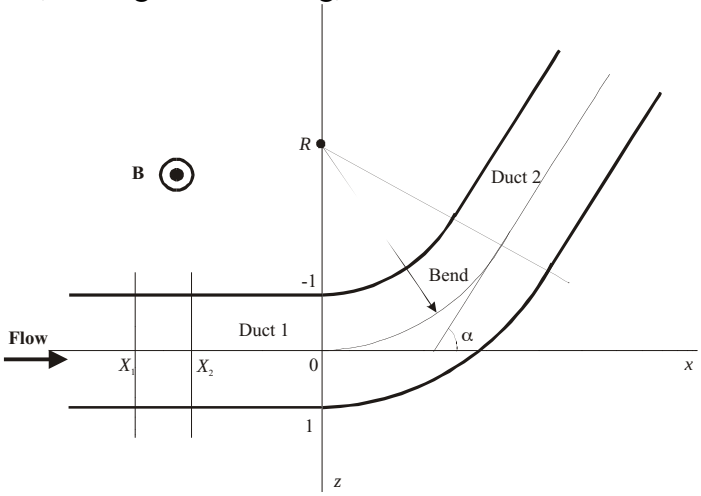

Figure 1. Schematic diagram of the flow in a bended cirdular duct: projection on the (x,z)-plane

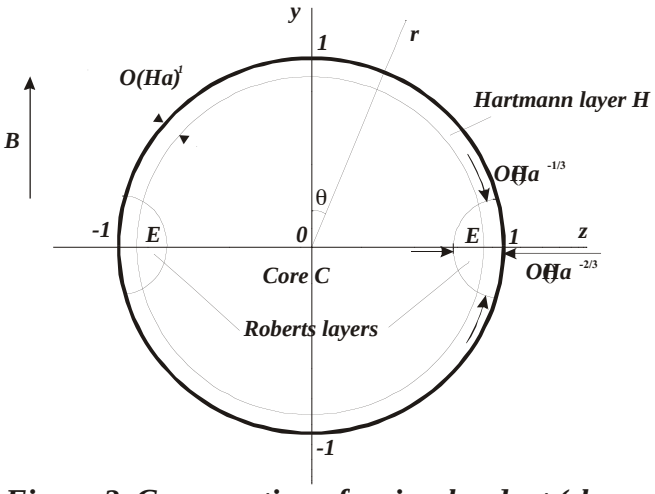

Figure 2. Cross-section of a circular duct (shown for Duct 1) and the flow subregions at high Ha.

We are concerned with a combined effect of duct bending and a nonuniform magnetic field on a liquid metal flow in an insulating circular duct (figure 1). The geometry consists of two straight ducts, Duct 1 and Duct 2, which are connected by a Bend. The axis of the resulting curved duct is in the (x,z)-plane. The transverse cross-section of all ducts is a circle of constant dimensionless radius of 1 (figure 2); the dimensional radius of the duct, a^*, has been chosen as the characteristic length of the

problem. The external magnetic field $\mathbf{B} = B(x,z)\hat{\mathbf{y}}$ has a single component. It is directed along the y-axis, i.e. out of the plane of the figure. We present the results for a particular type of fields that have a constant level, B_u, to the left of the line $x = X_1$ and B_d to the right of the line $x = X_2$ (see figures 1 and 3). The field is nonuniform between X_1 and X_2. The gradient of the field is aligned with the axis of Duct 1, while it is inclined by an angle of a to the axis of Duct 2 in the (x,z)-plane.

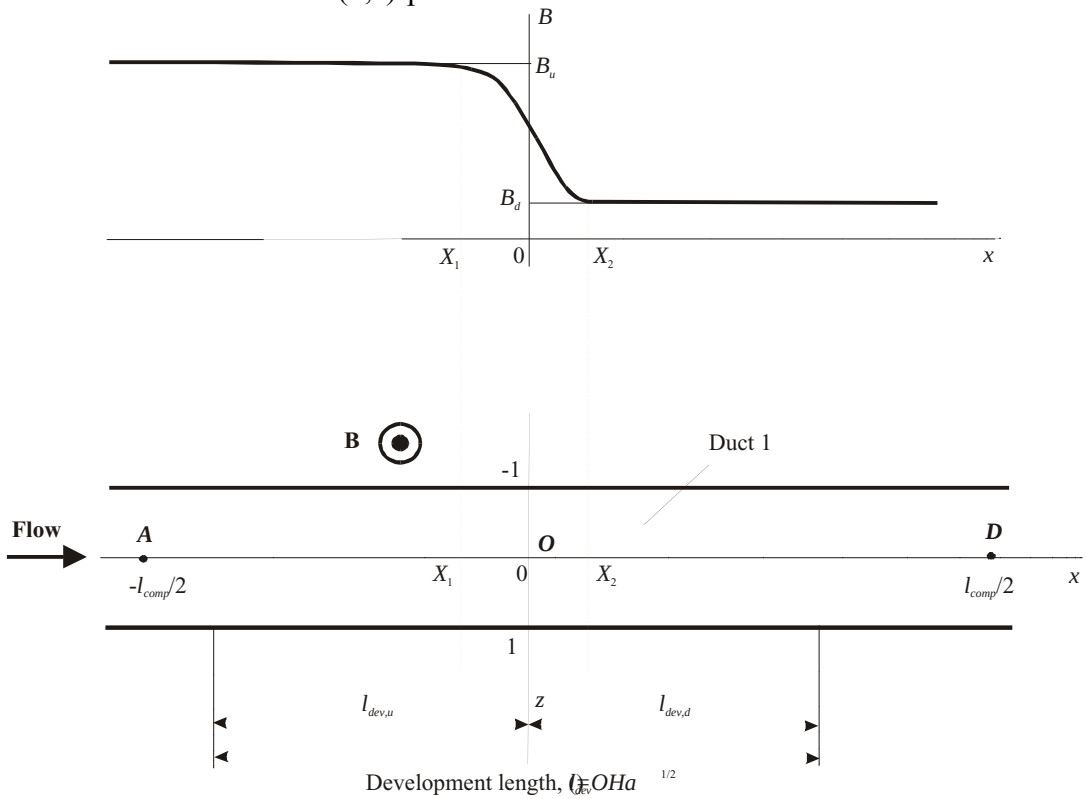

Figure 3. Schematic diagram of the flow in a straight circular duct (Duct 1): (a) nonuniform magnetic field and (b) projection of the duct on the (x,z)-plane

We perform a parametric study of the problem, in which we vary many flow parameters, among those are the positions X_1 and X_2, which determine the field gradient, angle a, the Hartmann number Ha, field levels B_u and B_d, etc.

For better understanding of the flow we separate the effects first. Thus the investigation consists of three parts. In the first part (Molokov&Reed, (2001a)) we study the flow in a straight duct in a fringing field $\mathbf{B} = B(x)\hat{\mathbf{y}}$, which varies along the duct only. This situation is relevant when both X_1 and X_2 are sufficiently far upstream from the bend region. When X_1 and X_2 are in the Duct 2 region far downstream, there is an effect of the inclination of the gradient of the nonuniform field to the axis of the straight circular duct. This effect is studied in Part 2 (Molokov&Reed (2001b)). Part 3 of the study (Molokov&Reed (2001c)) focuses on the effect of bending itself, as well as the combined flow shown in figure 1. The results of Part 3 of the study will be presented in next year's report.

In this study we use Hua&Walker's (1989) (hereinafter referred to as HW89) approach as a starting point. We use a different numerical scheme than that by HW89. Our finite-difference grid is nonuniform in the flow direction. This is done in order to cluster grid points in the nonuniform field region, where significant variations of the flow variables occur. As a result, our numerical code is able to treat flows at very high Hartmann numbers.

1.2.2 Flow in a straight duct

1.2.2.1 Summary

In the first part (Molokov&Reed (2001a)) of a three-part study the flow in a straight duct in a fringing magnetic field is considered. The magnetic field is uniform with two different levels upstream and downstream. In the region of a nonuniform magnetic field the gradient of the field is aligned with the duct axis. The flow is assumed to be inertialess. It is analysed using an asymptotic flow model at high values of the Hartmann number, Ha. The analysis leads to two two-dimensional partial differential equations for the core pressure and the electric potential of the duct wall. These equations are solved numerically using central differences on a transformed grid. It is confirmed that for the flow in insulating circular ducts the three-dimensional effects are very significant. For fusion-reactor parameters the three-dimensional pressure drop is equivalent to the extension of the length of the duct with fully developed flow by 10-150 diameters. Finally, the effect of the finite length of the magnet in magnetohydrodynamic experiments has been evaluated.

1.2.2.2 Formulation

Consider a steady, three-dimensional flow of a viscous, electrically conducting, incompressible fluid in a straight, insulating, circular duct in the x-direction (figures 2 and 3). A strong, nonuniform, transverse magnetic field $\mathbf{B}^* = B^*_0 B(x)\hat{\mathbf{y}}$ is applied, where B_0^* is a characteristic value of the magnetic field. In this study B_0^* is the level of the uniform magnetic field in the upstream region, i.e. for $x \to -\infty$. Here we use Cartesian co-ordinates (x,y,z). Dimensional quantities are denoted by letters with asterisks, while their dimensionless counterparts - with the same letters, but without the asterisks. The characteristic values of the length, the fluid velocity, the electric current density, the electric potential, and the pressure are a^* (the duct radius), v_0^* (average fluid velocity), $\sigma v_0^* B_0^*$, $a^* v_0^* B_0^*$, and $a^* \sigma v_0^* B_0^{*2}$, respectively. In the above, s, r, n are the electrical conductivity, density and kinematic viscosity of the fluid, respectively.

It is assumed that the flow is inertialess, which requires (see Holroyd&Walker (1978))

$$N >> Ha^{1/2}, \quad (1)$$

where $Ha = a^* B_0^* (\sigma/\rho\nu)^{1/2}$ is the Hartmann number, which expresses the ratio of the electromagnetic to the viscous force, and $N = a^* \sigma B_0^{*2} / \rho v_0^*$ is the interaction parameter, which expresses the ratio of the electromagnetic to the inertial force. The problem is analysed for high values of the Hartmann number.

1.2.2.3 Asymptotic analysis at high Ha

In a sufficiently strong magnetic field the flow region splits into the following subregions (figure 2):

- the core C
- the Hartmann layer H of thickness $O(Ha^{-1})$ at the wall;
- the Roberts layers E with dimensions $O(Ha^{-1/3}) \times O(Ha^{-2/3})$.

The asymptotic solution for the core and the Hartmann layers leads to two two dimensional equations for the core pressure, P, and the wall potential, F. These equations, subject to proper boundary conditions, are solved numerically.

1.2.2.4 Numerical Method

A different numerical scheme to that employed in HW89 is used, as discussed below. In order to account for high development length, the length of the computational domain, l_{comp}, in the x-direction (see figure 3) must be sufficiently high. In insulating circular ducts the development length is $O(Ha^{1/2})$. Therefore, it is anticipated that for Ha = 10,000, for example, the computational domain would need to be about 50 duct diameters. On the other hand, main flow changes occur at or near the nonuniform-field region, which, perhaps, equals only 5 duct diameters. Therefore, a nonuniform grid is introduced in the x-direction by means of the following co-ordinate transformation (Tanehill, Anderson & Pletcher (1997, p.337)):

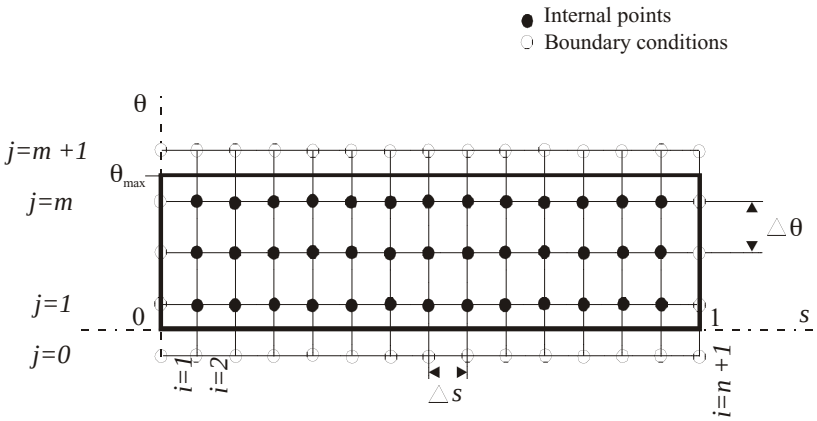

Figure 4. Computational domain in the (s,θ)-plane

$$x = \frac{1}{2} l_{comp} \frac{\sinh \tau(s - \frac{1}{2})}{\sinh \frac{1}{2}\tau}, \tag{2}$$

$$s = \frac{1}{2} + \frac{1}{\tau} \sinh^{-1}\left(\frac{2x}{l_{comp}} \sinh \tfrac{1}{2}\tau \right), \tag{3}$$

which stretches the vicinity of x = 0. In the above s is the new, transformed variable, which varies between 0 and 1, and t is the stretching parameter. Parameter t varies in the range $0 \le \tau < \infty$; for t = 0 there is no stretching and the grid becomes uniform.

The problem for P and F formulated on the (s,q)-plane, where q = arcsin z) is solved using finite differences on a regular, non-staggered grid (figure 4). The values of P and F are defined at the same grid points, which differs with HW89. Central differences are used throughout. The grid is positioned in such a way that the lines q = 0 and $q = q_{max}$ are located between two grid lines, as shown in figure 4. This is convenient (but not necessary) for treatment of the derivative boundary conditions at these lines. We use a direct method to obtain the solution of the resulting system of linear equations, which employs a sparse matrix solver. This eliminates possible convergence problems characteristic of iterative methods reported by HW89.

For a typical calculation we use 129 points in the s-direction (n = 128) and 22 points in the q-direction (m = 20). A sensitivity study of the solution to the stretching parameter t has been performed, and the value t = 10 has been selected to cover all the cases studied here with sufficient accuracy. Typical calculation with these parameter values requires about 30secs on a 700MHz AMD Athlon processor.

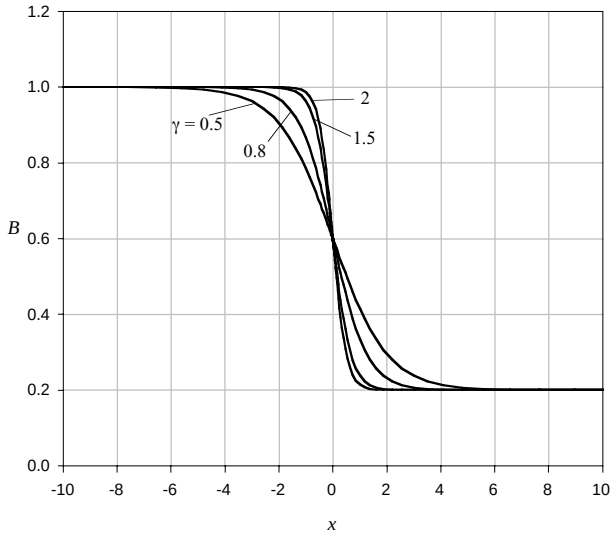

Figure 5. Magnetic fied distribution for B_d=0.2 and for several values of γ.

1.2.2.5 Results

In the following we consider a step-like magnetic field given by the expression

$$B = \frac{1}{2}(B_d + B_u) + \frac{1}{2}(B_d - B_u)\tanh \gamma x\,, \tag{4}$$

which varies between constant values of B_u and B_d, its levels upstream and downstream, respectively. With the chosen normalization, $B_u = 1$, while the value of B_d varies between 0 and 1 (flow out of the intense-field region). The value of B_d cannot be set to zero, since it would violate the asymptotic requirement $B_d Ha >> 1$. The lowest value of B_d used here is 0.1, while the results for $B_d = 0$ may be obtained by linear extrapolation.

The field gradient is defined in Eq. (4) by g. The family of the magnetic fields (4) is shown in figure 5 for $B_d = 0.2$ and for various values of g. The field for $B_d = 0.2$ and g = 0.8 approximates that used in HW89.

The aim of this study is to give an assessment of the importance of the three-dimensional effects in insulating circular ducts. There are several such characteristics: the

three-dimensional pressure drop, the development length, and the three-dimensional length. They are defined below.

The first characteristic of the three-dimensional effects is the development length, l_{dev}. The development lengths upstream, $l_{dev,u}$, and downstream, $l_{dev,d}$, of x = 0 are defined as the distance from point O (figure 3), where the z-component of the core current, $j_{z,C}$, deviates from its fully developed value by no more than 10%. In the fully developed flow $j_{z,C} = \frac{3}{8}\pi Ha^{-1}$ for both upstream and downstream regions. Therefore, one gets the condition h < 0.1, where

$$\eta = \left| \frac{8Ha}{3\pi} j_{z,C} - 1 \right| , \tag{5}$$

which determines both $l_{dev,u}$ and $l_{dev,d}$.

Total development length is

$$l_{dev} = l_{dev,u} + l_{dev,d} .$$

The second characteristic is the so-called three-dimensional pressure drop, Δp_{3D}. Consider two points, A and D, taken in the fully developed flow regions upstream and downstream at a certain distance from point O in both directions (i.e. from x = 0, see figure 3). This distance is taken as $l_{comp}/2$ in this paper, as shown in figure 3. The total pressure drop between these two points is denoted by Δp. Now, far upstream and far downstream the flow is fully developed, while the axial pressure gradients are constant and equal to

$$\left.\frac{dp}{dx}\right|_{upstream} = -\frac{3\pi B_u}{8Ha}, \quad \left.\frac{dp}{dx}\right|_{downstream} = -\frac{3\pi B_d}{8Ha}, \tag{6}$$

respectively. The fully developed pressures are extended from points A and D to the point O (cf. figure 9), where the field equals to the average value of B_u and B_d. The resulting difference in pressures is called the three-dimensional pressure drop:

$$\Delta p_{3D} = \Delta p - \frac{3\pi l_{comp}}{16Ha}\left(B_u - B_d\right). \tag{7}$$

The third characteristic of the three-dimensional effects is the so-called three-dimensional length, d_{3D} (not to be mixed with the development length). It is defined as follows:

$$d_{3D} = -\frac{\Delta p_{3D}}{dp/dx\big|_{upstream}} = \frac{8Ha}{3\pi}\Delta p_{3D} . \tag{8}$$

Sometimes, to get a rough estimate of a pressure drop in the blanket, one uses the formulas (6) for the fully developed flow, disregarding the three-dimensional effects. In a fully developed flow - dp/dx gives the value of the pressure drop per unit length of the duct. Therefore, d_{3D} indicates the additional length of the duct that one needs to add to account for the three-dimensional effects. For example, if d_{3D} equals to one or two duct radii, then the three-dimensional effects are negligible, while for $d_{3D} > 100$ the three-dimensional effects dominate. All these three characteristics will be discussed in the following Sections.

Reference case

As a reference case we consider the flow close to that discussed in HW89, namely Ha = 7000, g = 0.8, $B_d = 0.2$. These values are used further in all cases unless otherwise stated explicitly. For calculations in the reference case we use $l_{comp} = 100$.

The results of calculations are shown in Figs. 6-11. Far upstream and far downstream the flow is fully developed. It is driven by the pressure gradients given by the first and the second expressions in Eq. (6), respectively. The electric potential is (see Holroyd&Walker (1987), hereinafter referred to as HW78):

$$\phi_{C,u,d} = \Phi_{u,d} = \frac{3\pi}{16} B_{u,d} \left[z\sqrt{1-z^2} + \arcsin z \right]. \qquad (9)$$

Since $B_u \neq B_d$, from Eq. (9) follows that for any fixed value of $z \neq 0$ there is a difference in the values of potential upstream and downstream. This axial potential difference drives axial electric currents and causes the three-dimensional effects. Plots of F and P are shown in figures 6 and 7, respectively.

The three-dimensional current loops imply higher values of $j_{z,C}$ at z = 0 in the region $-22 \le x \le -2$ and negative values of $j_{z,C}$ (returning current) in the region $-2 \le x \le 10$ (figure 8). Part of the three-dimensional current enters the side region at $q = q_{max}$ for $0 \le x \le 8$.

As follows from their definition above, the development lengths in the upstream and the downstream regions are: $l_{dev,u} = 22$ and $l_{dev,d} = 16.7$, respectively (figure 8). Thus the total development length is $l_{dev} = 38.7$ duct radii, or 19.35 duct diameters.

The development of the core pressure along the duct for q = 0 and for $q = q_{max}$ is shown in figure 9. The values of pressure at these two positions are equal both in the far upstream and the far downstream regions, which means that the flow there is fully developed. The pressure values deviate from each other in the region $-22 \le x \le 16.7$ owing to the three-dimensional effects. At $q = q_{max}$ the pressure monotonically decreases along the flow, while at the duct axis, q = 0, there is a minimum in pressure. There is a partial pressure recovery at q = 0 in the region $-2 \le x \le 10$ owing to the returning current as discussed above. The transverse pressure difference is determined by the axial core current, $j_{x,C}$, which is shown in figure 10.

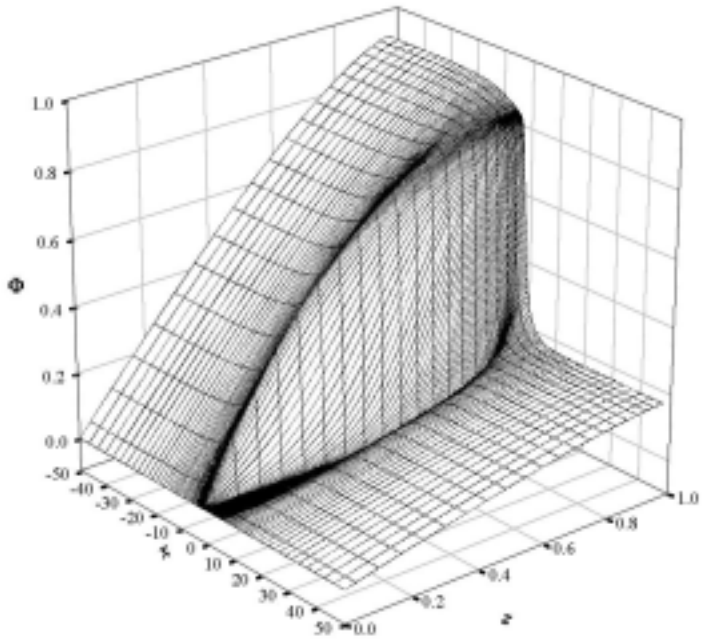

Figure 6. Wall potential Φ for the reference case

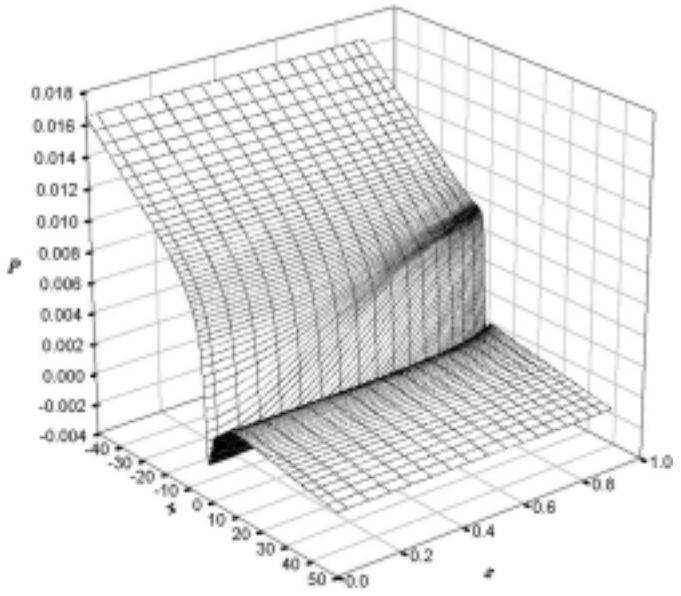

Figure 7. Core pressure P for the reference case

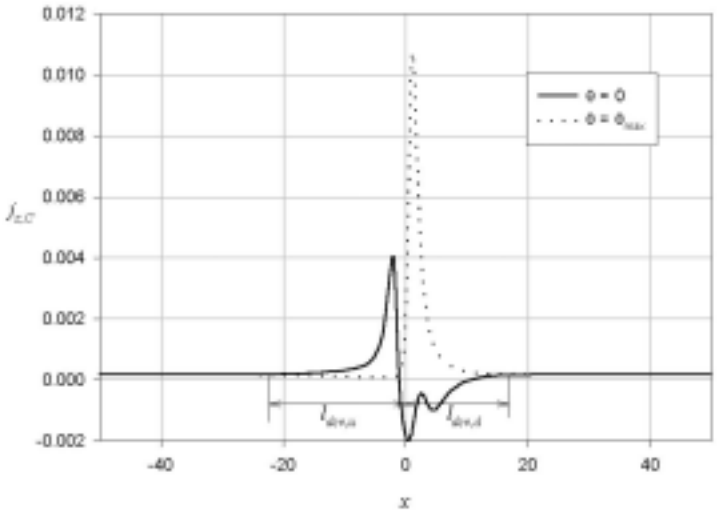

Figure 8. Development of the transverse component of current with x for the reference case and the definition of the development length.

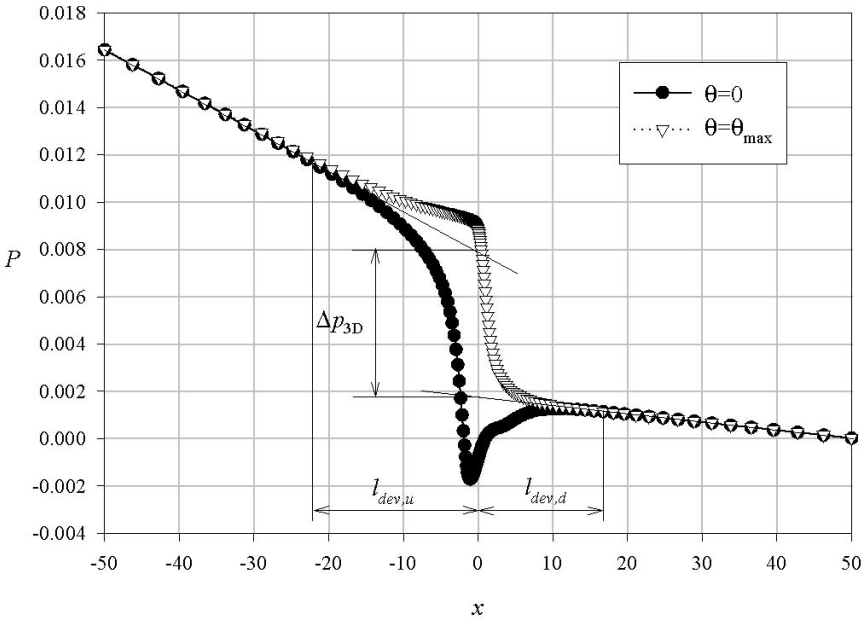

Figure 9. Variation of pressure with x, the three-dimensional pressure drop and the development length for the reference case

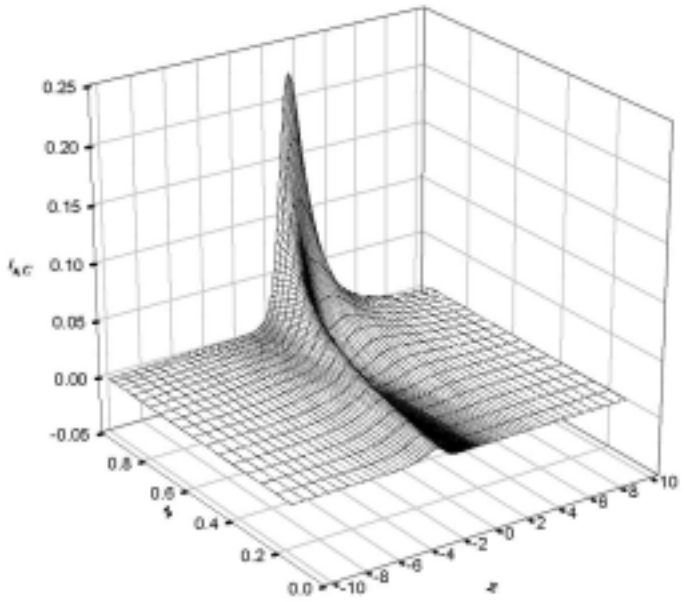

Figure 10. Axial component of current for the reference case

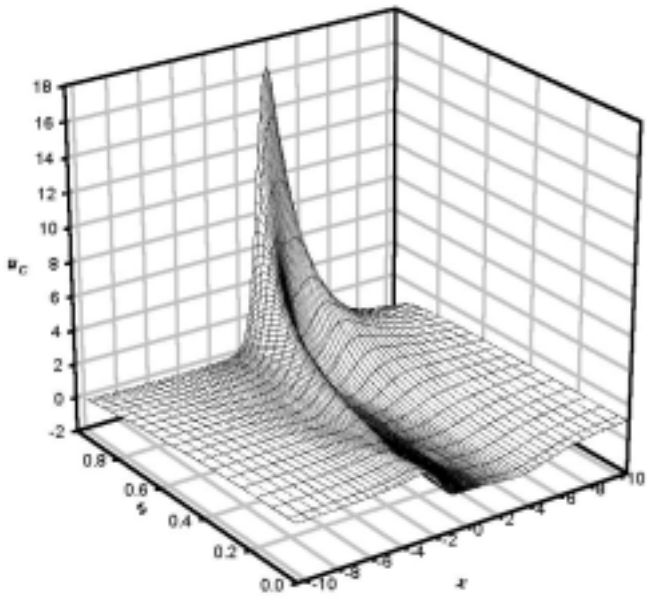

Figure 11. Axial velocity at y = 0 for the reference case

The resulting three-dimensional pressure drop, shown in figure 9, is $\Delta p_{3D} = 6.32 \cdot 10^{-3}$, while the three-dimensional length is $d_{3D} = 37.5$. This is a sufficiently high value, which means that the contribution of the three-dimensional effects to the total pressure drop cannot be neglected.

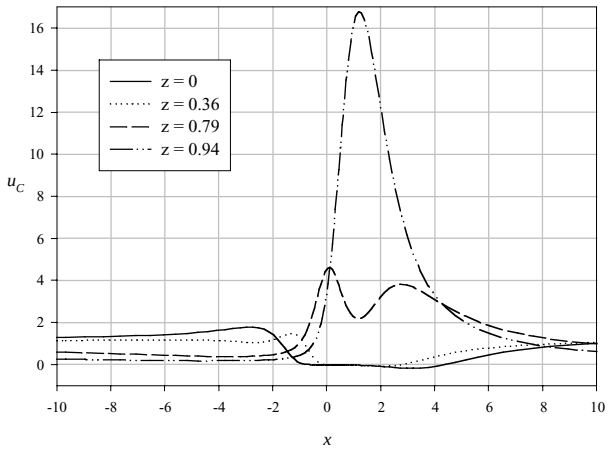

Figure 12. Axial velocity for different values of z for the reference case

The interaction of the magnetic field with the axial current pushes the fluid from the center of the duct to the side in the upstream region, and a peak of axial velocity appears at the side region (figure 11). The development of the axial velocity profiles at y = 0 for several values of z is shown in figure 12, which is similar to figure 7 in HW89. There is a good agreement between our results and those by HW89, both qualitative and quantitative.

Since the fluid is pushed towards the side regions, a stagnant zone develops in the center of the duct for $-1 \leq x \leq 4.5$ (figure 12). There is even a weak reversed flow with velocity minimum of –0.2.

Variation of the Hartmann number, Ha

In this Section we use l_{comp} = 200 in order to account for higher development length at very high Hartmann numbers.

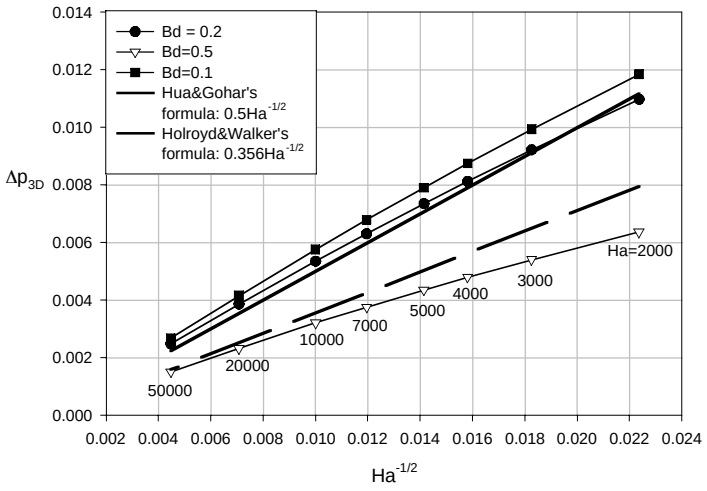

Figure 13. Variation of the three-dimensional pressure drop with Ha for several values of B_d and for γ = 0.8.

The increase in magnitude of the electromagnetic force is reflected in the increase of the Hartmann number. Variation of the three-dimensional pressure drop with Ha is shown in figure 13 for several values of the field level downstream. Also shown in this figure are the results from two analytical expressions. The first one is by HW78:

$$\Delta p_{3D} = 0.356 Ha^{-1/2}, \tag{10}$$

which is a high-Ha asymptotic expression for B_d = 0.5 and for arbitrary g. The second is by Hua&Gohar (1995):

$$\Delta p_{3D} = 0.5 Ha^{-1/2}, \tag{11}$$

and is for "rapidly varying magnetic fields"; no further details were given.

Concerning formula (10), as can be seen from both figure 13, as Ha increases, our numerical solution approaches HW78's formula from below. The coefficient at $Ha^{-1/2}$ tends to 0.356. However, the tendency is slow, so that the difference of coefficients at Ha = 10,000, for example, is about 10%. The reason for the difference is that

Holroyd&Walker obtain the first term in the asymptotic expansion only, while present solution is valid to $O(Ha^{-1})$ (HW89). Nevertheless, the results by HW78 may be taken as good conservative estimates for Δp_{3D}.

Concerning Hua&Gohar's formula, it approximates our results for Δp_{3D} for B_d = 0.2 and g = 0.8, but only for this set of parameters. Also, formula (11) is based on calculated data presented in figure 2 in their paper, which are scattered about the line (11). This might indicate a problem with numerics.

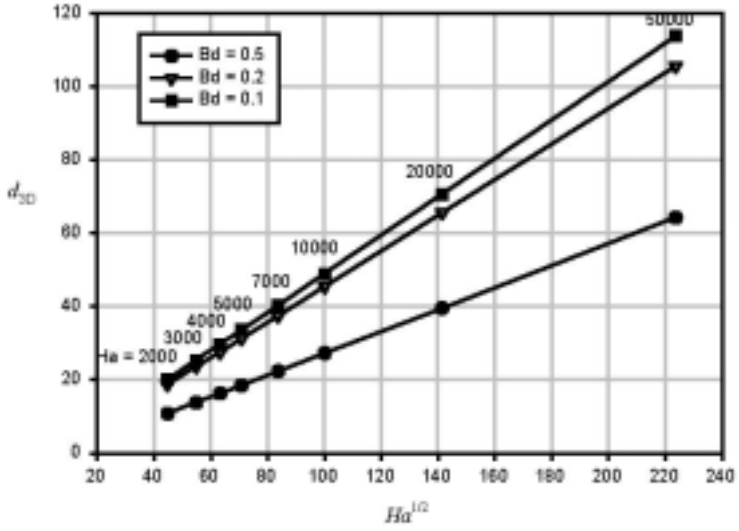

Figure 14. Variation of the three-dimensional length with $Ha^{1/2}$ for several values of B_d and for $\gamma = 0.8$.

Variation of the three-dimensional length, defined by Eq. (8), with the Hartmann number is shown in figure 14. Since Δp_{3D} varies as $Ha^{-1/2}$ for sufficiently high values of Ha, then d_{3D} increases as $Ha^{1/2}$. The three-dimensional length reaches high values even for relatively low values of Ha. This confirms the result that the three-dimensional effects are dominant for insulating ducts of non-rectangular cross-section.

Finally, variation of the development length with $Ha^{1/2}$ is shown in figure 15. There is almost a linear dependence of l_{dev} on this parameter. The development length upstream is higher than downstream and has a higher slope. The total development length reaches a value of about 100 for Ha = 50,000, which is equivalent to 50 duct diameters.

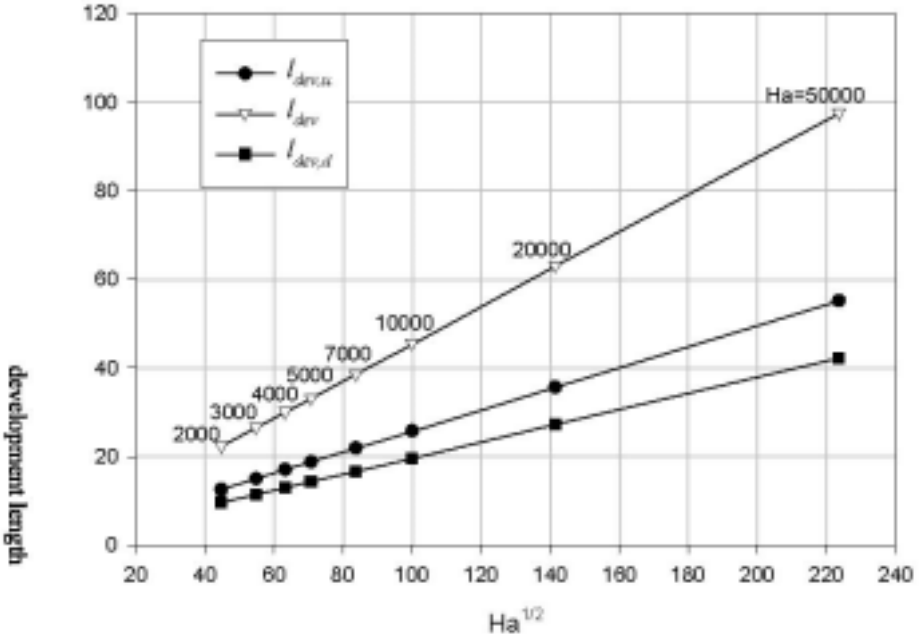

Figure 15. Variation of the development length with $Ha^{1/2}$ for $B_d = 0.2$ and $\gamma = 0.8$.

Variation of the field level, B_d

Decreasing the value of B_d from 1 to 0 increases the magnitude of the three-dimensional effects.

Variation of the three-dimensional pressure drop with the field level in the downstream region is shown in figure 16 for two different values of the Hartmann number. If $B_d = 1$, the flow is fully developed, and $\Delta p_{3D} = 0$. If B_d decreases, three-dimensional effects become more and more important, and the value of Δp_{3D} increases. Although current asymptotic model does not allow for modeling flows with $B_d = 0$, the value of the three-dimensional pressure drop can be extrapolated towards $B_d = 0$. Using this procedure, for example, for Ha = 4000 one gets $\Delta p_{3D}=0.007$, while for Ha = 7000 the result is $\Delta p_{3D}=0.009$. These two values are shown as separate circles in figure 16.

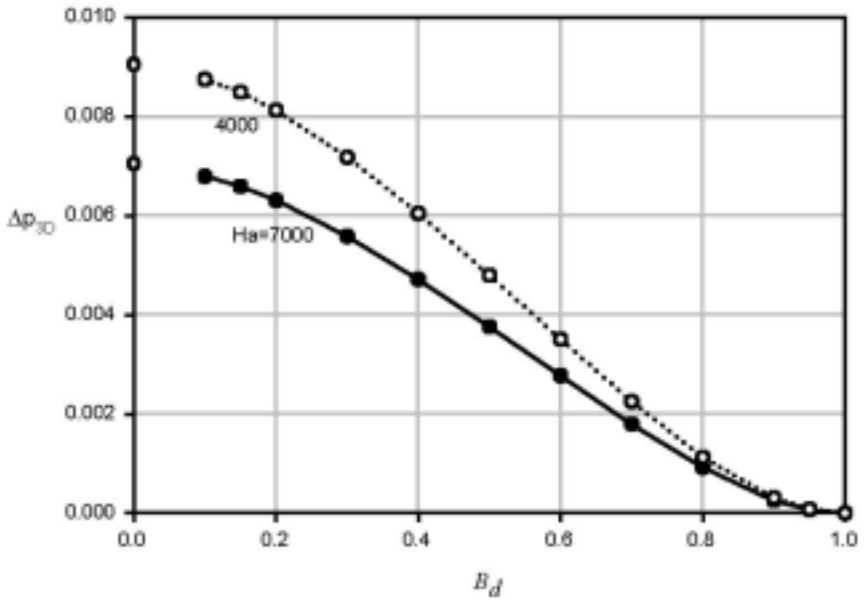

Figure 16. Variation of the three-dimensional pressure drop with B_d for γ = 0.8 and for two values of Ha.

Concerning the three-dimensional length, similar to the three-dimensional pressure drop, it increases monotonically with decreasing B_d.

Variation of the field gradient, g

Variation of Δp_{3D} with the field gradient, g, is shown in figure 17. Overall, the three-dimensional effects become more important with increasing g. There is a strong dependence of the three-dimensional pressure drop on g for fields with weak gradients ($g < 0.5$), and a weak dependence for fields with strong gradients ($g > 1$). Increasing the value of g beyond 2 does not make sense, since for higher field gradients, the second, x-component of the field becomes important. While the current model is not foreseen for such fields, there is no principal problem in extending it to the two-component fields.

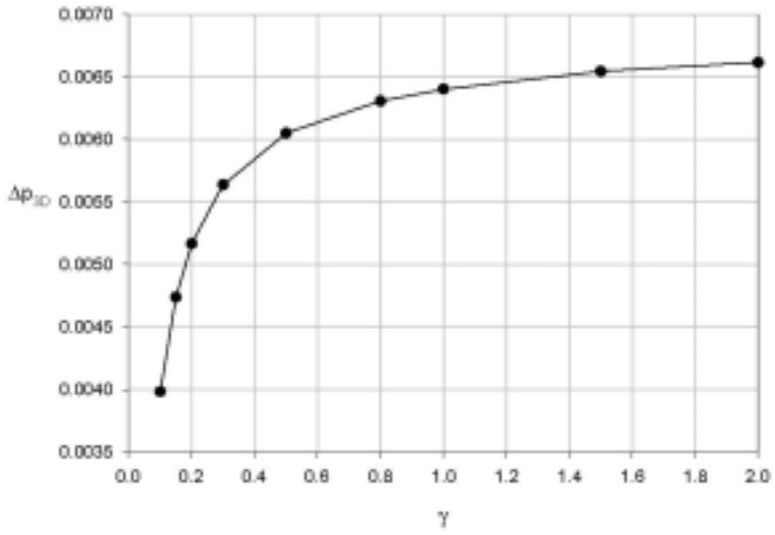

Figure 17. Variation of the three-dimensional pressure drop with γ for B_d = 0.2 and Ha = 7000.

The three-dimensional length increases with increasing g, while the development lengths in both upstream and downstream regions decrease.

As $\gamma \to 0$, the flow tends to become locally fully developed.

The effect of the finite length of the magnet

In laboratory experiments with straight circular insulating ducts the (usually dipole) magnets provide uniform field within a certain finite length. Therefore, real magnetic fields have not a step-function character as shown in figure 5, but rather that shown in figure 18. The second region of the nonuniform magnetic field is produced by the other end of the magnet. Since it has been shown above that the development length in circular insulating ducts may be very high, it is possible that the flow will never be fully developed inside the magnet. This may affect the effects studied experimentally. Thus we address this issue in this Section.

The family of the magnetic fields we adopt for this study is:

$$B = B_{out} + (B_c - B_{out})\frac{\tanh\gamma(x + X_2) - \tanh\gamma(x - X_2)}{2\tanh\gamma X_2}, \qquad (12)$$

where B_{out} is the field level outside the magnet (it is set to 0.2 in the following to ensure validity of the model), B_c is the field level in the center, at x = 0. The field is symmetric about x = 0. The positions $x = \pm X_2$ (shown in figure 18) roughly determine the size of the field region. For a fixed x > 0, as $X_2 \to \infty$ the field determined by expression (12) tends to that given by Eq. (4) with $B_{out} = B_d$ and $B_c = B_u$.

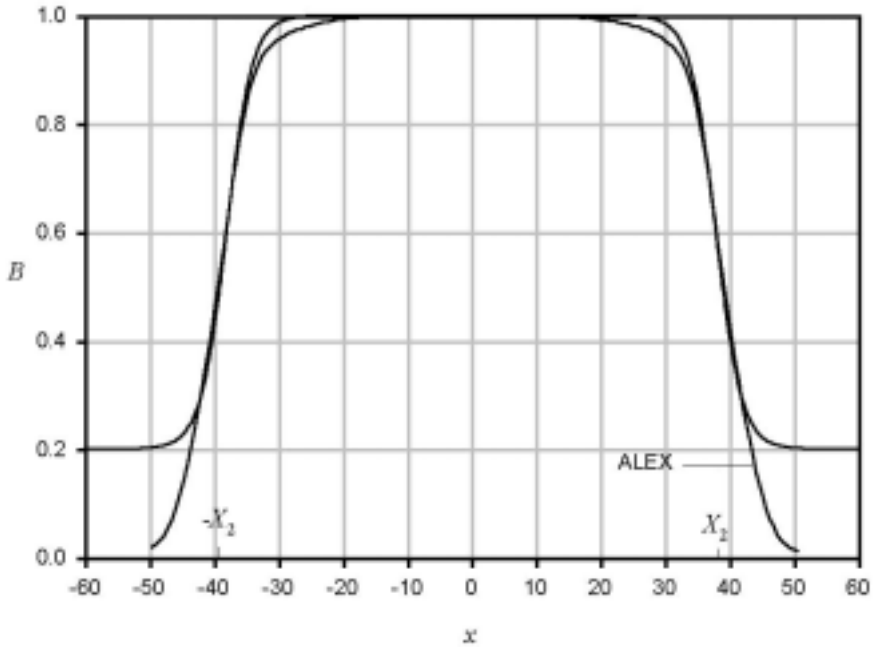

Figure 18. Magnetic field for ALEX (normalized by 2.4cm pipe radius) and that defined by Eq. (12) for $B_c = 1$, $B_{out} = 0.2$, $\gamma = 0.25$, $X_2 = 39$.

Variation of pressure with x for $B_{out} = 1$, $B_c = 0.2$, $X_2 = 15$ and Ha = 7000 is shown in figure 19. It is evident that at the center of the magnet there is a difference in axial pressure gradients at q = 0 and $q = q_{max}$. This indicates that at these parameter values the flow is not fully developed along the whole magnet length. Since the flow is not fully developed, it does not make sense to define a three-dimensional pressure drop between some point at the center of the magnet and some point downstream, as it is done in the experiments and as would be compatible with our previous definition of Dp_{3D}. It would make sense though to define Dp_{3D} between a point far upstream, and a point far downstream of the magnet. This definition, however, would not be compatible with our previous definition of Dp_{3D} as it would incorporate a possible fully developed pressure drop inside the magnet for sufficiently high X_2. Therefore, to quantify the three-dimensional effects we use parameter h defined by Eq. (5) and evaluated at the center of the magnet, i.e. for x = 0, q = 0.

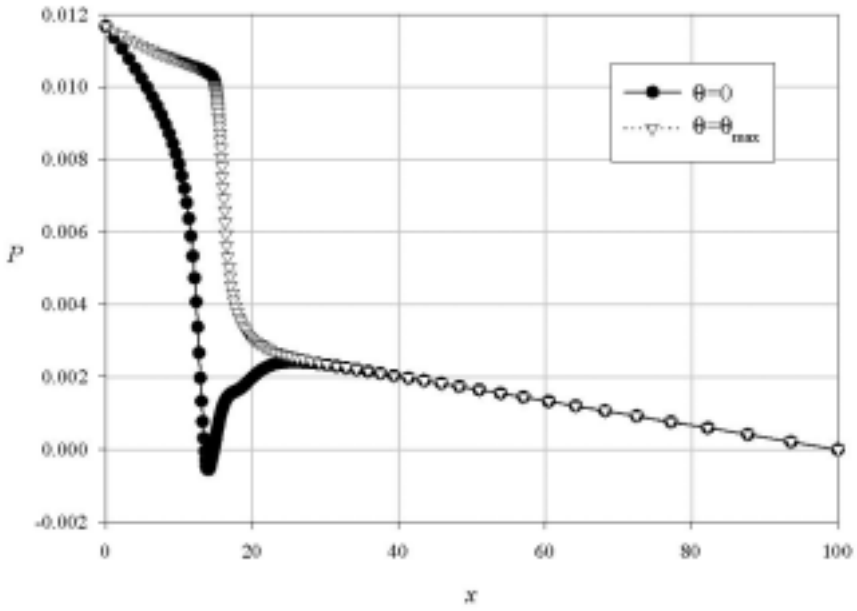

Figure 19. Variation of pressure with x for X_2 = 15, γ = 0.8, Ha = 7000, B_d = 0.2.

Variation of h with X_2 for g = 0.8 and Ha = 7000 is shown in figure 20. Note that the scale of the vertical axis is logarithmic. As could be expected from the results on the development length presented in previous Sections, the length of the magnet needs to be sufficiently high to ensure the fully developed flow in the center.

If one adopts a 10% threshold in h for the flow to be considered fully developed, then one gets $X_2 \approx 41.5$. This is shown in figure 20 by a vertical broken line. This means that the length of the magnet needs to be 41.5 duct diameters. For a duct of 4.8cm diameter (a^* = 2.4 cm) this gives a magnet 2m long. For ALEX facility $X_2 \approx 39$ (if normalized with a^* = 2.4 cm), see figure 22, so that close to the center of the magnet the flow is expected to be fully developed. Since the length of most other magnets is shorter, the fully developed flow condition places (perhaps surprisingly) a restriction on the maximum value of the Hartmann number that can be reached without violating the fully developed flow condition. This in turn implies an upper limit for the field strength for given duct radius and liquid metal.

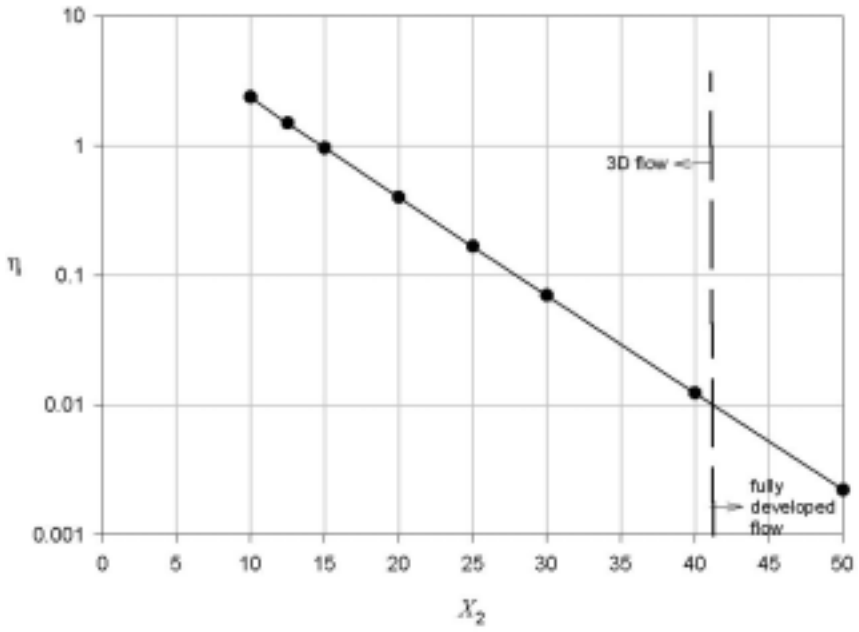

Figure 20. Relative deviation of the transverse current in the center of the magnet from its fully developed value against X_2 for Ha = 7000, $\gamma = 0.8$, $B_d = 0.2$.

1.2.2.6 Conclusions

In magnetohydrodynamic flows in circular insulating ducts in strong nonuniform magnetic fields three-dimensional effects prevail. The three-dimensional pressure drop induced in the inlet/outlet pipes of the blanket may double the total pressure drop if estimated by assuming the pure fully developed flow. However, since the development length in insulating circular ducts is very high, of the order of 100 duct radii, the whole upper part of the blanket needs to be modeled as a single piece. This involves the flow in a bended straight duct in a strong nonuniform field ending with the manifold that feeds an array of coolant ducts. Since our code is very fast, this goal is possible to achieve with current computational facilities.

Concerning the laboratory experiments with insulating circular ducts, care must be exercised even at the planning stage. Clearly defined flow conditions at the center of the magnet, i.e. those of fully developed flow, are necessary in order to decouple the flow at the entrance to and the exit from the magnet. High development length in insulating circular ducts may easily violate these conditions. Therefore, long dipole magnets to perform experiments with high Hartmann numbers are necessary, such as the ALEX facility at ANL.

1.2.3 ARIES benchmark problem

Dai-Kai Sze (2000, private communication) suggested the following benchmark problem which is related to the inlet/outlet pipes for a self-cooled blanket for ARIES.

The benchmark problem

Consider the flow of lithium in an insulating circular duct of 50cm diameter. The flow enters a magnetic field, which varies from zero to 12T within a distance of 50 cm. The flow velocity is 10m/s. Estimate the three-dimensional MHD pressure drop.

We will consider an outlet pipe. The data above give the following values of parameters: $a^* = 0.25m$, $\sigma = 3.34 \cdot 10^6\ (\Omega m)^{-1}$, $\nu = 9 \cdot 10^{-7}\ m^2/s$, $\rho = 500\ kg/m^3$, $v_0^* = 10m/s$, $B_0^* = 12T$. Then the values of the dimensionless parameters are:

$$\text{Ha} = 258{,}457, \quad \text{N} = 24{,}048, \quad B_d = 0, \quad g = 1.5.$$

Since $\text{Ha}^{1/2} = 508$, the inertialess-flow condition (1) is fulfilled, and the model can be applied. For calculations we use m = 40, n = 220, t = 20, $l_{comp} = 400$. We perform two calculations: one for $B_d = 0.2$ and the other for $B_d = 0.1$, and then extrapolate the results towards the case $B_d = 0$. The results are presented in Table 1.

Table 1. Three-dimensional pressure drop, three-dimensional length and development length for several values of B_d for the benchmark problem

B_d	Δp_{3D}	Δp_{3D}^*, MPa	d_{3D}	$l_{dev,u}$	$l_{dev,d}$	l_{dev}
0.2	$1.12 \cdot 10^{-3}$	1.35	245.7	120.41	93.62	214.03
0.1	$1.22 \cdot 10^{-3}$	1.47	267.6	137.63	64.78	202.42
0	$1.32 \cdot 10^{-3}$	1.59	289.6	154.85	35.94	190.79

The results show that the flow in the inlet/outlet pipes for the self-cooled liquid metal blanket for ARIES is dominated by the three-dimensional effects. This is not expected to present a problem, however, because of two reasons. The first reason is that the values of the pressure drop is acceptable. The second is that severe distortions of the velocity profile in this region are not important because it is outside of the active area of the blanket.

1.2.4 Inclination of the field gradient to the duct axis

1.2.4.1 Summary

In the second part (Molokov&Reed (2001b)) of a three-part study the duct is supposed to be straight, while the field gradient is inclined by an angle a to the duct axis. The results are presented for the magnetic field with higher value of B upstream than downstream. In this case the absolute values of the electric potential and the pressure gradient are higher upstream than downstream. As a result of the non-symmetry of the flow, the fluid tends to flow in the regions where both electric potential and the pressure drop sooner. In this region a global maximum of velocity occurs. There is also a local maximum of velocity in the other part of the duct, which is lower by about 10-20% than the global one. Despite the non-symmetry, for $a \leq 45^o$, the flow pattern is similar to that for $a = 0^o$. For higher values of a the region occupied by the nonuniform field grows in the axial direction. As the angle tends to 90^o a very large zone appears, in which the flow is locally fully developed. In this zone the flow is driven by a fully developed pressure gradient for $a = 90^o$. Nevertheless, for $a \neq 90^o$, sufficiently far upstream and downstream there are always semi-infinite zones with the fully developed flow as for $a = 0^o$. The development length in such a flow will be very high. From the practical point of view, however, this situation is purely hypothetical. The reason is that ducts in liquid metal blankets and divertors are expected to be much shorter than the development length in such a flow. No qualitatively new results have been observed by varying the Hartmann number with respect to those reported in Part 1 of the study.

1.2.4.2 Introduction

If changes in the magnetic field occur in the Duct 2 region, far downstream from the bended section, the effect of bending can be neglected. Then the geometry can be approximated by a straight duct. In this study we concentrate on the flow in Duct 2 and place a co-ordinate system (x, y, z) as shown in figure 21. We will be concerned with particular type of magnetic fields that have constant levels, B_u, to the left of Line 1 and B_d to the right of Line 2 (see figure 21). The field is nonuniform between these lines. The flow is assumed to be fully developed both upstream and downstream of the nonuniform field region with different field levels. The gradient of the field is inclined by an angle of a to the axis of Duct 2 in the (x,z)-plane (figure 21).

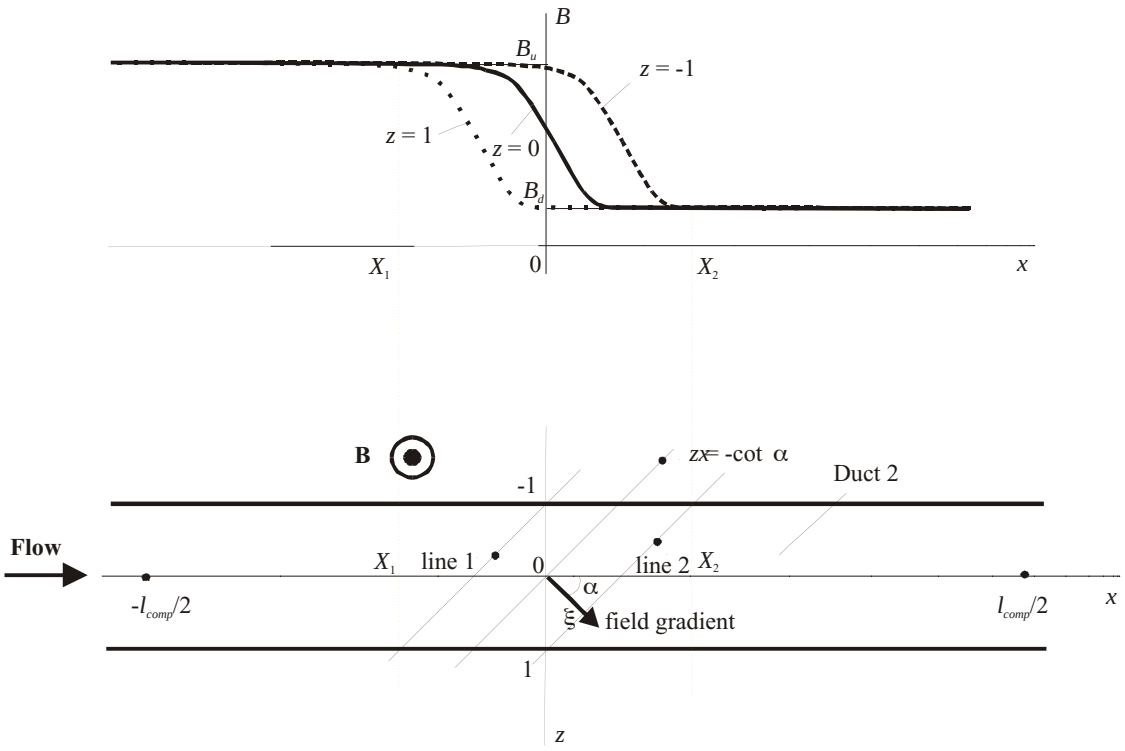

Figure 21. Schematic diagram of the flow in a straight circular duct (Duct 2): (a) nonuniform magnetic field and (b) projection of the duct on the (x,z)-plane

Here we perform a parametric study of the problem with the inclined field gradient to the duct axis, in which we vary the angle a and the Hartmann number Ha.

Consider a steady, three-dimensional flow of a viscous, electrically conducting, incompressible fluid in a straight, insulating, circular duct in the x-direction (figures 2 and 21). A strong, nonuniform, transverse magnetic field

$$B(\xi) = \frac{1}{2}(B_d + B_u) + \frac{1}{2}(B_d - B_u)\tanh\gamma\xi \qquad (13)$$

is applied, where $\xi = \cos\alpha x + \sin\alpha z$. The field induction varies between the constant values of $B_u = 1$ and B_d ($0 \le B_d \le 1$; flow out of the intense-field region), its levels upstream and downstream, respectively. The field varies along straight lines inclined by an angle of a to the x-axis as shown in figure 21. The co-ordinate x measures the distance along these lines. For $a = 0^o$ one gets x = x, thus the field gradient is aligned with the duct axis. For $a = 90^o$ one gets x = z, i.e. the field does not vary along the flow, so the flow is fully developed. This situation is singular in a sense since the fully developed pressure gradient is different from that for $a \neq 90^o$.

1.2.4.3 Results

Reference case

The following values of parameters define the reference case: a = 45°, Ha = 7000, g = .8, B_d = 0.2. For calculations we use l_{comp} = 200. The results of calculations are shown in Figs. 22-29.

Far upstream and far downstream the flow is fully developed. It is driven by the pressure gradients given by the expressions (6). The electric potential both far upstream and far downstream is independent of a. It may be approximated (to O(1)) by the expression (9). Since $B_u \neq B_d$, from Eq. (9) follows that for any fixed value of $z \neq 0$ there is a difference in the values of potential upstream and downstream. This axial potential difference drives axial electric currents and causes the three-dimensional effects. Plots of F and P are shown in figures 22 and 23, respectively. Both functions F and P are not symmetric with respect to z.

The three-dimensional current loops imply higher values of $j_{z,C}$ at z = 0 in the region $-22 \leq x \leq -2$ and negative values of $j_{z,C}$ (returning current) in the region $-2 \leq x \leq 12$ (figure 24). Peak of transverse current is higher at $q = q_{max}$ than at $q = -q_{max}$. Part of the three-dimensional current enters the side region at $q = q_{max}$ for $-4 \leq x \leq 10$ and leaves the side region at $q = -q_{max}$ for $-2 \leq x \leq 10$.

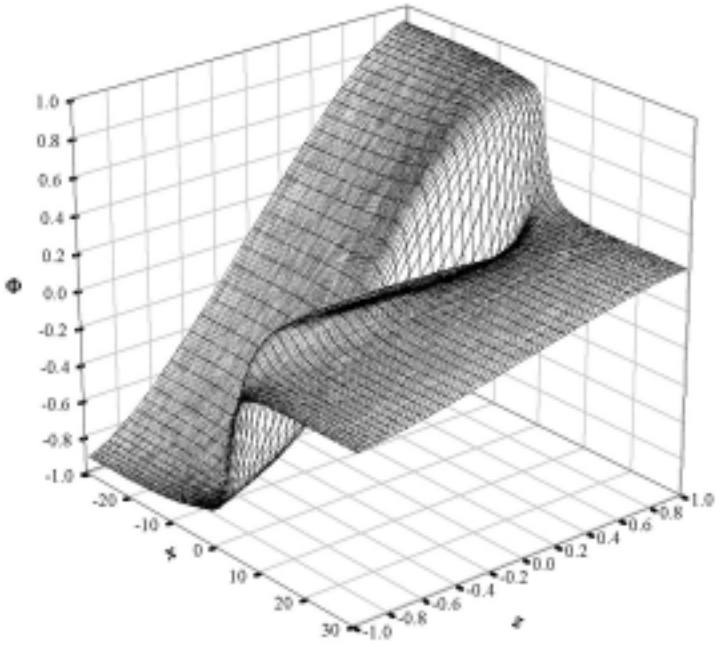

Figure 22. Wall potential Φ for the reference case

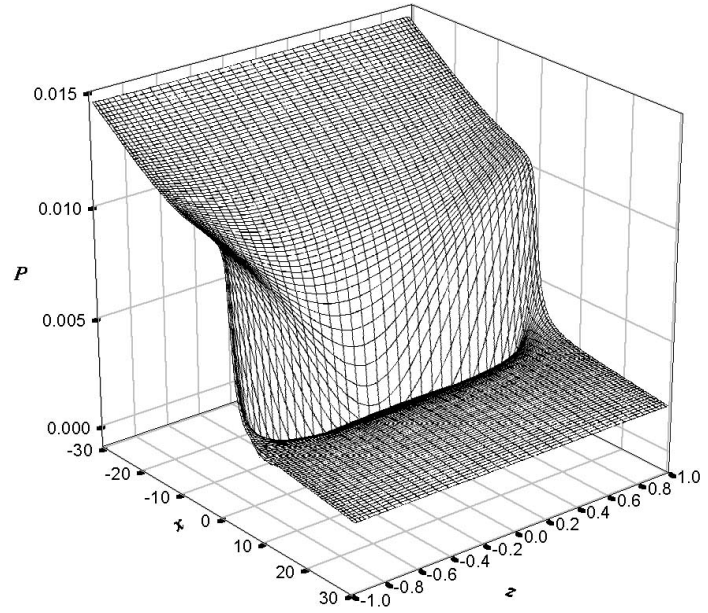

Figure 23. Core pressure P for the reference case

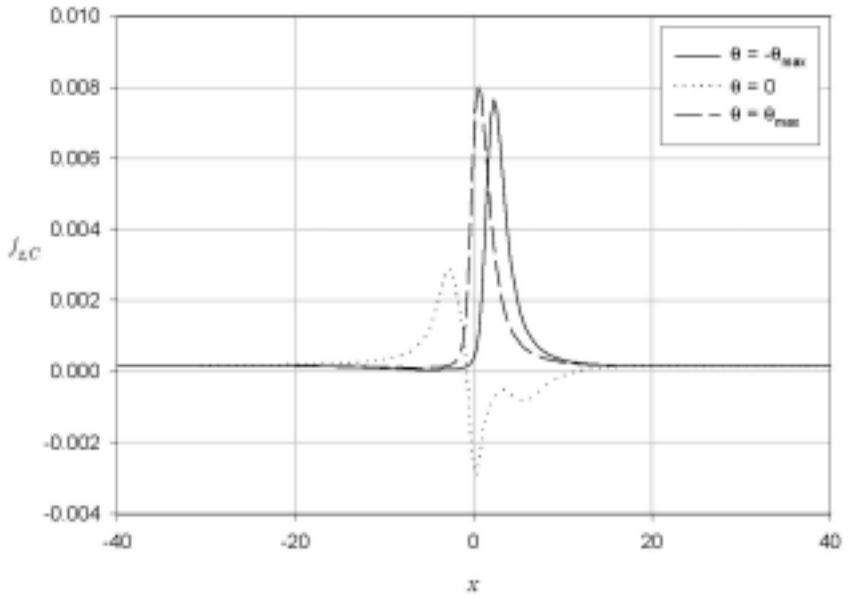

Figure 24. Development of the transverse component of current with x for the reference case.

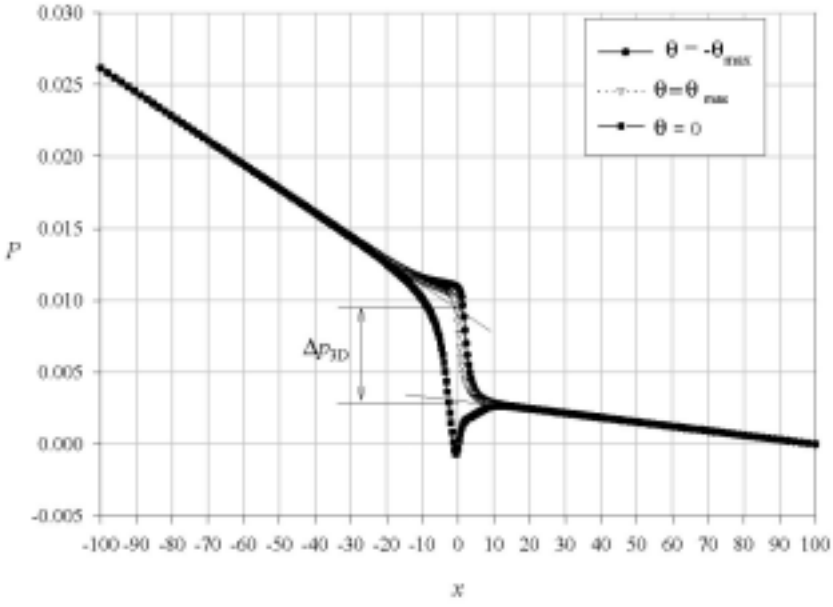

Figure 25. Variation of pressure with x and the three-dimensional pressure drop for the reference case.

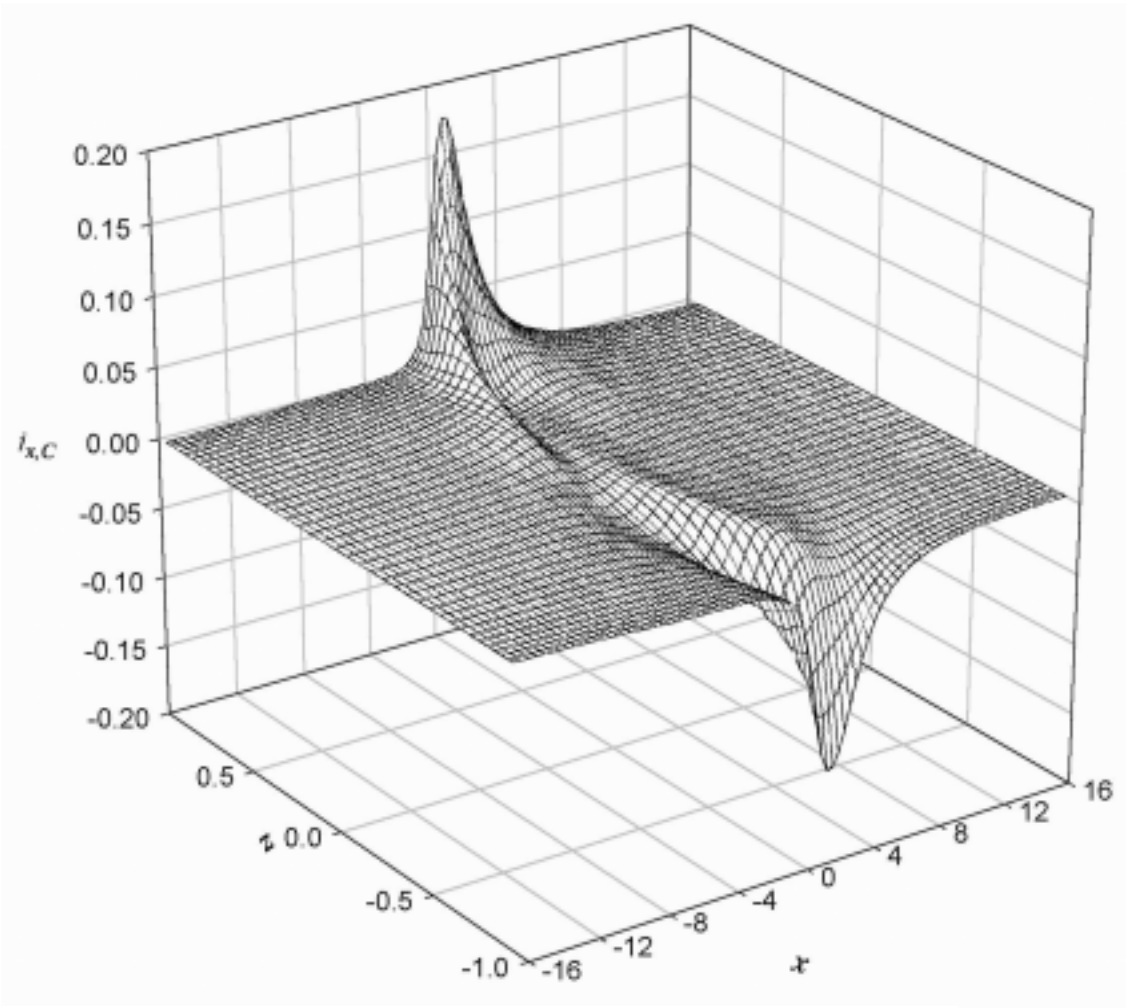

Figure 26. Axial component of current for the reference case

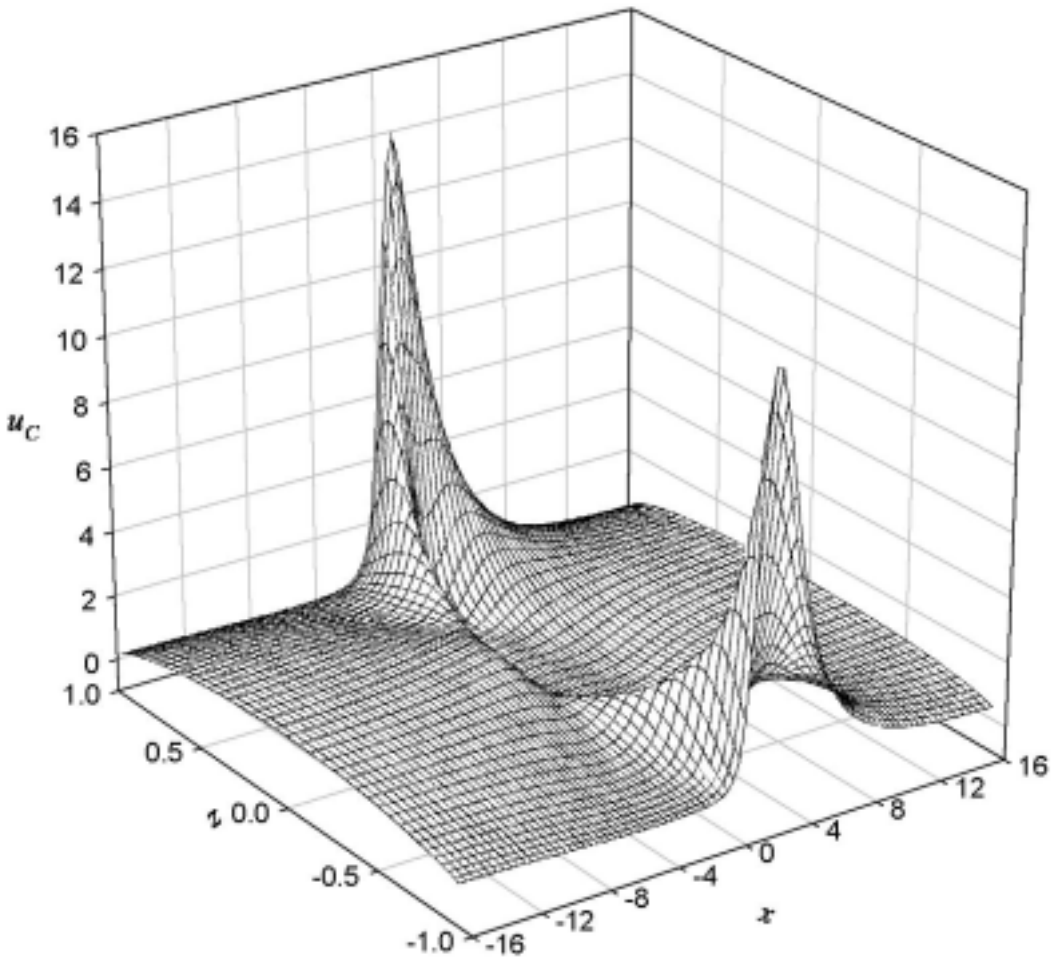

Figure 27. Axial component of velocity for the reference case

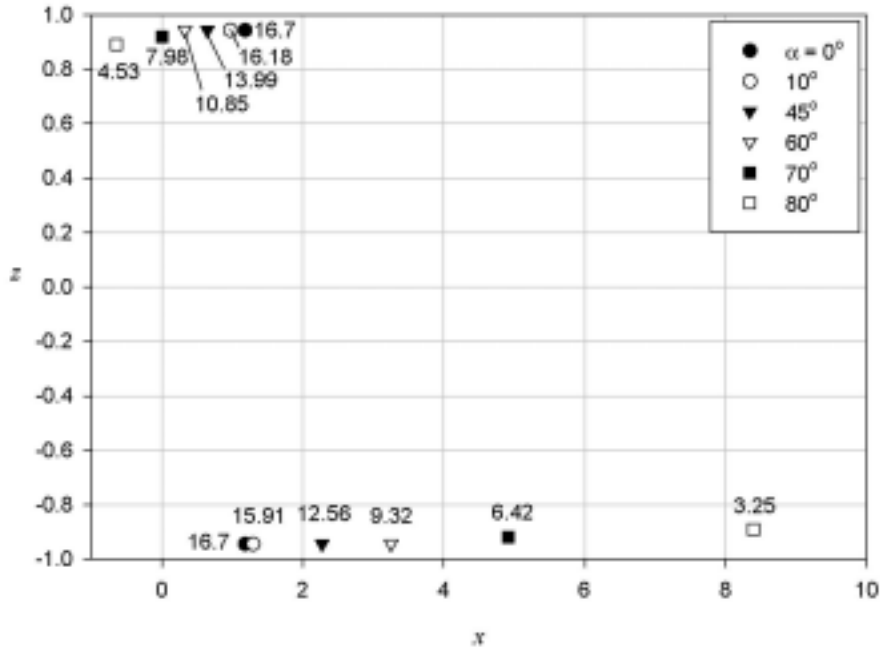

Figure 28. Positions of maxima of axial component of velocity for z > 0 and z < 0 and for different values of α. Here Ha = 7000, B_d = 0.2, γ = 0.8.

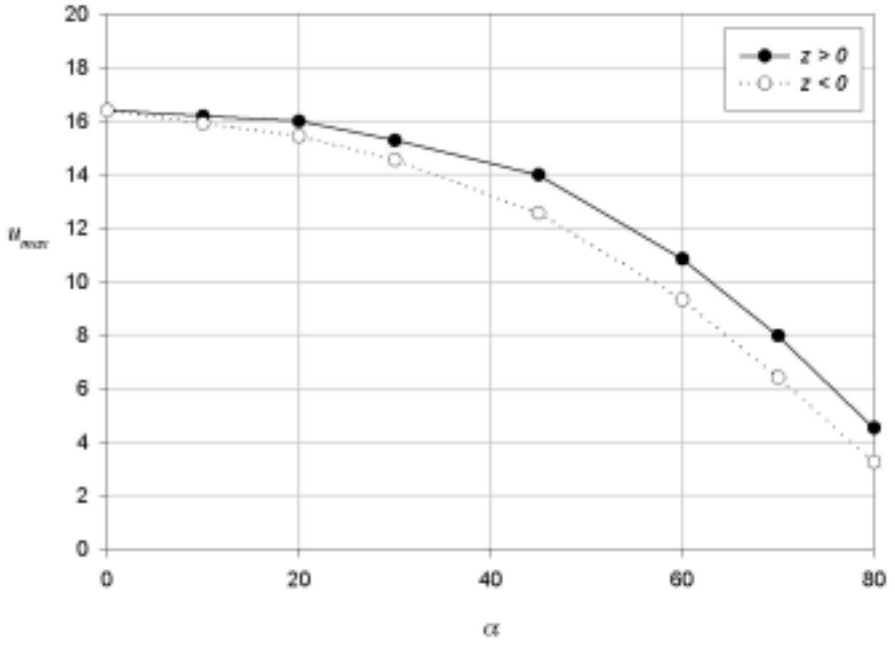

Figure 29. Variation of u_{max} with α for B_d = 0.2, γ = 0.8 and Ha = 7000.

Pressure at $z \approx 1$ (or $q = q_{max}$) drops sooner than that at $z \approx -1$ (or $q = -q_{max}$) as is seen in figure 25. This is because for a fixed x the magnetic field at z = 1 is lower. The values of pressure at $q = \pm q_{max}$ and at q = 0 are equal both in the far upstream and the far downstream regions, which means that the flow there is fully developed. The pressure values deviate from each other in the region $-25 \le x \le 13$ owing to the three-dimensional effects. At $q = \pm q_{max}$ the pressure monotonically decreases along the flow, while at the duct axis, q = 0, there is a minimum in pressure. There is a partial pressure recovery at q = 0 in the region $-2 \le x \le 10$ owing to the returning current as discussed above. The transverse pressure difference is determined by the axial core current, $j_{x,C}$, which is shown in figure 26.

The resulting three-dimensional pressure drop, shown in figure 25, is $\Delta p_{3D} = 6.25 \cdot 10^{-3}$, which is only slightly lower than the value $6.32 \cdot 10^{-3}$ for $a = 0^o$, while the three-dimensional length is $d_{3D} = 37$.

The interaction of the magnetic field with the axial current pushes the fluid from the center of the duct to the sides in the upstream region, and peaks of axial velocity appear at the side regions (figure 27). The peaks of velocity are not equal, the higher value of 13.99 being reached at $q=q_{max}$ and a lower value of 12.56 being reached at $q = -q_{max}$ (see figures 28 and 29). The reason for this asymmetry is that since the field induction drops faster at $q = q_{max}$, more fluid tends to flow in this region than at $q = -q_{max}$. It should be noted that both velocity peaks are lower than the value of 16.7 for $a = 0^o$.

Since the characteristic surfaces block the flow in the duct center, and the fluid is pushed towards the side regions, a zone of recirculating flow develops in the center of the duct at z = 0. There is a reversed flow with velocity minimum of –0.444, which is lower than the value of –0.2 for $a = 0^o$.

Although the flow is non-symmetric for $a = 45^o$, most of the flow features are the same as those for $a = 0^o$. Similarly to the flow for $a = 0^o$ the development length is $O(Ha^{1/2})$.

Variation of the angle a

Variation of velocity maxima and Δp_{3D} with a are shown in figs. 28-30. As the value of a increases, the axial distance occupied by the nonuniform magnetic field grows. However, as the gradient of the field becomes more and more transverse to the flow, three-dimensional distortions of the flow become less severe. For a close to the value of 90^o, the gradient of the field is almost transverse to the flow, while the fluid flows almost parallel to the lines B = constant. The region occupied by the nonuniform magnetic field is very large in the axial direction, but the flow there is locally fully developed.

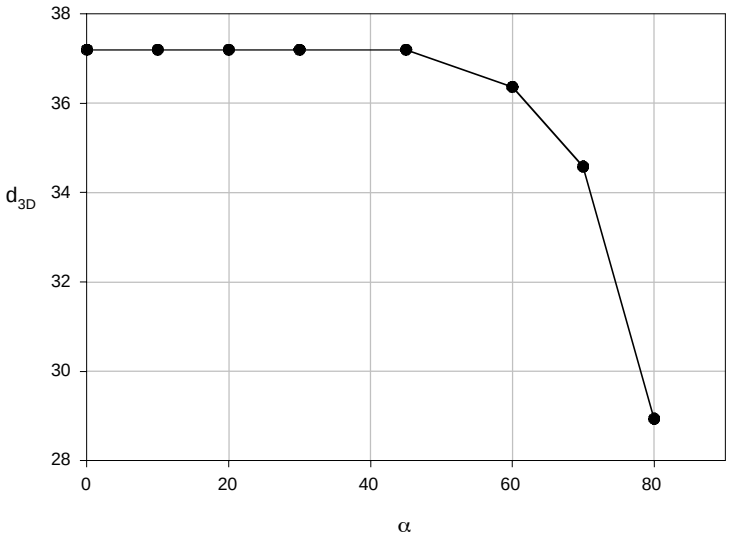

Figure 30. Variation of the three-dimensional length with α for B_d =0.2, Ha = 7000 and γ = 0.8.

Variation of the three-dimensional pressure with a is shown in figure 30. The three-dimensional pressure drop decreases with increasing a. However, it remains almost constant for a ≤ 45^o.

Variation of velocity maxima with a are shown in figures 28 and 29. As a increases, velocity maxima for both z > 0 and z < 0 decrease. The velocity maximum for z > 0 is always higher than the corresponding value for z < 0 owing to the reasons discussed above. For a given a the velocity maxima for z > 0 and z < 0 are shifted upstream and downstream from their positions for a = 0^o, respectively, and away from the wall.

Similar to the three-dimensional pressure drop, velocity maxima vary very slowly with a for a ≤ 45^o. This means that the flow for a ≤ 45^o retains the same properties as that for a = 0^o, while for higher values of a is tends to become locally fully developed.

1.2.4.4 Conclusions

The flow for a $\neq 0^o$ lacks symmetry with respect to the z-axis, which contrasts with the flow for a=0^o discussed in Part 1. As a result of the non-symmetry, the fluid tends to flow in the regions where both the electric potential and the pressure drop sooner. For a particular type of magnetic fields considered here this occurs at z = 1. As a result, a global maximum of velocity occurs at z = 1. Nevertheless, there is a local maximum of velocity at z = -1, which is lower than that for z = 1 by 10-20%.

Despite the non-symmetry, for a $\leq 45^o$, the flow pattern is similar to that for a = 0^o. For higher values of a the region occupied by the nonuniform field grows in the axial direction. As the angle tends to 90^o a very large zone appears, in which the flow is locally fully developed and in which the flow is driven by a fully developed pressure gradient for a = 90^o. Nevertheless, for a $\neq 90^o$, sufficiently far upstream and downstream there are always semi-infinite zones with the fully developed flow as for a = 0^o. The development length in such a flow will be very high. From the practical point of view, however, this situation is purely hypothetical, even if Duct 2, shown in figure 1, is almost perpendicular to Duct 1. The reason is that ducts in liquid metal blankets and divertors are expected to be much shorter than the development length in such a flow.

Variation of the Hartmann number reveals no new effects with respect to those discussed in the above and those obtained in Part 1.

References for Section 1

Bucenieks, I., Lielausis, O., Platacis, E., Shishko, A., 1994 Experimental study of liquid metal film and jet flows in a strong magnetic field, Magnetohydrodynamics, **30**(2), 219-230.

Debray, F., Joss W., and Mossang E. 2000 The Grenoble High Magnetic Field Laboratory opportunities for MHD Experiments, proceedings of Pamir 4th International Conference on MHD, Presqu'ile de Giens – France; September 18-22, 2000, pg. 757-62.

Holroyd, R. and Walker, J.S. 1978 A theoretical study of the effects of wall conductivity, non-uniform magnetic fields and variable-area ducts on liquid metal flows at high Hartmann number, J. Fluid Mech., **84**, 471-495.

Hua, T.Q. and Walker, J.S. 1989 Three-dimensional MHD flow in insulating circular ducts in non-uniform transverse magnetic fields, Int. J. Engng Sci., **27**, 1079-1091.

Hua, T.Q. and Gohar, Y. 1995 MHD pressure drops and thermal hydraulic analysis for the ITER breeding blanket design, Fusion Engineering and Design, **27**, 696-702.

Karasev, B.G., Tananaev, A.V. 1990 Liquid metal fusion reactor systems, Plasma devices and operations, **1**, 11-30.

Mattas et al 2000 ALPS – advanced limiter-divertor plasma-facing systems, Fusion Engineering and Design, **49-50**, 127-134.

Molokov, S. 2000 Spreading liquid drop in a strong magnetic field, proceedings of Pamir 4th International Conference on MHD, Presqu'ile de Giens – France; September 18-22, 2000, pg. 1.

Molokov, S., Cox, I., Reed, C.B. 2001 Theoretical investigation of liquid metal MHD free surface flows for ALPS, Fusion Technology, **39**, 2. Pt. 2, 880-884.

Molokov, S., Reed, C.B. 2000a Review of free-surface MHD experiments and modeling, Argonne National Laboratory Report, ANL/TD/TM99-08

Molokov, S., Reed, C.B. 2000b Fully developed magnetohydrodynamic flow in a rivulet, Argonne National Laboratory Report, ANL/TD/TM00-12, also presented 20th IUTAM; Chi., IL; Aug 27 - Sep 2, 2000.

Molokov, S., Reed, C.B. 2000c Liquid metal free surface flows in fusion, proceedings of Pamir 4th International Conference on MHD, Presqu'ile de Giens – France; September 18-22, 2000, pp. 303-08.

Molokov, S., Reed, C.B. 2000d Recent Results On MHD Jet Divertor Modeling, Argonne National Laboratory, Presented at ALPS/Modeling Meeting, November 13, 2000.

Molokov, S., Reed, C.B. 2001a Liquid metal flow in an insulated circular duct in a strong nonuniform magnetic field. Part 1: Straight duct and the benchmark problem, Argonne National Laboratory Report, ANL/TD/TM01-18.

Molokov, S., Reed, C.B. 2001b Liquid metal flow in an insulated circular duct in a strong nonuniform magnetic field. Part 2: Inclination of the field gradient to the duct axis, Argonne National Laboratory Report, ANL/TD/TM01-19.

Molokov, S., Reed, C.B. 2001c Liquid metal flow in an insulated circular duct in a strong nonuniform magnetic field. Part 3: Flow in a bend, Argonne National Laboratory Report, ANL/TD/TM01-20.

Reed, C.B., Natesan, K., Hua, T.Q., Kirillov, I.R., Vitkovski, I.V., Anisimov, A.M. 1995 Experimental and theoretical MHD performance of a round pipe with an NaK-compatible Al_2O_3 coating, Fusion Engineering and Design, **27**, 614-626.

Reed, C.B., Molokov, S. 2001 Proposed MHD Experiments on Liquid Metal Jets at GHMFL, **Presented at GHMFL, Grenoble France, July 5, 2001**

Tannehill, J.C., Anderson, D.A. and Pletcher, R.H. 1997 Computational Fluid Mechanics and Heat Transfer. (Taylor&Francis: Washington, Bristol, London).

2. Liquid Metal IR Temperature Measurements

Tina J. Tanaka, Thomas J. Lutz, Jimmie M. McDonald, Kenneth P. Troncosa, and Michael A. Ulrickson, Sandia National Laboratories

2.1 Summary

This report describes the tests and results of infrared temperature measurements of liquid metals performed to date. The emissivity of a material must be known to derive the temperature of a surface optically. Optical temperature measurements of the surface of a liquid metal have two major sources of error: (1) low emissive metals produce low signals that can be swamped out by reflected radiation of more emissive objects, and (2) surface contamination causes increased emissivity that can be interpreted as higher temperature. For all optical measurements of temperature, the transmission of the window and optics should be well known, because the optical losses will decrease the signal and therefore the inferred temperature. If data on emissivity are not available directly, the emissivity can be calculated from optical constants and electrical properties if these are available in the literature. In the absence of emissivity data, we have made preliminary experimental determinations and compared these with the emissivity calculated from properties in the literature. The results suggest that the calibration of our optics is still incomplete.

2.2 Introduction

Thermal properties of liquid metals are not known to high enough temperature to evaluate their usefulness for fusion applications. Sandia National Laboratories plans to heat the surface of flowing liquid metals by striking the surface with an energetic electron beam and study the thermal properties of the flowing liquid metal by measuring the temperature profile of the surface. The temperature rise during heating for flowing Li is expected to be 350 °C and for Ga and Sn, over 1000 °C. Temperature measurements through optical methods are required to obtain the surface temperature distributions without disturbing the surface flow. For such measurements the materials' emissivities and IR transmission factors must be known to determine the temperature profiles accurately.

Emissivity is the ratio of the power emitted from a body to that emitted by a black body at the same temperature. The spectral distribution of a gray body is the same as for a black body at the same temperature, but the gray body has a fraction of the emitted power of the black body, that fraction being the emissivity. Pure liquid metals are very conductive; most visible and infrared wavelengths are reflected from the surface because conduction electrons move freely to cancel electromagnetic fields in liquid metal. Only a small amount of incident radiation is absorbed and none is transmitted unless the liquid metal is very thin. By Kirkoff's law of radiation, the emissivity and absorbed fractions are equivalent.[1] Thus, the emissivity, ε, of liquid metals can be calculated from optical constants obtained from reflectivity measurements ($\varepsilon = 1 - r$), where r is the reflectivity.

Three types of information published in the literature can be used to obtain the emissivity: direct measurements of emissivity, optical constants, and electrical constants. Limited emissivity measurements are available in the literature on only a small number of

molten metals.[2] Havstad[3,4] has carefully measured the emissivity of molten Al and U directly and also by various optical techniques. The emissivity can be calculated from other measured optical constants such as the index of refraction or a complex dielectric constant. These constants are available for metals such as Sn[5-8] and Ga[9-11], but not for Li. A third literature-based method of calculation is to use other electrical properties, such as the electrical resistivity and Hall coefficient, to determine the optical constants and the emissivity[12] while assuming the free-electron nature of the liquid metal. These electrical properties are reported for molten Li[13] as well as Ga[14-19].

2.3 Experimental Procedure

The goal in the IR temperature experiments was to melt metals proposed for use as fusion reactor blankets, such as Li, Ga, Sn, and Sn-25at%Li alloy (SnLi), and measure their apparent emissivities. In our preparatory work reported here, our specific objectives are (1) calibration of our instruments, (2) identification of issues important in future use of our infrared equipment, and (3) development of useful techniques to analyze the temperature of flowing liquid metal. Measuring the temperature of low emissivity materials such as liquid metals is not straightforward. Sources of error are the reflection of other radiation sources besides the emission of the liquid metal, surface contamination, and unknown values for window transmission. So far, we have measured the apparent emissivity of Li and Ga, and we continue work on Sn; we use the same infrared instruments that will be used in the future for measurements of the temperature profiles.

The metals were melted in a crucible as a static pool and their emissivities were measured with infrared instruments that sampled wavelengths between 2 to 5.3μm. In each test, the temperature of the crucible was measured during the infrared measurements, so that the temperature measured by the pyrometers and cameras could be compared to the actual crucible temperature. Fig. 2.1 shows the vacuum chamber with the mounted cameras and pyrometers.

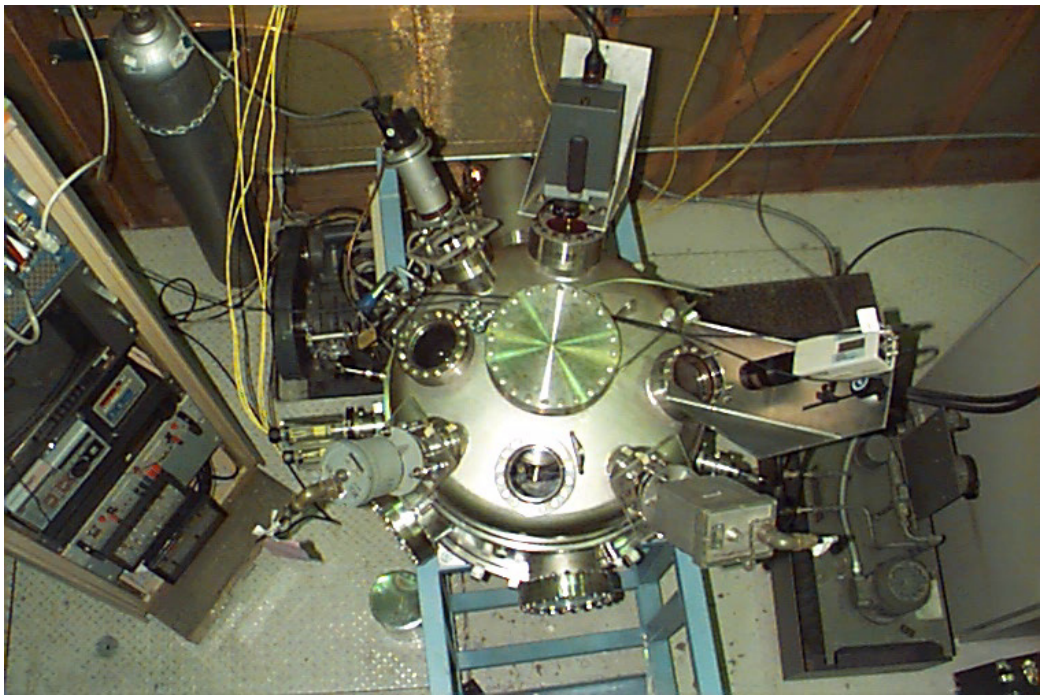

Figure 2.1. Vacuum chamber with mounted pyrometers and cameras.

Fig. 2.2 is a schematic drawing of the various pyrometers, the windows and the crucible. The resistively heated crucible was well insulated from the rest of the vacuum chamber so that it would cool slowly. Using a small diameter blind hole in the crucible as a gray body, we monitored the effect on the observed temperature of the deposition of evaporated metals onto the vacuum windows.

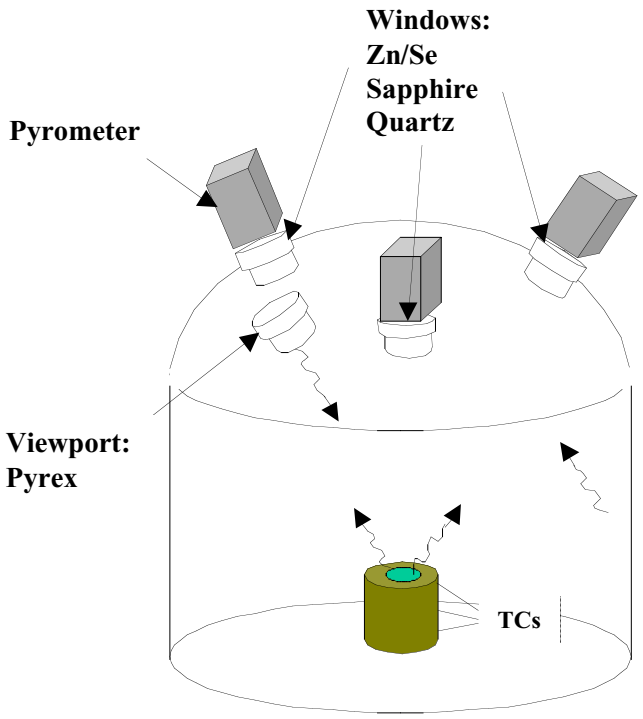

Figure 2.2. Schematic view of cameras and crucible on vacuum chamber.

Fig. 2.3 shows the crucible filled with Li. For most experiments, the crucible was heated to 400°C, and then the power to the heater was turned off and the liquid metal was allowed to cool and solidify. In the case of Ga, supercooling to 8°C below the melting point was encountered and the liquid was seeded with pieces of solid Ga to start solidification. Table 6.1 lists the instruments used in measuring temperature in the experiment.

Liquid metals are highly reflective and reflection of radiation from other sources can be a problem, especially at lower temperatures when the liquid metal signal is low. This reflected radiation, added to the radiation emitted from the liquid metal surface, results in a higher temperature measured by optical instruments.

On our vacuum chamber the ports are arranged symmetrically around the top of the chamber. A pyrometer could view the reflection, on the surface of the liquid metal, of light passing through a port on the opposite side of the top of the chamber. The tendency of the liquid metal to form a curved mirror due to surface tension exacerbates this problem. To reduce this error, all ports were covered to shield out laboratory light.

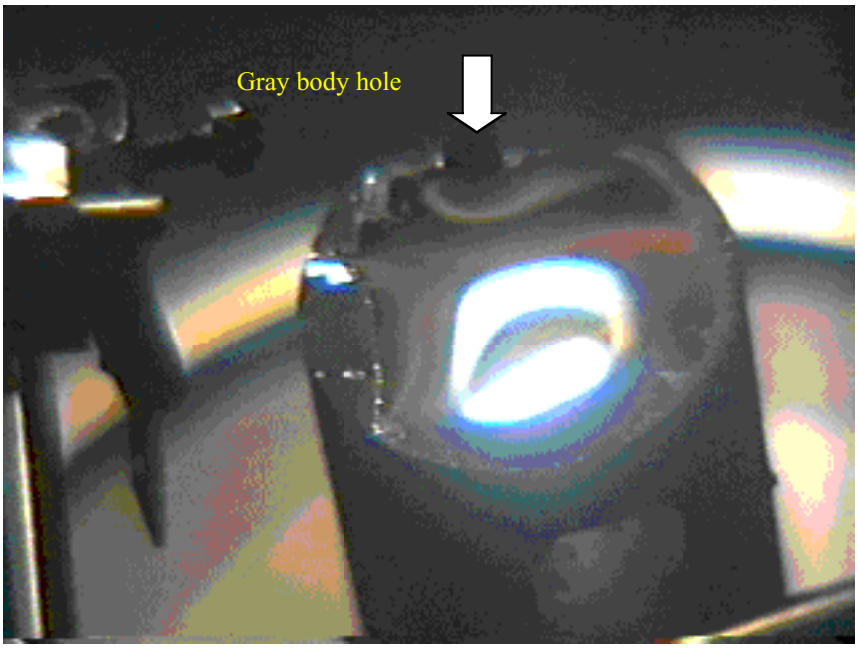

Figure 2.3. Crucible with molten Li and gray body hole.

Table 2.1. Temperature measuring instruments used in experiment.

Instrument	*Temp. (°C)*	*Wavelength (μm)*	*Emissivity*	*Windows*
Low range Pyrometer (IRCON series 6000)	70–220	2–2.6	0.001 – 0.999	Sapphire
Mid-range Pyrometer (Land)	130–550	2.05–2.55	0.1 – 1.0	ZnSe and WF Quartz
High range Pyrometer (IRCON series 7000)	300–1300	4.8–5.3	0.1 – 1.0	ZnSe and Sapphire
Infrared camera (Inframetrics)	25–500+	2-14 with narrow 3.9μm filter	1.0	ZnSe and NaCl, later, LW Quartz
Thermocouple (Type K)	0–1000	N/A	N/A	N/A

Another source of error with liquid metals is surface contamination. Emissivity is highly dependent on the condition of the surface. Surface contamination occurs because the

metals like lithium, gallium, and tin easily combine with gases such as oxygen and nitrogen. These compounds have higher melting temperature and lower conductivity than the liquid metal. As mentioned earlier, the reflectivity of liquid metals is high because of the highly conductive surface. Low conductivity impurities on the surface of the metal lead to a less reflective (more emissive) surface that in turn produces an observed temperature that is erroneously high. To reduce this error, the crucibles were filled so that the meniscus extended over the top and the surface of the metal was scraped with a flat stainless steel or molybdenum blade.

Vacuum windows reduce the signal received by the pyrometers due to losses from reflection at interfaces and from transmission through the window. The windows used for each pyrometer or camera are listed in Table 2.1. ZnSe is included because its reduced x-ray transmission is necessary for future electron beam experiments. Water free or low water (LW) quartz windows are used to shield the delicate ZnSe windows from metal vapor deposition. Using two windows leads to a significant signal reduction due to reflection (≈60%.) The low-range pyrometer had only a sapphire window since its temperature range is too low to be used in future electron beam tests with flowing Li.

In our early tests on Li, scraping of the initial dull and obviously contaminated surface left a visually bright and reflective surface that was easily maintained for several hours at a vacuum level of 5×10^{-7} Torr. Preliminary tests showed that lithium coated the windows of the vacuum chamber after the temperature of the crucible was maintained at 380°C for 3–4 hours. The coating was primarily on the upper windows and obscured the pyrometers and cameras, all mounted above the crucible. This coating seriously degraded the optical signals, and we concluded that future measurements should be performed with a shorter heating period or shutters to protect the windows.

In later tests on Ga, the scraping left a bright and reflective surface. However, it was obvious in deforming the surface (with the scraper) that a thin reflective coating had formed on the surface. This deformation of the surface produced a pattern of tiny cracks in this coating that confirmed its existence and produced a crazed surface with a significantly higher emissivity.

Thermal measurements on the Ga with the pyrometers were compared to thermocouples on the crucible for the following conditions:

1) Ga under vacuum and vacuum windows in place,
2) with argon flowing into the vacuum chamber at approximately atmospheric pressure and the vacuum windows in place, and
3) with argon flowing without vacuum windows.

The pyrometers and camera measure the power radiated at the wavelength ranges given in Table 2.1. The pyrometers and IR camera each have an emissivity setting that can be set at some (single) value to account for the emissivity of the material being viewed. We record data from the IR camera with the emissivity set to 1.0. Typically, we also capture separate "snapshots" electronically and make emissivities corrections via software during the tests.) Although the emissivity of the low-range pyrometer could have been set to match the temperature reading of the crucible in real time, this apparent emissivity would

include the losses from the window. Instead, the pyrometers were set to an emissivity of 0.1 because that was deemed best for recording and analysis.

The emissivity of liquid metals can be calculated from the electrical properties of the Hall coefficient and resistivity.[12] These electrical properties can be used with the Drude model of metals[20] to estimate the density of free electrons and the damping constant for electron motion. Both Hall coefficient and resistivity are dependent on temperature and data were found for both Ga[16,18] and Li[13].

2.4 Results

This section discusses the data gathered thus far on the IR temperature measurements. Some of the information has been presented in earlier news notes, meetings, and electronic conferences. Lithium was the first material melted and it was reported on at pervious e-meetings as shown in Fig. 2.4. The emissivity of the lithium reported previously was too low because the transmission of the windows was not measured at the time. Also we did not cover all ports so we could have signal on pyrometers from reflection of laboratory lights into the pyrometers. During these measurements we found that a shorter wavelength band was useful for controlling the reflection of cool surfaces from the liquid metal surface. As a result, the IR camera is now being used with its narrow-band 3.9μm filter.

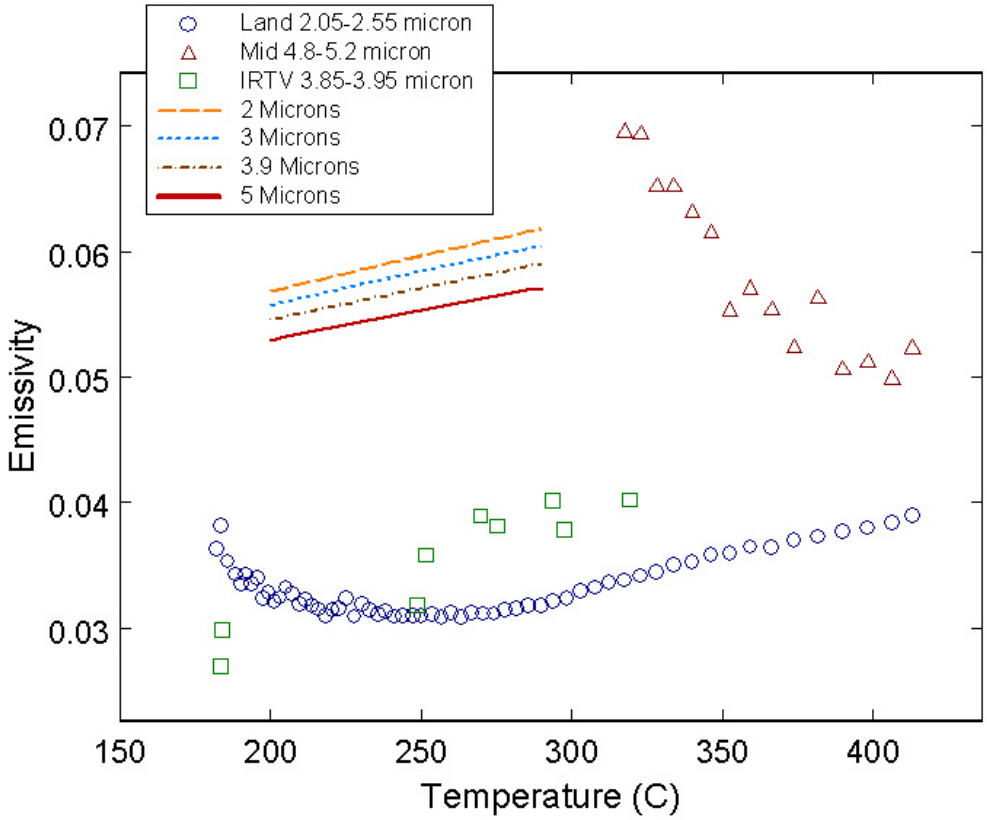

The emissivity of SnLi was never determined. We had problems obtaining a clean surface because solid compounds formed that floated on the surface of the liquid. Discussion of our attempts at this measurement is covered in the section of this report on the SnLi melting experiment.

Ga is less hazardous than Li because its melting temperature is lower and it is more inert. Because of its lower melting temperature, we used the low-range (70-220°C) pyrometer to determine the emissivity of the material first hand. We also experimented with the window transmission by making measurements with an argon cover gas with and without windows between the material and the pyrometer.

Fig. 2.5 shows the temperature from the Land pyrometer (emissivity setting at 0.1) versus the thermocouple temperature for Ga measured with no windows and an Ar cover gas. Despite using ultra high purity Ar as the cover gas, the molten Ga developed a slight film and needed to be scraped intermittently.

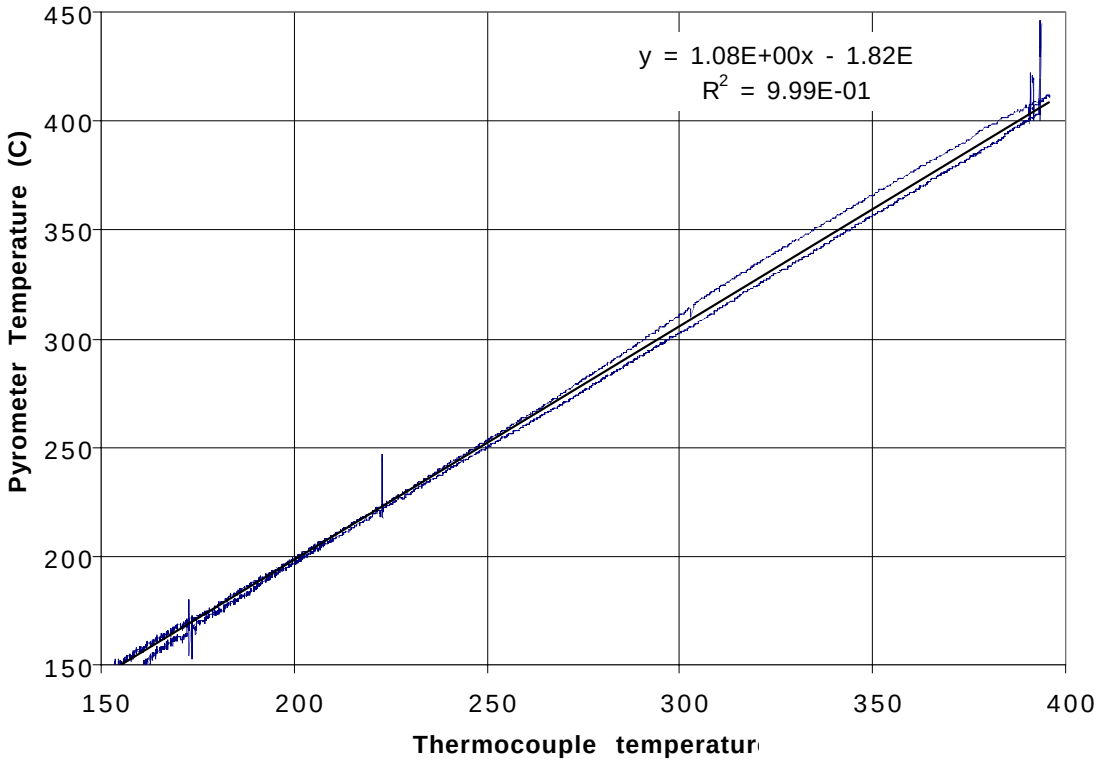

Figure 2.5. Temperature of Ga measured with pyrometer compared to temperature measured by thermocouple in the crucible.

Table 2.2 shows linear fits for the output of the Land pyrometer versus the temperature of the thermocouple (in the crucible) under different conditions. All of the linear fits are good as indicated by the high R^2 values. The vacuum windows lower the measured temperature and change the slope of the linear fit from 1.080 to an average of 0.92.

Table 2.2. Temperature Equations for Ga, Land Pyrometer (ε=0.1) measurements as a function of the thermocouple output

Conditions	Equation for T_p(C)	R^2
Windows and vacuum	0.93 T(C) + 1.48	0.9974
Windows and Argon flow	0.93 T(C) –12.92	0.9996
Argon flow	1.09 T(C) –20.41	0.9901

The results in Table 2.2 were analyzed to determine the transmission of the argon, windows, and emissivity of Ga. We used the method suggested by IRCON[21,22] and available on their website (www.ircon.com). The symbols are listed in Table 6.3.

$$T_{IND} - T_{TRUE} = -100 \times \frac{\varepsilon_{DIAL} - \varepsilon_{TRUE}\tau_W}{\varepsilon_{TRUE}\tau_W} \times \Delta T_{TABLE}$$

Table 2.3. Definitions for temperature correction equation

Symbol	Definition
T_{IND}	Temperature indicated by pyrometer
T_{TRUE}	Thermocouple temperature
$\_T_{TABLE}$	Temperature change for 1% change in emissivity table in papers [21,22]
ε_{DIAL}	Emissivity setting
ε_{TRUE}	True emissivity of liquid metal
τ_W	Window or argon transmission

The tabulated ΔT values vary with temperature and effective wavelength of the pyrometer. The correction for the Land pyrometer (λ=2.3 μm) is 0.73°C for a 1% shift in emissivity and for the Series 7000 pyrometer (λ=5 μm), the correction is 1.6°C at 400°C. Errors in emissivity are more significant for the temperature measurement of pyrometers that have longer effective wavelengths. The transmission losses are treated as a multiplier for the emissivity. Some representative transmission factors and emissivities are listed in Table 2.4 below.

Table 2.4. Calculated transmission and emissivity from data in Table 2.2.

Calculated value	200 °C	300 °C	400 °C
τ_{argon}	0.77	0.83	0.87
τ_{window}	0.61	0.53	0.50
ε_{Ga}	0.12	0.14	0.16

In Table 2.4 our calculated values of the transmission factors through argon and the vacuum chamber windows depend on temperature for the following reason. The

pyrometer integrates the signal transmission times Planck's distribution over the pyrometer wavelength band. Higher temperatures shift Planck's distribution to shorter wavelengths. (The decrease in emissivity with increasing wavelength can be seen in the calculated values for emissivity for λ equal to 2.3, 3.9 and 5μm in Fig. 3.6) The window transmission factors also vary rapidly through the wavelength band seen by the Land pyrometer. The overall effect of integrating over this band is to derive transmission factors that vary with temperature. While this result does not give single wave length transmission factors for the materials in question, the effective transmission factors derived are the ones needed for the measurement techniques that we use.

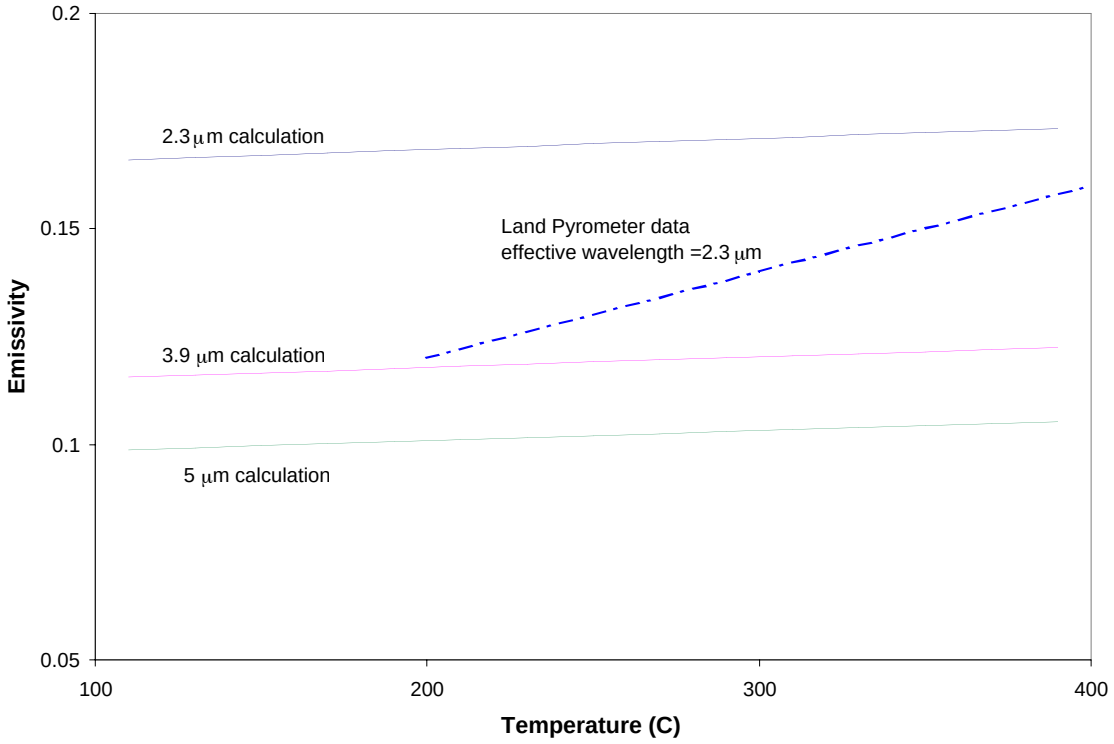

Figure 2.6. Comparison of Ga apparent emissivity with emissivity calculated from the Hall coefficient and resistivity.

Fig. 2.6 shows the comparison of the corrected Ga emissivity measured with argon cover gas vs. a calculation from Hall coefficients and resistivity. Even though the apparent emissivity is low compared to the calculated, the intent of these calibrations is to provide corrections for these instruments. The comparison to the theoretical emissivity is used as a check on the validity of the measurements and corrections and the applicability of the instruments to the materials and conditions of interest. These corrections to instrument readings for window transmission and emissivity for similar conditions should yield fairly accurate temperatures in the flowing liquid experiments.

We also performed experiments in which tin shot was melted in a stainless steel crucible. The oxides were difficult to remove and a persistent thin film was found on the tin. More work on tin and lithium are needed.

2.5 Conclusions

Commercial instruments can measure liquid metal temperatures if proper precautions are made in the experimental techniques and appropriate corrections are made to the data. Because liquid metals have such low emissivity, we need to: control background infrared radiation (reflections of other sources), determine and correct for transmission factors for windows, gases and vapors, and control or account for contamination of liquid metal. Short wavelength bands are preferred for this work because it reduces the contribution of radiation from cool, high-emissivity surface reflections.

Further work should be done on lithium and on tin if we are likely to use it in our pumping system. The window transmission corrections need to be carefully measured using a blackbody source and then applied to the case for lithium.

2.6 References

1. Frank Kreith, *Principals of Heat Transfer*, Third edition, Chapter 5-Heat transfer by radiation, Intext Educational Publishers, New York, NY, 1976, p232
2. K. Schaefers, M. Rösner-Kuhn, M. Frohberg, Concentration dependence of the spectral emissivity of liquid binary metallic alloys, International Journal of Thermophysics, Vol 16, No 4 (1995) p997.
3. M. A. Havstad, The Radiative Properties and Optical Constants of Liquid Metals, Lawrence Livermore National Laboratory, UCRL-LR—107524, DE91 016874, June 1991
4. M. A. Havstad, W. McLean II, S. A Self, Measurements of the thermal radiative Properties of Liquid Uranium, Journal of Heat Transfer, vol. 114 (1993) p1013
5. M. Brückner, J.H. Schäfer, C. Schiffer, and J. Uhlenbusch, Measurements of the optical constants of solid and molten gold and tin at lambda=10.6 mu-m, J. Appl. Phys. Vol. 70, No. 3, 1 August 1991, p1642-7
6. E. T. Arakawa, T. Inagaki, M. W. Williams, Optical properties of metals by spectroscopic ellipsometry, Surface Science, Vol. 97 (1980) p248-274.
7. J. P. Petrakian, A. R. Cathers, J. E. Parks, R. A. MacRae, T. A. Callcott, E. T. Arakawa, Optical properties of liquid tin between 0.62 and 3.5 eV, Phys. Rev. B, Vol. 21, No. 8, 15 April 1980, p3043-6
8. I. A. Shaikevich, P. I. Drozd, L. V. Poperenko, N. V. Sopinskii, Ellipsometric investigation of oxidation processes of tin in solid and liquid states, Opt. Spectrosc. (USSR) Vol 53. No. 1, July 1982
9. N. R. Comins, The optical properties of liquid metals, Phil. Mag., vol. 25 (1972) p817
10. R. Sh. Teshev and A. A. Shebzukhov, Electronic characteristics and dispersion of optical constants of liquid gallium in the 0.4-2.5 μm spectral region, Opt. Spectrosc. (USSR) vol. 65, No. 5, November 1988, p693-695
11. L. A. Akashev and V. I Kononenko, Optical properties of liquid gallium-indium alloy, Technical Physics, vol. 43, no. 7, July 1998, p853-4

12. M. A. Havstad and T. Qui, Prediction of Liquid Metal Alloy Radiant Properties from Measurements of the Hall Coefficient and the direct Current Resistivity, Lawrence Livermore National Laboratory Preprint UCRL-JC-L-18866-1, National Heat Conference, Portland Oregon, August 5-9, 1995
13. H.-J. Güntherodt, H.U. Künzi, R. Müller, R. Evans, Hall Coefficient and Electrical resistivity of liquid lithium, Physics Letters, Vol. 54A, no 2, 25 August 1975
14. M. Ogita, T. Fujinami, Y. Nakanishi, Y. Hatanaka, Surface reflection and nonlinearities in AC Hall measurements of liquid metals, Applied Surface Science, Vol. 113/114 (1997) p777-782
15. G. Ginter, J. G. Gasser, R. Kleim, The electrical resistivity of liquid bismuth, gallium and bismuth-gallium alloys, Philosophical Mag. B, vol. 54, no. 6 (1986) p543-552
16. A. J. Crispin and R. V. Aldridge, The Hall effect in liquid mercury-gallium alloys, J. Phys F: Met. Phys. Vol. 16 (1986) p1753-1760
17. M. Ogita and T. Fujinami, Perplexities related to Hall measurements in the liquid state, Bull. Res. Inst. Electron. Shizuoka Univ. Japan, vol. 30, no. 3 (1995) p241-4
18. J. Yahia and J. P. Thobe, The temperature dependence of the resistivity of liquid gallium to 1000º C, Canadian Journal of Physics, Vol. 50 (1972) p2554-2556
19. A. J. Crispin, Hall effect frequency spectra obtained from the Corbino method, J. Phys E, Sci. Instrumentation , Vol. 21 (1988) p271-274
20. M. Born and E. Wolf, *Principals of Optics*, Chapter 13, Optics of Metals, Pergamon Press, Oxford, 1975 (Fifth Edition)
21. IRCON, Inc., “Temperature Errors Caused by Change in Product Emissivity”, Technical Solutions, TS100
22. IRCON, Inc., “Temperature Errors Due to Transmission Losses”, Technical Solutions, TS101

3. Experiments on Sn-0.25 Li

T. J. Tanaka, T. J. Lutz, J. M. McDonald, R. E. Nygren, K. P. Troncosa, R. Bastasz and M. Clift, Sandia National Laboratories

Experiments on the melting Sn-25% by atom Li, were started in an effort to measure the emissivity of this alloy. As SNL worked with this material and gained experience, we found that the material formed a high temperature crust and thus we have discarded it as a material that we could possibly use in our liquid metal integrated test system, LIMITS. The alloy does not remain uniformly mixed and forms compounds that solidify below 700ºC. Presented here is a summary of SNL results on Sn-25a%Li (SnLi). Fig. 3.1 shows a phase diagram of the Sn-Li system.[1]

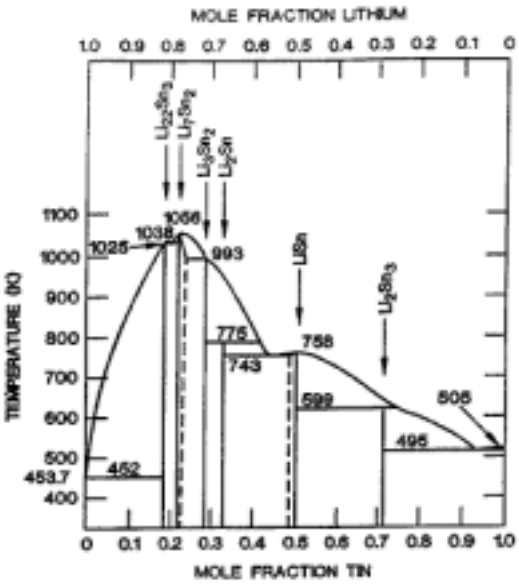

Fig. 3.1 Phase diagram of Li-Sn system

3.1 Melting of SnLi

SNL attempted to mix SnLi by melting Sn shot in a stainless steel crucible and then adding Li by dipping a piece of Li foil into the molten Sn. Initially there was little reaction with the solid Li foil. But as the foil began to melt, a stong exothermic reaction was observed thatspilled material out of the crucible, as shown in Figure 3.2. In the last frame of Fig. 3.2 the temperature of the crucible was about 700ºC. We assume that the reaction might be due to compound formation or simply the mixing itself. As the Li melted, a reaction zone would have formed adjacent to the Li/Sn interface with rapid diffusion of Li and Sn producing composition gradients in the Li-rich side and in the Sn-rich side. The Li-rich side of the phase diagram (Fig. 3.1) shows several intermetallic compounds ($Li_{22}Sn_3$, Li_7Sn_2, Li_3Sn_2 and Li_2Sn) as well as Li_2Sn_3 on the Sn-rich side. The literature indicates the mixing itself is strongly exothermic and this has been observed by Natesan (ANL) in slowly introducing Li in small amounts into Sn[1] and by Bastasz (SNL) in melting layered foils of Sn and Li and by ourselves.

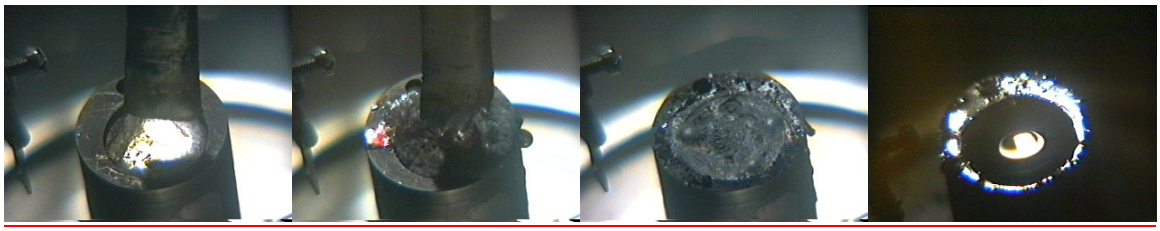

Figure 3.2. Sequence of frames taken during the melting of Li into Sn.

After encountering difficulty in trying to mix our own SnLi, we abandoned the idea of melting the two materials together in the crucible, and instead requested some SnLi alloy

from Ken Natesan of ANL. In subsuquent test, we melted material from Natesan in a 316L SS crucible that was quickly heated to about 400 °C. The melt started to bubble and within 2 minutes had bubbled out of the crucible. Figure 3.3 shows some stills taken from the video of the bubbling material as it melts and spills out of the crucible. We presumed that this material was well mixed and hypothesized that the material was either reacting to the SS crucible, as expected by Sharafat and Ghoniem[2], or outgassing as it melted.

Figure 3.3. Video sequences from melting Natesan sample in SS crucible.

The material ejected from the SS crucible was analyzed by Auger spectroscopy and X-ray analysis in a scanning electron microscope(SEM). We also analyzed the gases in a subsequent melting experiment in which we melted SnLi. In this case the SS crucible was protected with a Boron Nitride(BN)-liner. All materials from these melts were viewed in the SEM and analyzed by energy dispersive spectra.

3.2 Analysis of SnLi

Figure 3.4 shows a scanning electron micrograph of material that was ejected from the SS crucible prior to analysis in the Auger spectrometer. Area 1, located in the center of the image, was examined first. Area 2 is a smoother region that was examined in depth.

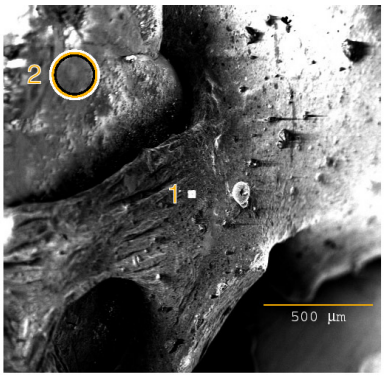

Figure 3.4 (right). SEM picture of SnLi sample that was ejected from SS crucible.

Figure 3.5 shows the Auger analysis of the surface at area 1. Li but not Sn was observed on the surface. The large oxygen content is typical for an air-exposed Li-containing sample. Some C and a very small amount of Cl were detected on the surface. The atomic composition of the surface, estimated from Auger signal sensitivity factors, is: 48%(at.) O, 47% Li, 5% C, <1% Cl. In area 2, some material was removed from the surface and more Auger analysis was performed. The results of probing the depths of the sample are shown in Figure 3.5. More Sn and less Li appears as the sample is taken deeper into the material.

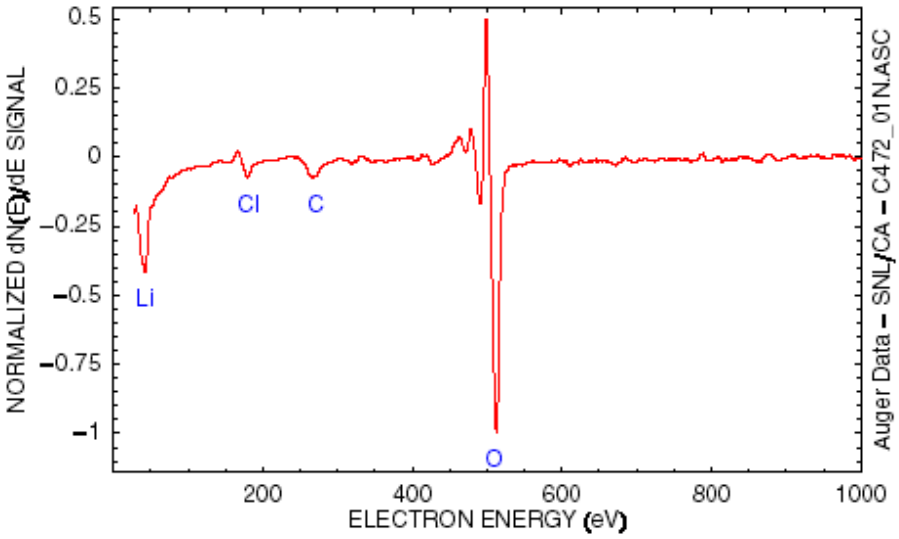

Figure 3.5. Area 1 surface analysis. Auger electron energy spectrum of area 1 on the Sn-Li sample as it was received.

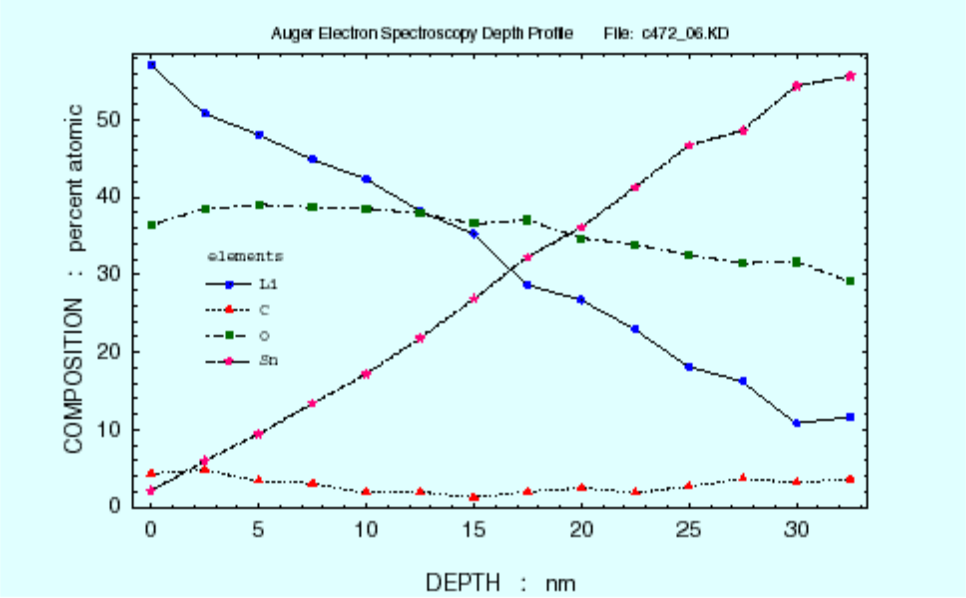

Figure 3.6. A depth profile of the sample at area 2 was obtained by sputter/Auger spectroscopy. A Li-rich surface layer was observed. Below this layer a composition

more like the bulk Sn-L alloy was seen. Li decreases and Sn increases with depth. The sample appeared to have been substantially oxidized.

Figures 5.7 show two scanning electron images of the materials ejected from the melting of SnLi in the stainless steel crucible. The figure on the left shows the inhomogenous and bubbly material that was ejected. The figure on the right is a ball of ejected alloy.

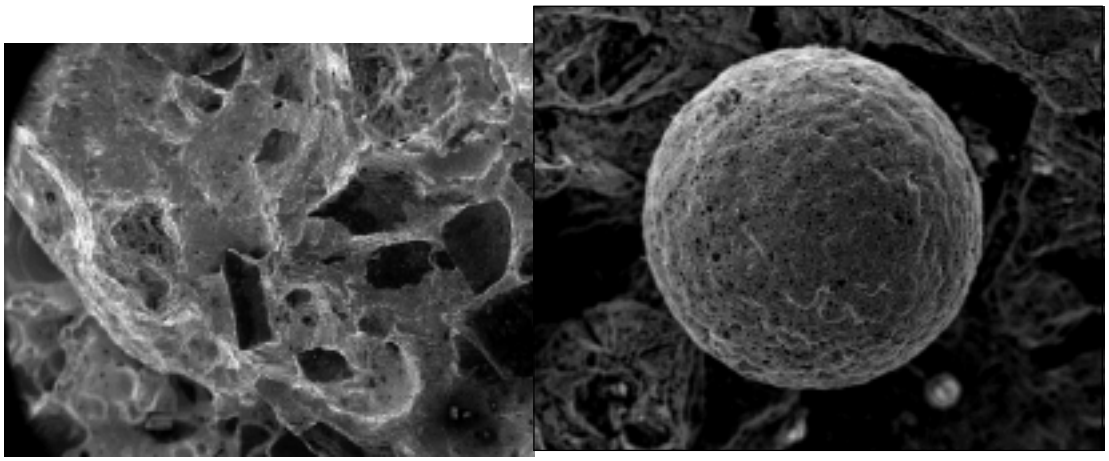

Figure 3.7. SEM images of ejected material. The light sections are mostly Sn—electrons scatter more from Sn than Li or O, thus the lighter color. The ball is approximately 200μm across.

X-ray analyses of the ejected materials showed areas rich in Sn and other areas rich in oxygen. We cannot see Li with the SEM X-ray detector (theLi-K line is too low in energy) but we assume that the oxygen-rich Sn-poor areas are Li rich. Figure 3.8 below shows some X-ray maps of ejected material and the separate Sn rich and O-rich areas.

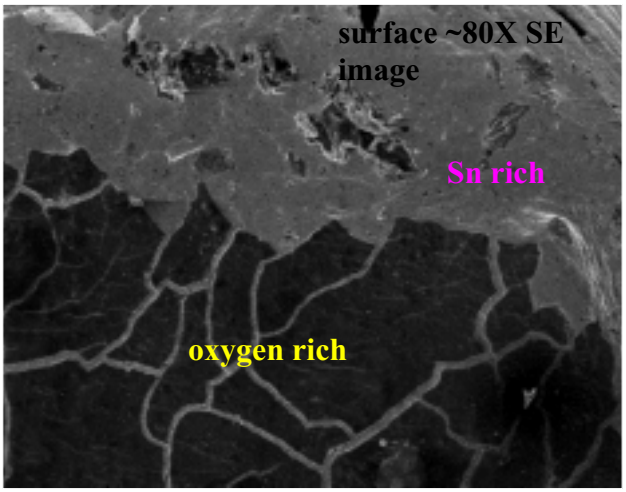

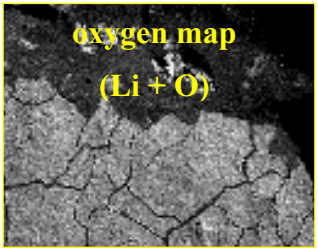

Figure 3.8 (right). SEM image of material ejected from SnLi melted in SS crucible on top, with x-ray maps of the same region underneath

3.3 Melting SnLi in BN-lined crucible

Another sample of SnLi was obtained from Ken Natesan to melt in a BN-lined crucible. The lining provided additional thermal insulation between the crucible and the alloy, and the alloy melted more slowly. Also less power was applied to the heater to slow down the reaction and prevent bubbling and loss of material. A residual gas analyzer was added to the vacuum chamber to measure the gases that were released when the alloy was first melted. This melt proceeded much more calmly, but the surface of the alloy was not very clean and areas with solid compounds on the surface were observed. The pictures of the molten alloy are shown in Figure 3.9. When the SnLi alloy was melted a significant amount of hydrogen was released, as shown in Figure 3.10.

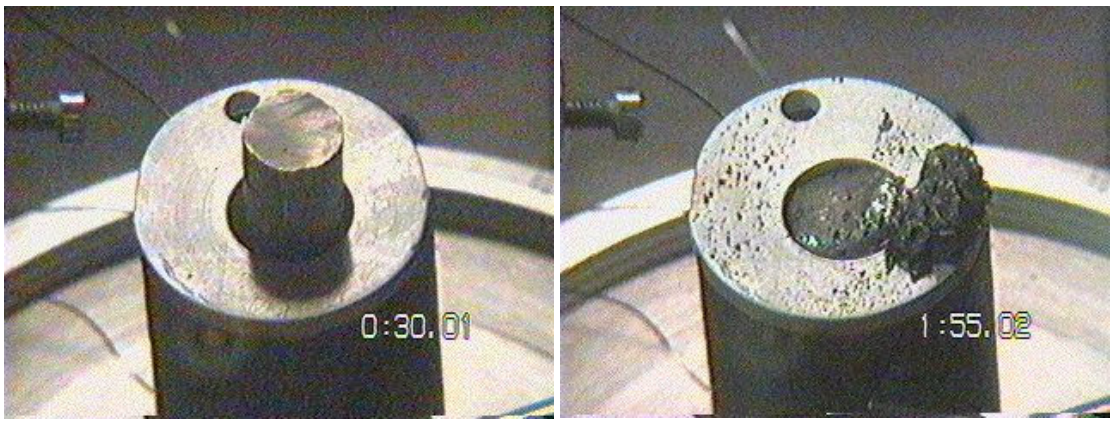

Figure 3.9 . SnLi alloy melted in BN-lined crucible.

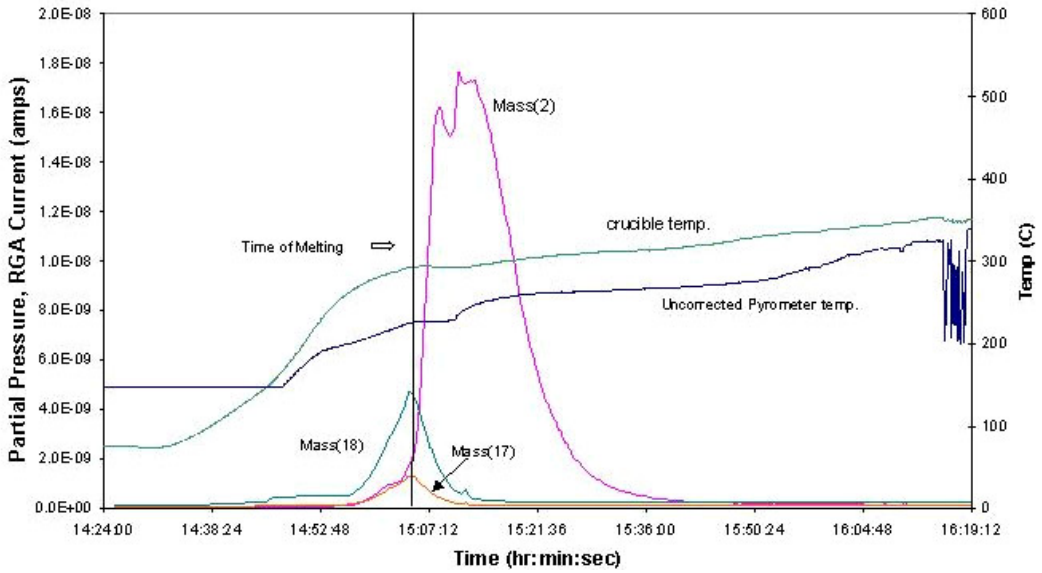

Figure 3.10. RGA output compared to temperature of alloy. Hydrogen was the highest signal measured.

A stainless steel rod was dipped into the molten SnLi and a solid compound quickly formed on the rod. The compound that formed on the rod was low in iron, chromium or nickel, materials in stainless steel, therefore, we do not believe that the SnLi reacted with the stainless steel chemically, but may have caused the compound to condense because of temperature differences.

3.4 Conclusions on SnLi

The APEX Team study of SnLi as a possible first wall and breeding material prompted our consideration of possible use of SnLi in the Sandia liquid metal loop (LIMITS) and we have gained some limited experience in handling this material. Our application in LIMITS would involve melting and resolidifying the SnLi and experiments in which an open surface of SnLi would be heated. Since we observe that SnLi does not appear to remain as a single well-mixed solution and it is known that SnLi is likely to form solid

compounds[3], we conclude that SnLi would not remain a uniform liquid in our liquid metal loop. Due to these considerations, we are not planning to use SnLi in our flow loop. This consideration may also be important for a reactor application and should be reviewed by the ALPS and APEX Team

In our melt experiment the SnLi released significant H_2 upon melting and the melt continued to bubble under vacuum conditions. Also, we observed some coating of the diagnostic windows of our chamber when the SnLi melt was heated above 400 °C.

3.5 References

1. K. Natesan and W. E. Ruther, "Fabrication and properties of a tin-lithium alloy," Fusion Materials Semiannual Progress Report, DOE/ER-0313/27, Dec. 1999

2. S. Sharafat and N. Ghoniem, "Summary of thermo-physical properties of Sn, and compounds of Sn-H, Sn-O, Sn-C, Sn-Li, and Sn-Si and Comparison of Properties of Sn, Sn-Li, Li, and Pb-Li" Apex Study E-meeting, UCLA-UCMEP-00-31 Report, August 2000

3. Cees van der Marel, Jean Hennephof, Gerrit J. B. Vinke, Ben P. Alblas and Willem van der Lugt, "Physical Measurements on Liquid Lithium Alloys: Material behavior and physical chemistry in liquid metal systems", Plenum, New York, NY (1982) p401-410

4. Li Loop Development

Jimmie McDonald, Tina Tanaka, Ken Troncosa, Richard Nygren and Dennis Youchison, Sandia National Laboratories

Assessing the maximum possible heat removal of a particular LS concept is a very basic objective in the development of liquid surface PFCs, and high heat flux testing is a logical approach. However, in some ways it is easier to design large (costly) HHF experiments (for example use of the ALEX loop at ANL with a neutral beam heat source) than to design small tests. The engineering of useful small experiments that combine high heat flux with a magnetic field is by no means straightforward since an impinging heat source must be used with a free surface. One critical issue is measuring temperature distributions so that the MHD effects on heat transfer can be deduced.

4.1 Loop Design

Sandia has designed and will be receiving a new Li loop that will be coupled with the existing vacuum chamber now being used for our liquid metal heating tests.

Basically the unit consists of a heated vessel, rotary pump, dump tank and associated piping and our test chamber. The heated vessel or furnace has a specified capacity of 66 liters and

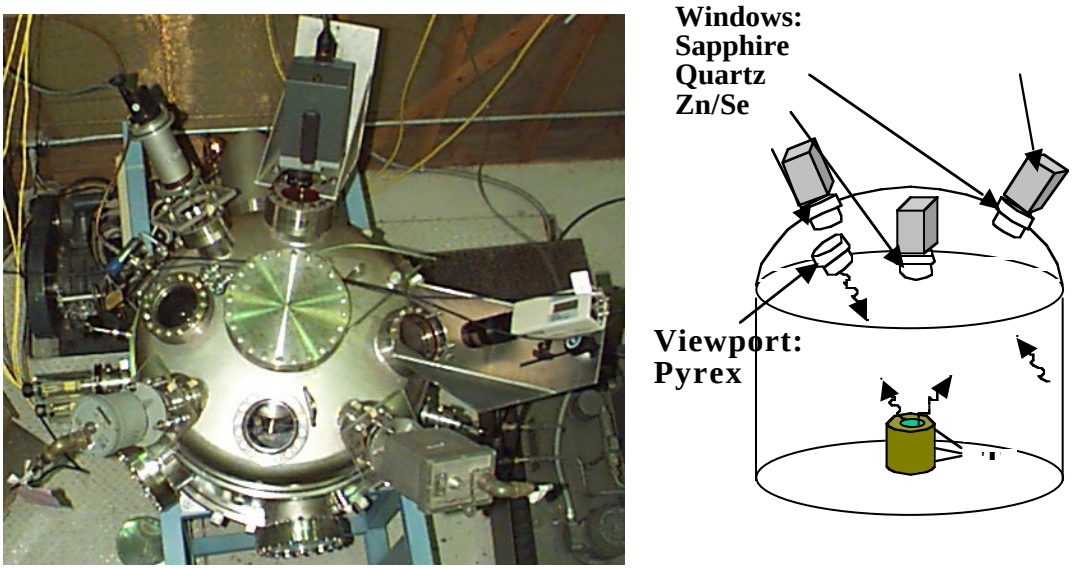

Fig. 4.1. Liquid metal test chamber

maximum temperature of 450°C. The specifications for the dump tank are a capacity of 82 liters and maximum temperature of 500°C. Both are made of 316L stainless steel. Figure

4.1 shows the test chamber; it is not yet installed into the EBTS facility and has been in use for heating tests on various liquid metals.

Figure 4.2 is a sketch of the Li loop components. We expect to receive in August 2001 and perform initial acceptance tests. We expect the first operational test to be done with a closed pipe prior to subsequent tests with free flowing Li.

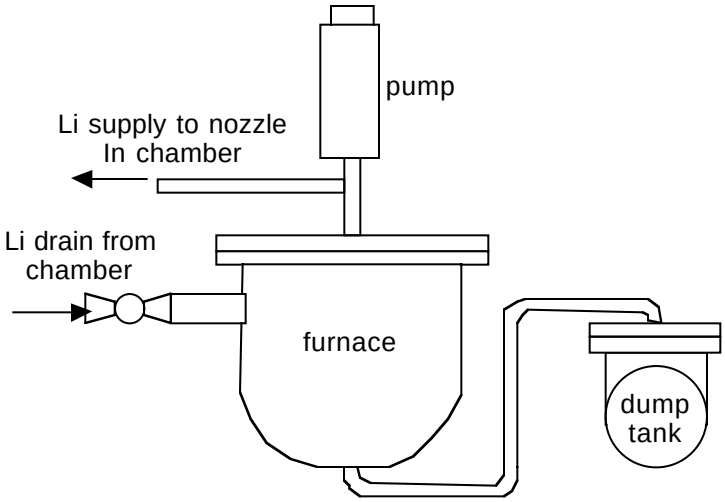

Fig. 4.2. Sketch of Li loop

4.2 Nozzle Design and Modeling for the Li Loop

In the Li loop being prepared at Sandia National Laboratories, a nozzle will inject a lithium steam into the vacuum chamber of our small electron beam facility (EBTS). The first test will be on a closed system. The initial test on a open system will be with a free flat stream. Other configurations, e.g., droplets and other streams are also being considered. In the preliminary studies to develop a nozzle for a flat stream (reported here), we adapted the Japanese design for the nozzle for the International Fusion Materials Irradiation Facility (IFMIF) and the nozzle size was scaled to fit the Sandia LiMITS (Liquid Metal Interaction Test System). We evaluated this with a finite volume method computational fluid dynamics code (CFD2000) and with water tests through a simple plastic model. We also examined results provided by UCLA on nozzles with rather low compression ratios used in their studies.

While a high compression nozzle, such as the one designed for IFMIF, may be more to reduce turbulence, effective, we have concluded that a smaller single compression nozzle will better meet the requirements for flow geometry, easy drainage, etc. for the LiMITS facility. The design of a nozzle with an intermediate compression ratio of about 3:1 is now being studied.

Fig. 4.3 shows a sample result from the CFD2000 model. We found that quiescent, nearly uniform cross section, free flows of Li would propagate as much as 34 cm in near vacuum under the influence of gravity. Such flows could be used for subsequent heat transfer experiments in LiMITS. In the model a second fluid (rather than vacuum) is required.

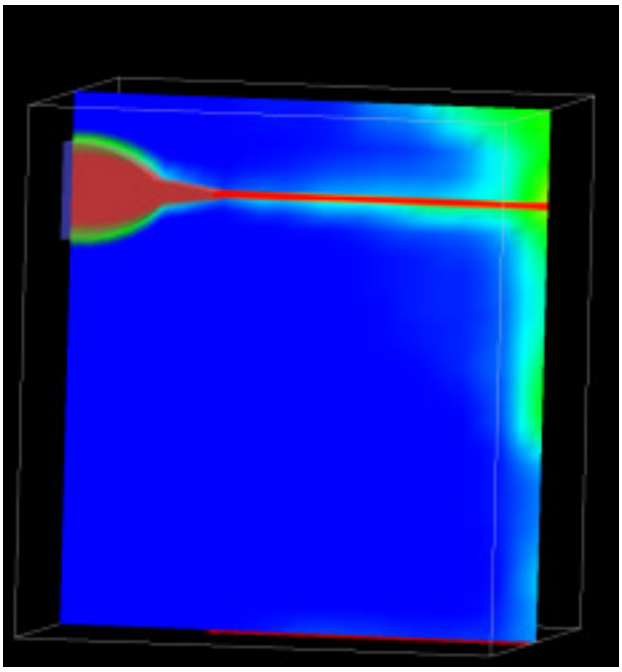

Fig. 4.3 Li at 10 m/s flowing through air (.75 Torr) under influence of gravity. Red = 100% Li and blue = 100% air in volume of fluid representation.

In our preliminary water flow tests on a plastic nozzle (Fig. 4.4), we monitored the pressure and flow rate and took photos of the stream. For an exit velocity of 10m/s, the volumetric flow rate from this nozzle (25.4x4mm) is ~16.1gpm. At flow rates up to about 8gpm, the stream seemed fairly well behaved. At higher flow rates, there was more tendency for small side streams and apparent instability of the surface. However, the plastic at the nozzle exit had some surface flaws that may have contributed to the development of side streams.

To maintain a flat area for heat transfer studies, the practical limits (in the absence of a magnetic field) appear to be the encroachment from the sides of the stream of (a) waves that propagate from the edge of the nozzle, and (b) the rounding and thickening of the stream at the edge due to surface tension. The half period distance for inversion of the stream from horizontal to vertical was also estimated. The distance to the end of the "V" tongue was measured in the photos and is listed in the table. A rough extrapolation indicates the distance halfway to the "V" would be about 60mm at 10m/s.

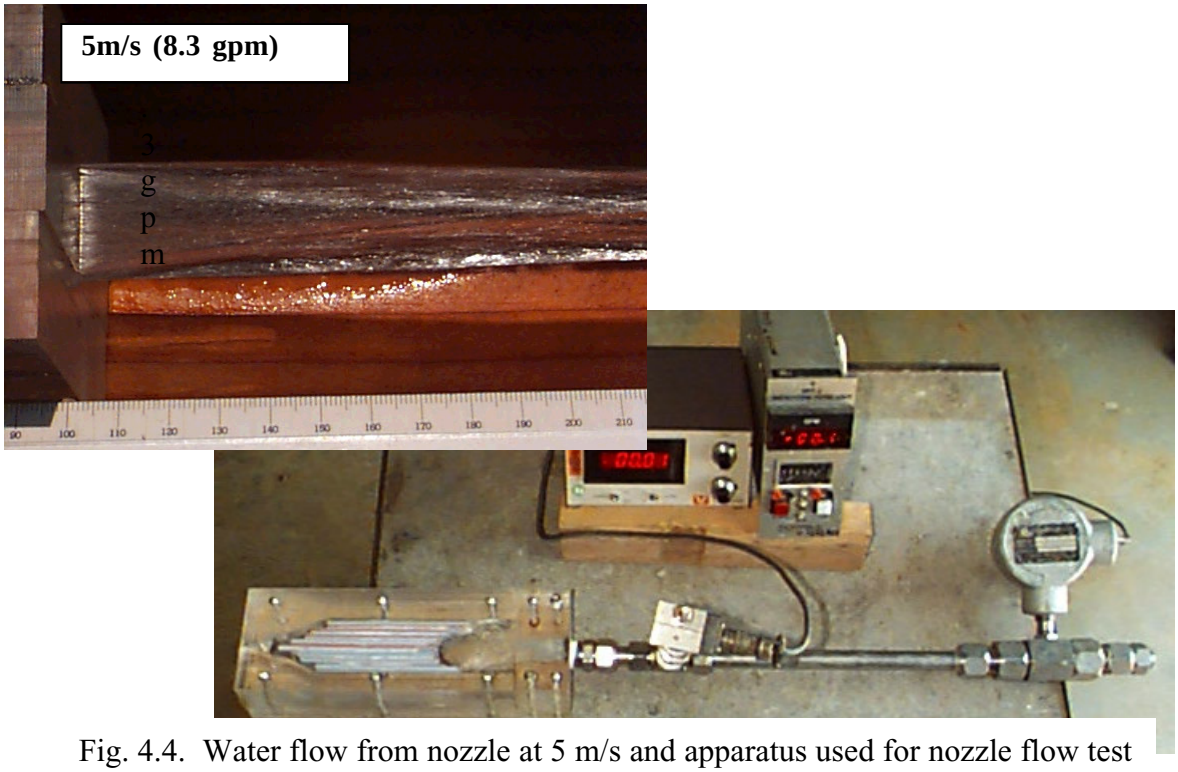

Fig. 4.4. Water flow from nozzle at 5 m/s and apparatus used for nozzle flow test

nozzle test 1aug00 4 = nozzle height (mm)

	comments	*P (psi)*	*flow (gpm)*	*Velocity (m/s)*	*V-length (mm)*	*1/2 period (mm)*
1		0.12	2.8	1.74	17	
2		?	3.8	2.36	20	
3	dumbell distortion in X-section increases	0.63	5.7	3.54	25.5	~350
4		0.9	6.4	3.97	26.5	
5		1.85-1.9	8.3	5.15	36.75	
6		5.1	13	8.07		~600
7		14.4	21.4	13.29		
8		7.7-7.8	15.7	9.75		

See separate attachment

5. Li Handling Experience

Jimmie McDonald, Tina Tanaka and Ken Troncosa, Sandia National Laboratories

Basically Li is chemically very active and will combine easily with hydrogen, nitrogen and water in the air. Preserving the purity of Li and Li surfaces and protecting against the hazard of a Li fire are both important aspects with regard to handling of Li. Sandia has investigated handling of this material in preparation for experiments on melting of Li and heating of liquid Li. Outside the fusion program, Sandia has experience in handling of Li in its research on batteries.

Li is typically shipped from a supplier in a sealed container. Foils are typically in a bag under argon atmosphere. Ingots are typically shipped under argon or in a bath of mineral oil. To minimize the contamination without going to heroic measures for the small quantities of Li we have dealt used to date, we have opened the Li containers in a vessel back-filled with argon. For example, when we needed to cut Li from a roll of foil, we did this in a rough vacuum chamber with a large lid on top that had been back-filled with argon. In another case we transferred the Li in a bag filled with argon. We then transferred the desired quantity of Li into a mason jar, also filled with argon, and carried the jar to our test chamber. There we placed the jar in the test chamber that had also been previously evacuated and back-filled with an argon cover gas. During the operation lab personnel wear protecting glasses and clothing as shown in Figure 5.1.

Fig. 5.1. Equipment for Li handling

Sandia has drafted a brief procedure, given below, for Li handling in the lab and we have used this procedure in transferring small quantities. We are in the process of developing handling procedures for our specific applications in the Fusion Technology Department. These include the transfer of a larger quantity of Li with which we will charge our Li loop. For this operation we are outfitting a glove box that will hold the Li tank for the loop. Issues related to future Li handling are being investigated as part of the process of developing a readiness evaluation for the Li loop.

July 31, 2000

Initial Working Draft of LITHIUM HANDLING PROCEDURE

Caution Do not handle lithium (Li) alone. A minimum of two people are required to be in the lab during these procedures and within normal voice range of each other.

Required safety equipment
1. Tweezers
2. Pliers or Tongs
3. Scoop
4. Goggles
5. Gloves, butyl or Silver Shield
6. Face shield for some operations, see below
7. Arm covers or coveralls

For operations in a glove bag
1. Goggles only

For operations in the Liquid Metal Experiment (LME)
1. Face shield
2. Goggles
3. Gloves
4. Coveralls or arm covers

In the case Li pieces are spilled, the cleanup process is
1. Pick up pieces using tongs, pliers, tweezers or a scoop and return to container
2. Wipe area with Butanol
3. Wipe up excess Butanol

In case of a Li fire
1. Use Lith-X to extinguish, or
2. Pump LME chamber

6. Heat Flux Limits For Flowing Liquids

M. Ulrickson, Sandia National Laboratories

Heat flux limits for flowing liquid surfaces composed of either Li or Sn75Li25 were estimated for the first wall and calculations for surfaces of pure Sn, In and Ga were included for divertor surface applications. The models use laminar flow and the best estimates of the surface temperature limits from plasma modeling. Any turbulence would tend to reduce the surface temperatures. However, the experimental evidence from the Russian tokamaks supports laminar flow. There are no experiments on using induced currents to mix the flow. Where the thermal properties are not known, e.g., Sn-Li, we have tried to use conservative values in the estimated properties.

6.1 Thermal Properties

Lithium The thermal properties of Li are from the APEX Interim Report.

Tin-Lithium The thermal properties of Sn-Li alloys are not known but estimates were derived. (There is also a separate progress report on this area.)

Tin Equations are given for k, C_p, and ρ.

Indium Equations are given for k, C_p, and ρ.

Gallium Equations are given for k, C_p, and ρ.

6.2 Heat Load Limits

Heat load limits were developed based upon surface temperature limits associated with the acceptable level of plasma impurity. For Li and SnLi, Tom Rognlien provided the surface temperature limits. For Sn, In and Ga, allowed concentrations and associated surface temperatures were based on an allowable limit scaling with Z^3 or a possible limiting value from the collapse of the sheath due to ionization of the evaporated material. The limiting values for Z^3 scaling were 600°C for Sn and Ga and 500°C for In. And Jeff Brooks has estimated the limit for Sn for sheath collapse to be about 1000°C. The equivalent evaporation rates for In and Ga occur at 800°C and 850°C respectively. The first estimate is likely to be the lower bound. The second estimate is likely to be the upper bound.

To assess the allowable heat flux, a constant heat flux was applied to each material and the time required to reach the temperature limit was determined. In all cases the starting temperature was 40°C above the melting point. The results are shown in Figure 6.1, 6.2 and 6.3. It can be seen that both Li and SnLi have similar behavior. The lower end of the estimated values for SnLi are about a factor of two below the higher values. Even though SnLi has a wider temperature window, the thermal properties are poorer resulting in nearly identical performance limits. The allowed duration is inversely proportional to the square of the heat flux. For the lower bound temperature limit both pure Sn and pure In are very similar to Li. Gallium shows a substantial advantage over the other materials. For the upper bound Sn and In have an advantage over Li, but Ga is clearly superior again.

Analyses of the effect of the divertor angle and flow velocity were also included in the report and cases with the peaked heat flux profile for ITER were analyzed. The conclusions areas follows. The thermal properties of molten SnLi alloys need to be measured to reduce the uncertainty of these calculations. Li and SnLi appear from these estimates to have very similar heat flux windows of operation, but SnLi could have poorer performance if the thermal properties are at the lower limits estimated.

Gallium appears to have a considerable advantage over all the other materials from a thermal performance standpoint. Other factors such as cost, activation and corrosion will need to be considered. The peak surface temperature is only a weak function of the flow velocity (increasing velocity does not increase the heat flux limit very much). For turbulence to significantly increase the heat flux limits, the turbulence would have to mix the top 1-2 mm of the fluid in millisecond time-scales. Experiments are clearly needed to confirm these estimates.

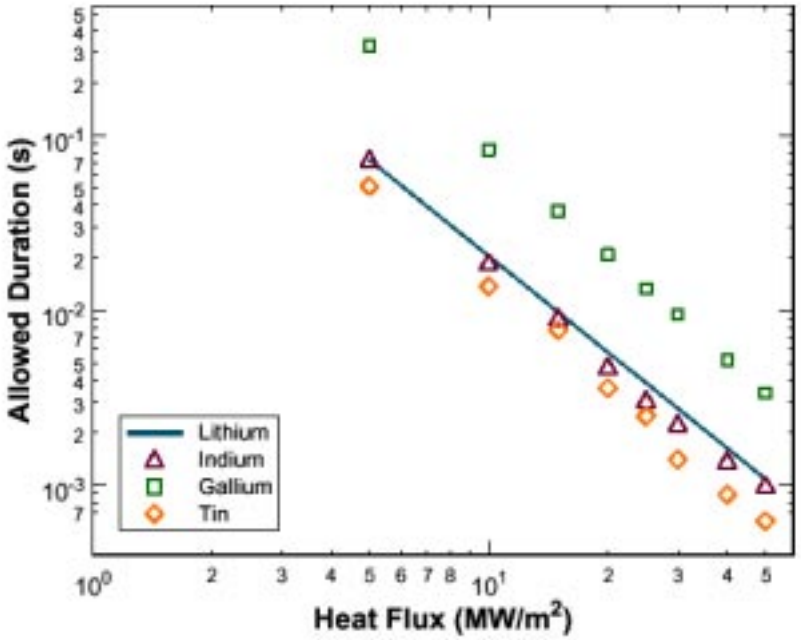

Figure 6.1. The allowed duration of heat flux on a flowing liquid surface is shown as a function of the heat flux. The high and low estimates for SnLi are shown (see text). The slop of the curve is –2.

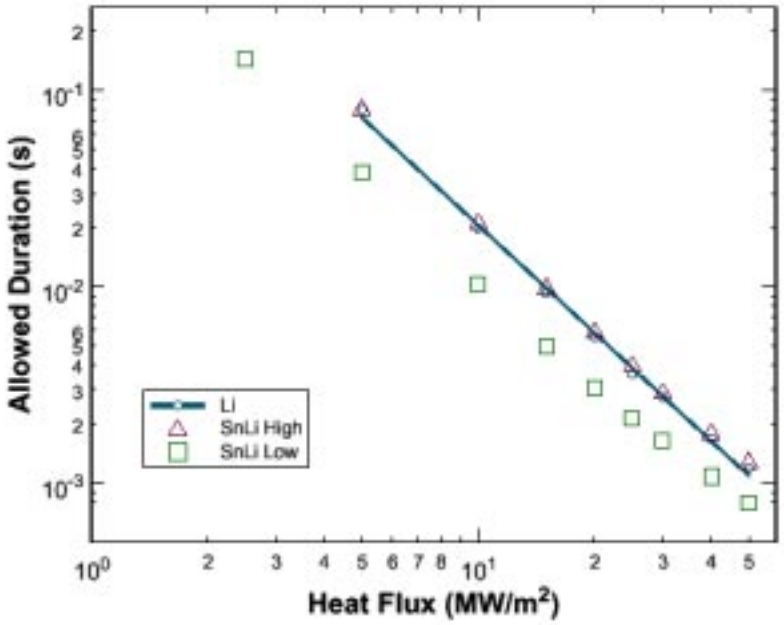

Figure 6.2. Calculated allowed duration of heat flux for the case of the lower bound temperature limits (see text) for Ga, In and Sn compared to the values for Li.

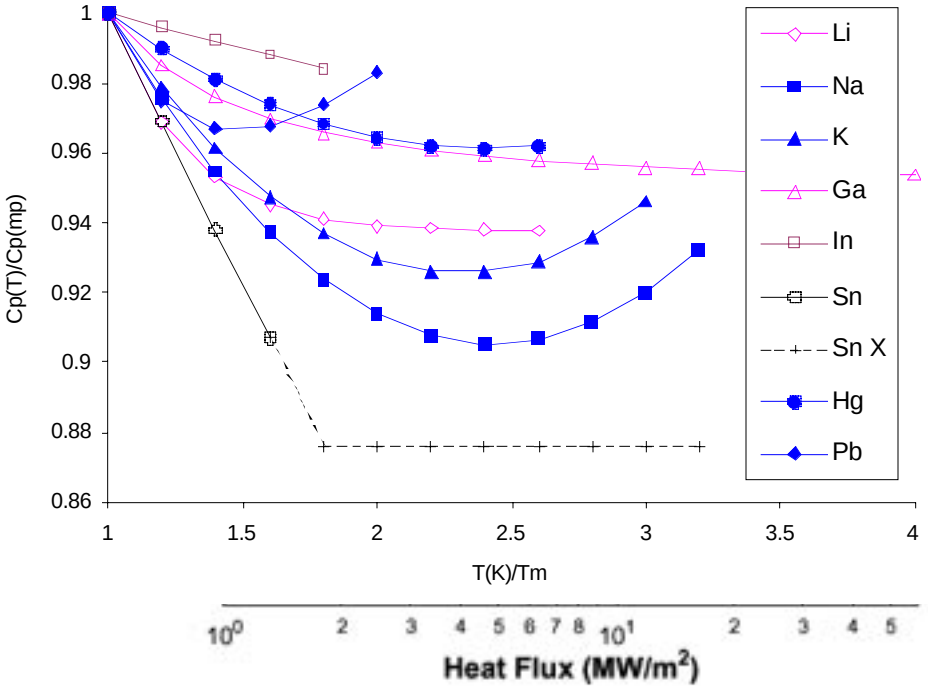

Figure 6.3. Calculated allowed heat flux duration for the upper bound temperature limits (see text) for Ga, In and Sn compared to the value for Li.

7. Notes on the thermal Properties of Sn

Richard Nygren, Sandia National Laboratories

Experimental data on the thermophysical properties of liquid Sn are available over only a limited range. For example, for the Cp of liquid tin, Mike Ulrickson and I have found data over only a limited range of temperature, e.g. compilations in Refs. 1-3 (Let me add that I do consult the Sharafat/Ghoniem compilation on the APEX website.) We all know that in making calculations that require data on Sn (and perhaps other metals) at high temperatures (T>1000K) we should be careful about extrapolating data. This note documents how I am estimating the heat capacity and thermal conductivity of liquid tin.

7.1 Heat Capacity, Cp

I have recently been examining a parameter fit by Kubaschewski and Alcock.[4] I set values for the Cp of tin as indicated below. In Fig. 7.1, I plotted Cp(T)/Cp($T_{m.p.}$) versus homologous temperature (T/Tm) for various liquid metals. For Sn, I cut off the extrapolation somewhat arbitrarily at T/Tm of 1.8 and, in the absence of data, am using a flat extrapolation beyond this point. The actual trend may be to rise again as is suggested by curves for Na, K and Pb or, like the curves for Li and Ga, stay rather flat. The main point is that a continued extrapolation of the initial rapid decline seems inappropriate. Note -- Units for the Fig. 7.1 are J/g-K, however the table of coefficients (Table 7.1) is taken directly from Ref. 3 with units of J/mole-K.

Fig. 7.1 Trend curves showing the value of C_p at the temperature indicated divided by C_p at the melting temperature versus temperature.

In these data Cp drops quickly with temperature above the melting temperature over the short range of the data. *While theory in solid state physics may help in estimating the*

dependence of thermal conductivity on temperature there is less hope for such guidance for the heat capacity (paraphrase from [3]).

Table 7.1 Coefficients for Heat Capacity [4]
$Cp = C1 + C2*T + C5/T^2 + C3*T^2$
Units are (J/mole-K). Range is indicated.

	C1	C2 (10^{-3})	C5(10^5)	C3(10^{-6})	mp	low	hi	hi/Tm
Li	24.48	5.48	8.66	-1.954	454	mp	1200	2.6
Na	37.51	-19.221		10.636	371	mp	1200	3.2
K	37.18	-19.12		12.3	336	mp	1037	3.1
Ga	26.36		1.26		303	mp	1200	4.0
In	30.29	-1.38			430	mp	800	1.9
Sn	34.69	-9.2			505.3	510	810	1.6
Hg	30.38	-11.46		10.155	234.4	298	630	2.7
Pb	32.43	6.15	21.13		600	mp	1200	2.0

7.2 Thermal conductivity, k

The k of liquid tin rises over the limited temperature range of available data. Based on arguments about what should happen near the critical temperature (~8000K) per Ho, Powell and Liley[5], **k** will "round over" and decline at very high temperatures. (They show this "rollover" point for Li with the maximum (null derivative) near the boiling point of Li.)

The Weidmann-Franz-Lorenz law, given below, relates thermal conductivity to electrical conductivity (for metals). The Lorenz number (0.0245) is a theoretically derived constant but experimental values are found to deviate somewhat.

$$\frac{k}{\sigma_e T} = 0.0245 \qquad (W\mu\Omega/K^2)$$

Ho, Powell and Liley[5] use a straight line extrapolation for their recommended curve of **k** for liquid tin from the melting point to 973K using a Lorentz number of 0.02443 and values of the electrical resistivity at the end points of this range.

I have used their formulation but substituted values for electrical resistivity from Cusack and Enderby[6] for a range up to 1473K and then further extrapolated these data to obtain the curve **k**-REN shown on the next page. The portion of the curve at higher temperatures, where there is a significant deviation from the linear extrapolation, is based on extrapolation of the resistivity data past the range quoted by Cusack and Enderby.

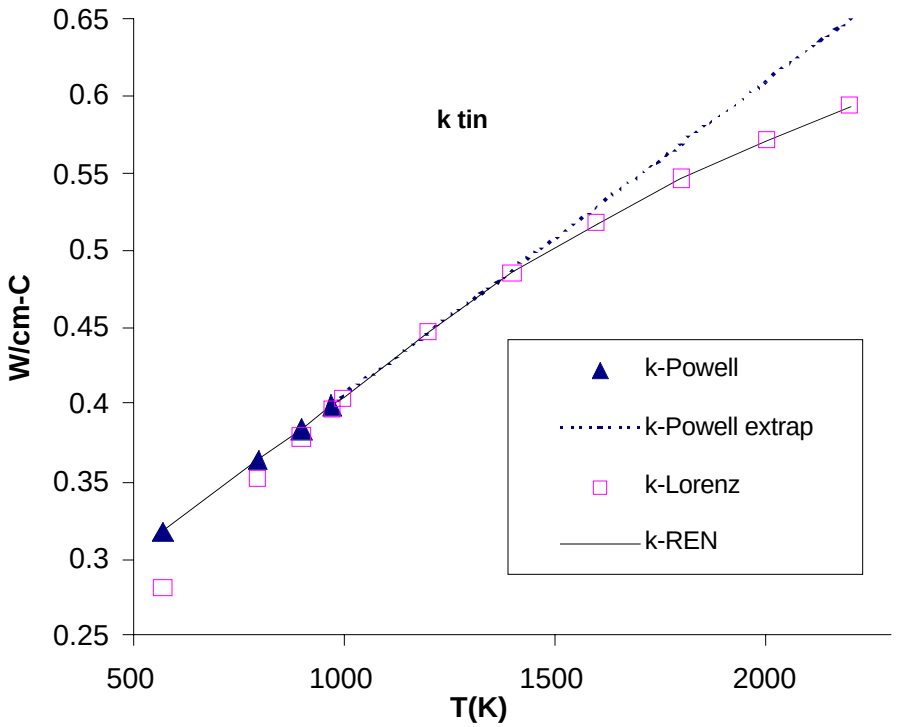

Figure 7.2. Values of thermal conductivity of liquid Sn versus temperature. The solid line indicates the expression preferred by Nygren.

Table 7.2 Values for k for liquid tin
(extrapolated values are in italics)

T(C)	k-Powell	k-Powell extrap	k-Lorenz	resist	k-REN
573.2	0.317		0.281	49.67	0.317
800	0.363		0.352	55.32	0.363
900	0.384		0.379	57.81	0.384
973.2	0.399	0.399	0.397	59.63	0.399
1000		*0.404*	0.403	60.30	0.404
1200		*0.445*	0.447	65.28	0.445
1400		*0.486*	0.485	70.26	0.485
1600		*0.527*	0.517	*75.24*	*0.517*
1800		*0.568*	0.546	*80.22*	*0.546*
2000		*0.609*	0.571	*85.20*	*0.571*
2200		*0.650*	0.594	*90.18*	*0.594*

If anyone has other information or suggestions for how to handle the thermophysical property data on Sn, I would appreciate suggestions.

7.3 References

[1] R. Hultgren, R.L. Orr, P.D. Anderson and K.K. Kelly, Selected Values of Thermodynamic Properties of Metals and Alloys, John Wiley & Sons (1963)

[2] Y.S. Touloukian, Thermophysical Properties of Matter, Vol. 4, Specific Heat of Metallic Elements and Alloys, IFI-Plenum (1970)

[3] T. Iida and R.I.E. Guthrie, The Physical Properties Liquid of Metals, Clarendon, Oxford, 1988.

[4] O. Kubaschewski and C.B. Alcock, "Metallurgical Thermochemistry," Permagon, Oxford, Table C1, p336, cited [3]

[5] C.Y. Ho, R.W. Powell, P.E. Liley, J. Physical and Chemical Reference Data, **3** (1974)

[6] Cusack and Enderby, Proc. Phys. Soc., 75 p395, cited in Iida[3], Table 8.1 p232

8. IR Camera at UCLA and CDXU

Jimmie McDonald, Dennis Youchison, Tina Tanaka, Richard Nygren and Mike Ulrickson, Sandia National Laboratories

In our work in the Fusion Technology Department at Sandia, we utilize various pyrometers and several IR cameras to measure temperature optically on the surface of samples that we test in our electron beam heating facilities. We have also used the IR cameras for thermography outside the e-beams, for example, to evaluate braze flaws in armored tubes for Tore Supra in rapid thermal pulses with hot water. We also have programs in which we place IR cameras on site at collaborating institutions. Recent examples include IR measurements on CDXU at PPPL and at ULCA.

In the application at CDXU, the low magnetic field outside the coils was still sufficient to affect the motor drive for the mirror. Sandia has designed a magnetic shield for the camera for future use in magnetic environments. The camera has also been lent to UCLA and was used at Sandia in collaboration with UCLA researcher Brent Freeze for exploratory tests in which a drop of hot water penetrated into a jet of cold water from a nozzle.